SCUOLA DI DOTTORATO

UNIVERSITÀ DEGLI STUDI DI MILANO-BICOCCA

Dipartimento di / Department of
Fisica "Giuseppe Occhialini"

Dottorato di Ricerca in / PhD program: Fisica e Astronomia Ciclo / Cycle: XXXIII

ELECTROMAGNETIC COUNTERPARTS OF DOUBLE NEUTRON STAR AND BLACK HOLE-NEUTRON STAR BINARY MERGERS

Cognome / Surname: Barbieri Nome / Name: Claudio

Matricola / Registration number: 805888

Tutore / Tutor: Prof. Monica Colpi

Cotutore / Co-tutor: Dr. Om Sharan Salafia

Coordinatore / Coordinator: Prof. Marta Calvi

ANNO ACCADEMICO / ACADEMIC YEAR 2020/2021

DECLARATION

I hereby declare that the thesis entitled "Electromagnetic counterparts of double neutron star and black hole - neutron star binary mergers" submitted by me, for the award of the degree of *Doctor of Philosophy* to Milano-Bicocca University is a record of bonafide work carried out by me under the supervision of Prof. Monica Colpi and Dr. Om Sharan Salafia.

I further declare that the work reported in this thesis has not been submitted and will not be submitted, either in part or in full, for the award of any other degree or diploma in this institute or any other institute or university.

Finally I declare that part of this work has been published in Barbieri et al. (2019a,b, 2020a,b).

Place: Milan

Date: 23/10/2020

Signature of the Candidate

Claudio Barbieri

CERTIFICATE

This is to certify that the thesis entitled “Electromagnetic counterparts of double neutron star and black hole - neutron star binary mergers” submitted by Mr. Claudio Barbieri to Milano-Bicocca University for the award of the degree of *Doctor of Philosophy*, is a record of bonafide work carried out by him under our supervision, as per the Milano-Bicocca University code of academic and research ethics.

The contents of this report have not been submitted and will not be submitted either in part or in full, for the award of any other degree or diploma in this institute or any other institute or university. The thesis fulfills the requirements and regulations of the University and in our opinion meets the necessary standards for submission.

Place: Milan

Date: 23/10/2020

Signature of the Supervisor

Signature of the Co-supervisor

TABLE OF CONTENTS

ACKNOWLEDGEMENT i

ABSTRACT ii

LIST OF FIGURES iv

LIST OF TABLES vii

LIST OF TERMS AND ABBREVIATIONS viii

1 Introduction 1

1.1 Context 1

1.2 My contribution 3

2 Gravitational Waves 6

2.1 Basic physics of GWs 6

2.2 Coalescence of compact binaries 10

2.2.1 Energy loss and GW signal frequency evolution 11

2.3 GW signal analysis 12

2.3.1 Waveform and detection 12

2.3.2 Parameter estimation 14

3 Ejecta from NSNS/BHNS mergers 17

3.1 Merger remnant and ejecta production 17

3.2 Dynamical ejecta 19

3.3 Disk ejecta 20

3.3.1 Wind ejecta 21

3.3.2 Secular ejecta 21

3.4 Adopted fitting formulae for ejecta properties 24

4 Kilonovae 27

4.1 History of kilonovae 27

4.1.1 The r-process in the Universe 27
4.1.2 The “birth” of kilonovae 28
4.2 Kilonova model 30
4.2.1 NSNS 30
4.2.2 BHNS 33
4.3 Kilonova example light curves 36

5 Gamma-Ray Bursts 38
5.1 A brief history 38
5.2 Basis of GRBs 39
5.3 Relativistic jet 40
5.3.1 Jet launch and breakout condition 40
5.3.2 Jet launch 41
5.3.3 Jet structure 43
5.4 GRB prompt emission 44
5.5 GRB afterglow emission 45
5.5.1 Dynamics 47
5.5.2 Equal-arrival time surfaces 48
5.5.3 Radiation 49
5.5.4 GRB afterglow example light curves 50
5.6 Kilonova radio remnant 51

6 Analysis 54
6.1 EM counterparts dependence on BH and NS properties 54
6.1.1 NSNS 54
6.1.2 BHNS 56
6.2 GW+EM multi-messenger astronomy 57
6.2.1 Binary parameter estimation improvement 61
6.2.2 Distinguishing the nature of “ambiguous” systems 63
6.2.3 Organisation of the EM follow-up campaign 71
6.3 NSNS/BHNS horizons and EM counterpart peak properties distribution . 74
6.3.1 BHNS/NSNS populations and binary parameters distribution . . . 75
6.3.2 GW and EM signals 76

6.3.3 BHNS/NSNS mergers detection rates and horizons 78
6.3.4 EM counterparts peak properties distribution of GW-detectable BHNS/NSNS mergers 82

Conclusions **87**
REFERENCES 89
LIST OF PUBLICATIONS 103

ACKNOWLEDGEMENT

With immense pleasure and deep sense of gratitude, I wish to express my sincere thanks to my supervisor Prof. Monica Colpi. Her trust in me was fundamental for my personal growth in these years.

I further thank Dr. Albino Perego and Prof. Giancarlo Ghirlanda for their personal support, their help in the development of our models and their collaboration in our publications.

I express my sincere thanks to Dr. Om Sharan Salafia for his fundamental help in my research activity, his kind words of support and encouragement and his precious scientific and non-scientific advices.

I would like to acknowledge the support rendered by my colleagues Mr. Alberto Mangiagli and Dr. Federico Abbate in several ways throughout these three years.

I wish to extend my profound sense of gratitude to my parents, Mauro and Flavia, for all the sacrifices they made to support me during my studies.

I thank my sister Chiara for providing me encouragement whenever required.

I wish to remember my grandfather Enrico, who left us to join his wife Marisa beyond the stars.

Last but not the least, I would like to thank my wife Rossella. Despite all the binary mergers detected in this exciting new gravitational waves astronomy era, the most important merger happened on 19th July 2019 when, after almost 8 years (2804 days to be precise) our hearts merged together in the sacred bond of marriage. Thank you Rossella for your constant encouragement and moral support along with patience and understanding. Thank you for everything, my love.

ABSTRACT

This PhD dissertation is focused on the electromagnetic (EM) counterparts of gravitational waves (GW) signals from double neutron star (NSNS) and black hole-neutron star (BHNS) mergers.

I developed semi-analytical models to predict the multi-wavelength emission from BHNS mergers, including the kilonova, its radio remnant, the prompt emission from the relativistic jet and the related gamma-ray burst (GRB) afterglow. Adopting fitting formulae in the literature, I established a link between the binary parameters and the EM counterparts properties.

I anticipated the variety and the high degree of degeneracy of EM counterparts from BHNS mergers. I showed how joint GW+EM analysis can reduce this degeneracy, performing a proof-of-concept multi-messenger parameter estimation, considering a BHNS merger with an associated kilonova. My results indicate that joint analysis can produce better constraints on the binary parameters. This would lead to a deeper understanding of the NS and BH fundamental physics (e.g. the NS equation of state and maximum mass, the BH spin distribution) and would give information on the formation and evolution of compact object binaries.

I analyzed "ambiguous" coalescing binaries (consistent with both NSNS and BHNS), whose nature may not be identified through the GW signal alone. In the BHNS case, the binary would host a "light" stellar BH, with the mass falling in the theoretically expected and to date observationally confirmed discontinuity between NS and BH mass distributions (mass-gap). I found that the observation of the associated kilonova could unveil the system's nature, as in the BHNS case it can be far more luminous with respect to the NSNS case. Applying this analysis to the GW190425 event, I found that the kilonova would have been detectable if the binary had hosted a BH (if the source had been precisely localized), potentially disentangling the nature of the merging system. The observation of a kilonova from an "ambiguous" event consistent with a BHNS nature would be the first hint of the existence of "light" stellar BHs, confuting the mass-gap. This would provide new constraints on the NS maximum mass and equation of state, and it would strongly impact the supernova explosion models, favoring those producing a continuum spectrum of remnant masses.

I presented a method to optimize the EM follow-up campaigns, based on the knowledge of the system's chirp mass. With this information, the compatible NSNS and BHNS configurations can be obtained and the expected ranges of kilonova light curves in different bands can be computed. The probability of detecting the EM counterpart of a GW event could be enhanced if the observation of transients consistent at their first detection with the expected kilonova ranges was prioritized for photometric and/or spectroscopic follow-up.

Finally I studied the EM counterparts properties distributions of future NSNS and BHNS mergers detected with gravitational waves. This could represent another useful contribution for EM follow-up strategy organization.

Keywords: *Neutron stars*, *Black holes*, *Binaries*, *Gravitational waves*, *Kilonovae*, *Gamma-ray burst*.

LIST OF FIGURES

2.1 Simple representation of deformations induced by "plus" and "cross" polarized GWs on a freely-falling particles ring. 9

2.2 Comparison of example GW signals observed in LIGO Livingston with respect to the detector's sensitivity. 14

2.3 Parameter estimation results for the BHBH merger GW190412. 16

3.1 Relative probability for each remnant scenario for a population of NSNS binary mergers, assuming two EoS. 19

3.2 Simple sketch representing the outcome of NSNS/BHNS mergers. . . . 22

4.1 Sketch of a section in the dynamical ejecta. 34

4.2 Example kilonova light curves showing the contribution from each ejecta component and the main dependences on ejecta properties. 37

5.1 Schematic representation of a GRB jet. 39

5.2 NSNS merger configurations producing long-lived NSs or BHs. 41

5.3 NSNS merger configurations producing a successful jet. 42

5.4 Angular distribution of the Lorentz factor and of the isotropic equivalent energy in the jet. Observed prompt emission isotropic equivalent energy as a function of the observer's viewing angle. 45

5.5 Schematic representation of jet's head sub-regions. 46

5.6 Schematic representation of observer's position with respect to a given jet's head sub-region. 46

5.7 Example GRB afterglow light curves, showing the dependence on the observer's viewing angle. 51

5.8 Simple sketch showing how the viewing angle affects the observed GRB afterglow light curve. 52

6.1 NSNS dynamical ejecta and accretion disc mass dependence on the NS masses for different EoS. 55

6.2 NSNS kilonova light curves dependence on binary properties and EoS. . 56
6.3 NSNS GRB afterglow radio light curves dependence on binary properties and EoS. 56
6.4 BHNS dynamical ejecta and accretion disc mass dependence on the binary parameters. 58
6.5 BHNS Kilonova light curves dependence on binary properties and EoS. 59
6.6 BHNS GRB afterglow light curves dependence on binary properties and EoS. 60
6.7 BHNS systems whose kilonova mimic the GW170817 observed light curve. 60
6.8 Example of binary components' masses constraints given by the inferred chirp mass. 62
6.9 Corner plot for MCMC run with $M_{\rm BH}$, $\chi_{\rm BH}$, $M_{\rm NS}$ and $\Lambda_{\rm NS}$ as free parameters. 64
6.10 Kilonova computed using the best-fitting parameters compared to mock light curves. 64
6.11 Corner plot for MCMC run with $M_{\rm BH}$, $\chi_{\rm BH}$ and $M_{\rm NS}$ as free parameters (fixing the EoS). 65
6.12 Classification scheme for compact object binaries, showing the "ambiguous" chirp mass range. 66
6.13 Dynamical ejecta and accretion disc masses from NSNS and BHNS configurations compatible with the same chirp mass. 67
6.14 Expected ranges of kilonova light curves from NSNS and BHNS mergers consistent with the considered "ambiguous" chirp masses. 68
6.15 Binary configurations consistent with the inferred chirp mass for GW190425. 70
6.16 Dynamical ejecta and accretion disc masses for different NSNS/BHNS configurations consistent with the inferred chirp mass for GW190425. . 71
6.17 Kilonova light curves ranges for NSNS/BHNS configurations consistent with the inferred chirp mass for GW190425. 72
6.18 First detections of promising candidates as kilonova from GW190425, compared with expected kilonova ranges from NSNS/BHNS systems consistent with the GW190425 chirp mass. 74

6.19 Considered BH spin distributions. 77
6.20 Cumulative BHNS intrinsic merger rate and detection rates. 80
6.21 Cumulative NSNS intrinsic merger rate and detection rates. 81
6.22 BHNS kilonova and GRB afterglow peak properties distributions, for events whose GW signal is detectable. 84
6.23 NSNS kilonova and GRB afterglow peak properties distributions, for events whose GW signal is detectable. 85

LIST OF TABLES

3.1 Ejecta properties for NSNS and BHNS mergers. 23

6.1 MCMC best-fitting parameters. 63

6.2 Horizon distances and local ($z < 0.1$) detection rates in the different channels for the `Startrack` BHNS population and the two BH spin distributions. 80

6.3 Same as Table 6.2, for the `MOBSE` BHNS population. 81

6.4 Horizon distances and local ($z < 0.1$) detection rates in the different channels for the `Startrack` NSNS population. 82

6.5 Same as Table 6.4, for the `MOBSE` NSNS population. 82

LIST OF TERMS AND ABBREVIATIONS

GW	Gravitational Wave
LVC	LIGO/Virgo Collaboration
LVK	LIGO/Virgo/KAGRA Collaboration
BH	Black Hole
NS	Neutron Star
EM	Electromagnetic
sGRB	Short Gamma-Ray Burst
LGRB	Long Gamma-Ray Burst
ISM	Interstellar Medium
KN	Kilonova
EoS	Equation of State
ISCO	Innermost Stable Circular Orbit
PE	Parameter Estimation
Pan-STARRS	Panoramic Survey Telescope and Rapid Response System
GR	General Relativity
TT	Transverse-Traceless
PN	Post-Newtonian
NR	Numerical Relativity
HMNS	Hyper-Massive Neutron Star
SMNS	Supra-Massive Neutron Star
SNR	Signal-to-Noise Ratio
SN	Supernova
BATSE	Burst And Transient Source Experiment
GRHD	General-relativistic hydrodynamic
GCN	Gamma-ray Coordinates Network

MCMC	Markov Chain Monte Carlo
NICER	Neutron Star Interior Composition Explorer
BNS	Binary Neutron Star
BBH	Binary Black Hole
GROWTH	Global Relay of Observatories Watching Transients Happen

CHAPTER 1

Introduction

1.1 Context

Since 2015 the LIGO-Virgo Scientific Collaboration (LVC) detected gravitational waves (GW) from the inspiral and merger of several black hole - black hole binaries (BHBH) (LVC 2019*d*, Nitz et al. 2019). On 17 August 2017, the first GW signal from the coalescence of a double neutron star binary (NSNS) was detected (GW170817, LVC 2017*b*,*a*). This event was accompanied by electromagnetic (EM) counterparts covering a broad-band spectrum (Soares-Santos et al. 2017, Cowperthwaite et al. 2017, Nicholl et al. 2017, Chornock et al. 2017, Margutti et al. 2017, Alexander et al. 2017), marking the beginning of the multi-messenger astronomy. On 25 April 2019 the second NSNS merger was detected (GW190425, LVC 2020*c*), without any firlmy associated EM counterpart. Furthermore, during the last observing run O3, several promising candidates for NSNS and black hole - neutron star binary (BHNS) mergers were reported[1], without any associated EM counterpart.

The expected intrinsic NSNS and BHNS merger rates from population synthesis models are, respectively, $3 \times 10^{-7} \lesssim \mathcal{R}_{\rm NSNS} \lesssim 4 \times 10^{-6}$ Mpc^{-3} yr^{-1} and $6 \times 10^{-10} \lesssim \mathcal{R}_{\rm BHNS} \lesssim 10^{-6}$ Mpc^{-3} yr^{-1} (LVC 2010, Coward et al. 2012, Petrillo et al. 2013, Dominik et al. 2015, de Mink and Belczynski 2015, Fong et al. 2015, Mapelli and Giacobbo 2018, Giacobbo and Mapelli 2018, Artale et al. 2019, Rastello et al. 2020). The expected NSNS and BHNS detection rates for O3 were, respectively, $1.3 \lesssim \mathcal{R}_{\rm NSNS,det} \lesssim 6.9$ yr^{-1} and $0.04 \lesssim \mathcal{R}_{\rm BHNS,det} \lesssim 12$ yr^{-1} (Dominik et al. 2015).

The detection of EM counterparts from GW170817 demonstrated that NSNS mergers are possible progenitors of short Gamma-ray burst (sGRB, as proposed in Eichler et al. 1989, Narayan et al. 1992) and sites for r-process nucleosynthesis, producing heavy elements whose radioactive decay powers an ultraviolet-optical-infrared transient emission, called “kilonova” (KN) (Lattimer and Schramm 1974, Li and Paczyński 1998, Metzger 2019). Moreover the relativistic jet launched after the merger, that causes sGRB emission (also called GRB Prompt), subsequently propagates into the

---

[1] The list of O3 candidates is available on the LVC Public Alerts webpage `https://gracedb.ligo.org/superevents/public/O3/`.

Inter-Stellar Medium (ISM) and interacts with it, producing the GRB Afteglow emission (Sari et al. 1998, Salafia et al. 2019a).

The EM counterparts are produced only if some material remains outside the final remnant of the merger. During the last phase of inspiral, the NSs are partially tidally disrupted, producing some gravitationally unbound material (called "dynamical ejecta", also produced by shocks in NSNS mergers when the two stars' crusts collide) and an accretion disc around the remnant object. Sevaral processes can produce outflows from the disc ("wind" and "secular" ejecta), while its accretion onto the remnant powers the launch of a relativistic jet (if the remnant is a BH). NSNS mergers are always expected to produce EM counterparts, as for all binary configurations tidal disruption and/or collision shocks happen (Radice et al. 2018a, Kiuchi et al. 2019, Radice et al. 2020). It is anticipated that BHNS mergers can produce EM counterparts as well, if the NS is tidally disrupted outside the BH's innermost stable circular orbit (ISCO) (otherwise the NS experiences a "direct plunge" and no material remains outside the remnant BH) (Shibata and Taniguchi 2011, Foucart 2012, Kyutoku et al. 2015, Kawaguchi et al. 2015, Foucart et al. 2018).

Different works in the literature showed that a combined analysis of EM and GW data from a NSNS merger helps constraining the binary's parameters (i.e. component masses, NS tidal deformabilities, viewing angle, distance) and the Equation of State (EoS) of matter at supra-nuclear densities (Margalit and Metzger 2017, LVC 2018*b*, Radice et al. 2018b, Finstad et al. 2018, Raithel et al. 2018, Margalit and Metzger 2019, Coughlin et al. 2019). Prospects for multi-messenger analysis for BHNS mergers have been widely discussed, showing that a great deal of information on the underlying physics can be obtained (Pannarale and Ohme 2014, Coughlin et al. 2017, Coughlin and Dietrich 2019).

Furthermore multi-messenger observations are fundamental to distinguish the nature of the merging system for events that can not be firmly classified through the GW signal alone (Mandel et al. 2015). The LVC classifies the coalescing binaries according to the value of their chirp mass (a combination of the two component masses) that is one of the most precisely measured parameter from the GW signal. If we assume that BH and NS mass distributions are adjacent (no "mass-gap"), there exist a range of "ambiguous" chirp mass values compatible with both NSNS and BHNS systems. Therefore for these events the EM counterpart detection is necessary to disentangle the nature of the binary. As an example, the inferred chirp mass for GW190425 is "ambiguous", thus the presence of a BH in the binary can not be excluded (LVC 2020*c*, Kyutoku et al. 2020, Han et al. 2020). Unfortunately no EM counterpart for that event was detected, thus no further information is available.

Therefore the EM counterpart detection is crucial for a better characterization of the merging system and a deeper understanding of the underlying physics involved. From the observational point of view this is very challenging. Indeed from the GW signal the estimated sky-localisation can be poorly informative (up to $\sim$thousands deg^2). Combined with the distance uncertainty, this would imply a volume error box containing $\sim$thousands of galaxies (for a comparison, the GW170817 localisation volume contained $\sim$180 galaxies, see Arcavi et al. 2017). Among the thousands of transients in the sky-area the identification of the one associated with the GW signal is very challenging, and rapidly decaying EM counterparts (if not all of them) would be lost. Therefore some criteria to optimise the EM follow-up strategy would be very useful to enhance the probability of discovering the EM counterpart of the merger.

1.2 My contribution

In Barbieri et al. (2020a) I developed a series of versatile semi-analytical models to predict the expected multi-wavelength emission that accompanies BHNS mergers. I included the nuclear-decay-powered kilonova emission (both from dynamical ejecta and disc outflows), its radio remnant, the prompt emission from the jet and the related GRB afterglow. The developed models compare well with other more sophisticated (but also more computationally expensive) results in the literature (i.e. Kawaguchi et al. 2020). For what concerns the KN emission, insights from general relativity numerical simulations indicate that ejecta properties (such as composition and geometry) can be very different in BHNS and NSNS mergers, in particular for the dynamical ejecta. I extended the model presented in Perego et al. (2017) (that in turn is an extension of Grossman et al. 2014 and Martin et al. 2015) for the contribution of disc winds to the BHNS case. For the dynamical ejecta I defined a new model to calculate its contribution to the KN according to the peculiar geometrical distribution expected from simulations (Kawaguchi et al. 2016, Fernández et al. 2017, Foucart et al. 2019). The kilonova radio remnant is produced when the ejecta decelerate through interaction with the ISM (likewise GRB afterglow emission). I modeled this emission improving Hotokezaka and Piran (2015), using the ejecta geometrical properties expected from BHNS simulations instead of assuming spherical symmetry. For what concerns the relativistic jet launch, I modeled how it interacts with the environment and how this interaction affects its structure (Salafia et al. 2019b). Finally I modeled the prompt and afterglow emission following Salafia et al. (2015) and Salafia et al. (2019a). My model has been used in Ackley et al. (2020) to constrain the ejecta and binary properties for the BHNS merger candidate S190814bv and in McBrien et al. (2020) to discuss the nature of a promising kilonova candidate from the Panoramic Survey Telescope and Rapid Response System (Pan-STARRS) search.

The properties of the aforementioned counterparts depend upon those of the outflows that result from the partial disruption of the NS during the merger and from the accretion disc around the remnant. These are necessary ingredients for transient EM emission to accompany the GW signal. I therefore adopted fitting formulae in the literature (Kawaguchi et al. 2016, Foucart et al. 2018, Radice et al. 2018a, Salafia et al. 2020, calibrated on general-relativistic numerical simulations) to relate the properties of these outflows to those of the progenitor binary, establishing a link between the binary parameters and the counterpart properties (Barbieri et al. 2019a, 2020a,b). In NSNS mergers the EM emission is mainly governed by the NSs's masses M_1 and M_2 and their tidal deformabilities Λ_1 and Λ_2. Dynamical ejecta and accretion disc mass production is favoured in binaries with large $\Lambda_{1,2}$ or, equivalently, "stiff" EoS. In particular dynamical ejecta production is favoured in binaries with large mass ratio $q = M_1/M_2$, while larger disc masses are produced for large mass ratios or equal-mass systems with very light NSs. In BHNS mergers the EM emission is mainly governed by the NS mass $M_{\rm NS}$, its tidal deformability $\Lambda_{\rm NS}$, the BH mass $M_{\rm BH}$ and its spin $\chi_{\rm BH}$. Tidal disruption is favoured in binaries with low mass ratio $q = M_{\rm BH}/M_{\rm NS}$ and large $\Lambda_{\rm NS}$ (corresponding to a small $M_{\rm NS}$ and/or to a "stiff" equation of state). A large $\chi_{\rm BH}$, that brings ISCO closer to the BH horizon, also greatly enhances the tidal disruption.

In Barbieri et al. (2019a, 2020a) I anticipated the variety of multi-bands light curves that can emerge from a BHNS merger, from radio to gamma-rays. These light curves show universal traits, related to the dynamics of the emitting outflows, but they also present clear dependences on the binary properties, though there is an high degree of degeneracy. In Barbieri et al. (2019a) I showed how joint GW+EM analysis can reduce this degeneracy, performing a proof-of-concept multi-messenger parameter estimation, considering a BHNS merger with an associated kilonova. My results indicate that joint analysis can lead to better constraints on the binary parameters (i.e. the BH spin).

Moreover, in Barbieri et al. (2019b) I analysed the case of coalescing compact-object binaries whose chirp mass is "ambiguous". For these events the nature of the binary may not be identified through the GW signal alone. As mentioned before, the properties of the binary are encoded in those of the ejecta, and therefore in those of the EM counterparts. In particular I focused on the KN and I found that in the BHNS case it can be far more luminous with respect to the NSNS case, even assuming non-spinning BHs. This happens because, in the considered chirp mass interval, the mass ejection in the majority of NSNS configurations is at its worst (the system promptly forms a BH, producing few ejecta). Instead mass ejection for the majority of BHNS configurations is at its best as the mass ratios are small and the NSs have low mass/large deformability. This work shows again the potential of joint GW+EM detections, where information from one "channel" can improve the amount of information obtainable from the other.

In Barbieri et al. (2020b) I applied the previous analysis to the GW190425 event (whose inferred chirp mass is "ambiguous"). In agreement with other works (i.e. Kyutoku et al. 2020), I found that the presence of a BH in the binary would have produced a brighter KN with respect to the NSNS case, that would have been detectable if the source had been precisely localised. In such a case, the KN observation could have disentangled the nature of the merging system.

As explained above, the identification of the EM counterparts associated with a GW signal source is very challenging, due to the large volume error box. In Barbieri et al. (2020b) I presented a method to optimise the EM follow-up campaigns, based on the knowledge of the system's chirp mass. With this information, the compatible NSNS and BHNS configurations can be obtained. Then, assuming an EoS, the expected ranges of KN light curves in different bands can be calculated. The probability of detecting the EM counterpart of a GW event could be enhanced if the observation of transients consistent at their first detection with the expected KN ranges was prioritized for photometric and/or spectroscopic follow-up. I applied this method to GW190425 EM follow-up campaign, finding that two of the initial promising counterpart candidates (there were observed for $\sim$1 day before being classified as supernovae) were not consistent with the expected KN range at their first detection. Thus observation of other transients could have been prioritized.

Finally, as a preparation work for a future paper (Barbieri et al. 2020c) I used NSNS and BHNS populations (from existing synthesis codes) to estimate the expected detection rates and horizon distances in O3. I considered all the possible "channels" for the detection: GWs, KN, GRB prompt and afterglow emission, as well as joint multi-messenger detections. For populations from Dominik et al. (2012, 2013) I found detection rates and horizons consistent with the O3 reported candidates. Finally, for the events whose GW signal is detectable, I analysed the distribution of the KN and GRB afterglow peak properties (time and magnitude/flux) in different bands. This could be another useful contribution for EM follow-up strategy organisation.

CHAPTER 2

Gravitational Waves

In this chapter I present the basic physics of GW emission during compact binary sistems' coalescence. In §2.1 I summarise general relativity (GR) basic concepts that lead to the formulation of GW equation. In §2.2 I describe the inspiral and merger phases of compact binaries. Arguments in these two sections are presented following Maggiore (2008) (see also references therein). In §2.3 I present the binary parameters that can be inferred from the GW signal analysis.

2.1 Basic physics of GWs

The differential line element ds in the $\mathbf{x}$ point of the space-time is

$$ds^2 = g_{\alpha\beta}(\mathbf{x}) dx^\alpha dx^\beta, \tag{2.1}$$

where $g_{\alpha\beta}$ is the metric tensor. Note that repeated indices indicate summation (Einstein's notation). The simpliest metric tensor is the Minkowski metric, descriving a flat space in Cartesian coordinates

$$g_{\alpha\beta}(\mathbf{x}) = \begin{pmatrix} -1 & 0 & 0 & 0 \\ 0 & 1 & 0 & 0 \\ 0 & 0 & 1 & 0 \\ 0 & 0 & 0 & 1 \end{pmatrix}, \tag{2.2}$$

where $\alpha = (t, x, y, z)$. Instead the curved space-time outside a spherically simmetric mass distribution is described in spherical coordinates by the Schwarzschild metric

$$g_{\alpha\beta}(\mathbf{x}) = \begin{pmatrix} -(1 - 2GM/c^2r) & 0 & 0 & 0 \\ 0 & (1 + 2GM/c^2r)^{-1} & 0 & 0 \\ 0 & 0 & r^2 & 0 \\ 0 & 0 & 0 & r^2 \sin^2\theta \end{pmatrix}, \tag{2.3}$$

where $\alpha = (t, r, \theta, \phi)$, M is the total mass, G is the gravitational constant and c is the speed of light.

The Riemann curvature tensor is defined as

$$R^{\alpha}_{\beta\gamma\delta} = \frac{\partial \Gamma^{\alpha}_{\beta\delta}}{\partial x^{\gamma}} - \frac{\partial \Gamma^{\alpha}_{\beta\gamma}}{\partial x^{\delta}} + \Gamma^{\alpha}_{\gamma\epsilon}\Gamma^{\epsilon}_{\beta\delta} - \Gamma^{\alpha}_{\delta\epsilon}\Gamma^{\epsilon}_{\beta\gamma}, \tag{2.4}$$

where Γ is the Christoffel symbol, given by

$$g_{\alpha\delta}\Gamma^{\delta}_{\beta\gamma} = \frac{1}{2}\Big(\frac{\partial g_{\alpha\beta}}{\partial x^{\gamma}} + \frac{\partial g_{\alpha\gamma}}{\partial x^{\beta}} + \frac{\partial g_{\beta\gamma}}{\partial x^{\alpha}}\Big). \tag{2.5}$$

The Ricci tensor is obtained from the Riemann tensor by contracting two indices:

$$R_{\beta\delta} = R^{\alpha}_{\beta\alpha\delta}. \tag{2.6}$$

The scalar curvature is defined as the trace of the Ricci curvature tensor with respect to the metric:

$$R = g^{\alpha\beta}R_{\alpha\beta}. \tag{2.7}$$

The stress-energy tensor $T_{\alpha\beta}$ describes the density and flux of energy and momentum in the space-time. The "time-time" component ($\alpha = \beta = 0$) represents the energy density divided by c^2. The "time-space" components ($\alpha = 0$ and $\beta = i$, with $i = 1, 2, 3$) represent the density of the i-th component of the linear momentum. The diagonal "space-space" components ($\alpha = \beta = i$ with $i = 1, 2, 3$) represent the normal stresses (pressure), while the off-diagonal "space-space" components ($\alpha = i$ and $\beta = j$ with $i = 1, 2, 3$, $j = 1, 2, 3$ and $i \neq j$) represent the shear stresses. The stress-energy tensor is symmetric, thus $T_{\alpha\beta} = T_{\beta\alpha}$.

With all these ingredients one of the most famous, important and innovative equation in physics, the Einstein's equation, can be written:

$$R_{\alpha\beta} - \frac{1}{2}g_{\alpha\beta}R = \frac{8\pi G}{c^4}T_{\alpha\beta}. \tag{2.8}$$

This relation describes how matter curves the space-time and how curvature influences matter. Starting from eq. 2.8, the GW equation can be derived using a perturbative approach. For simplicity, one can start from a background Minkowski metric $\eta_{\alpha\beta}$ (any other more complex metric could be considered as well). Let us consider some sources, described by a stress-energy tensor $T_{\alpha\beta}$, producing a small perturbation $h_{\alpha\beta}$. The metric of the perturbed space-time is

$$g_{\alpha\beta}(\mathbf{x}) = \eta_{\alpha\beta} + h_{\alpha\beta}(\mathbf{x}). \tag{2.9}$$

$h_{\alpha\beta}$ is a small perturbation, thus $|h_{\alpha\beta}| \ll |\eta_{\alpha\beta}| = 1$ (linearized theory). One can simplify the left hand side of eq. 2.8 keeping only leading order terms in $h_{\alpha\beta}$ and applying the Lorentz gauge condition:

$$\partial_\beta h^\beta_\alpha(\mathbf{x}) - \frac{1}{2}\partial_\alpha h^\beta_\beta(\mathbf{x}) = 0. \tag{2.10}$$

In vacuum, where $T_{\alpha\beta} = 0$, the homogeneous wave equation is

$$\Box h_{\alpha\beta}(\mathbf{x}) = 0, \tag{2.11}$$

where $\Box$ is the D'Alambertian operator

$$\Box = \eta^{\alpha\beta}\frac{\partial}{\partial x^\alpha}\frac{\partial}{\partial x^\beta} = -\frac{1}{c^2}\frac{\partial^2}{\partial t^2} + \nabla^2, \tag{2.12}$$

implying that GWs propagate at the speed of light. Fixing a wave vector $\vec{k}$, a solution of eq. 2.11 is

$$h_{\alpha\beta}(\mathbf{x}) = A_{\alpha\beta}e^{i(\vec{k}\cdot\vec{x}-\omega t)}, \tag{2.13}$$

where A is a 4x4 symmetric matrix and $\omega = kc$. One can impose the "transverse-traceless gauge" (TT-gauge)

$$h_{0,\alpha} = 0 \text{ with } \alpha = 0,1,2,3;\ h^\alpha_\alpha = 0 \text{ with } \alpha = 1,2,3; \tag{2.14}$$

to make the metric perturbation purely spatial and traceless. Then the Lorentz gauge condition implies that the spatial metric perturbation is transverse $\partial_\alpha h_{\alpha\beta} = 0$ with α,β=1,2,3. For a GW propagating in the z direction

$$h_{\alpha\beta}(\mathbf{x}) = \begin{pmatrix} 0 & 0 & 0 & 0 \\ 0 & h_+ & h_\times & 0 \\ 0 & h_\times & h_+ & 0 \\ 0 & 0 & 0 & 0 \end{pmatrix} e^{i(kz-\omega t)}, \tag{2.15}$$

where h_+ and $h_\times$ are the amplitudes of the "plus" and "cross" polarizations (see Fig. 2.1). Thus the degrees of freedom of a GW are the two possible polarization states.

In flat space-time and assuming TT-gauge, the inhomogeneous wave equation is

$$\Box h_{\alpha\beta}(\mathbf{x}) = -\frac{16\pi G}{c^4}T_{\alpha\beta}. \tag{2.16}$$

Eq. 2.16 has the same form of the wave equation for relativistic electrodynamic fields. Therefore the solution can be obtained is a similar way as

$$h_{\alpha\beta}(t,\vec{x}) = \frac{4G}{c^4}\int d^3x' \frac{[T_{\alpha\beta}(t',\vec{x}')]_{\mathrm{ret}}}{|x-x'|}, \tag{2.17}$$

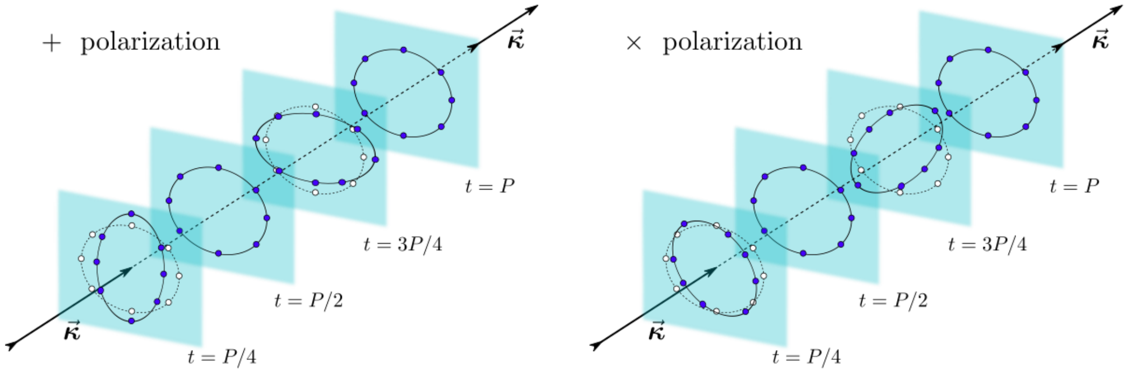

Fig. 2.1 Simple representation of deformations induced by “plus” and “cross” polarized GWs on a freely-falling particles ring. Dark dots indicate the particles’ position at different times. White dots indicate the unperturbed positions. Image from Bishop and Rezzolla (2016), copyright by the authors.

where the subscript ”ret” indicates the evaluation at the retarded time $t' = t - |\vec{x} - \vec{x}'|/c$. The factor $4G/c^4 \sim 3.4 \times 10^{-49}$ s^2 g^{-1} cm^{-1} is very small. Indeed the GW detection is very challenging.

Every massive object produces GWs when it accelerates but, due to the very small amplitude, very rapid accelerations and huge masses are needed to produce detectable signals. There are four categories of GWs, based on different sources:

- Continuous GWs, produced by a spinning massive object (i.e. a NS) due to some imperfections on its shape (breaking down spherical symmetry). If the rotational velocity is constant, so are the frequency and amplitude of the GW.

- Compact binary inspiral GWs, produced by systems hosting two compact (massive and dense) objects (i.e. white dwarves, NSs and BHs) orbiting each other. During each revolution, the system looses orbital energy through GW emission and the objects come closer and closer. Tighter the orbit, faster the objects’ velocity, stronger the GW emission, more intense the orbital energy loss, closer the orbit and so on until the two objects merge. The GW signal has increasing amplitude and frequency during the orbiting phase (inspiral) and rapidly reaches the maximum amplitude very close to merger (chirp). More massive systems evolve faster, thus their final inspiral phase has a smaller duration with respect to lighter systems.

- Stochastic GWs, produced by all the possible sources in the Universe from every direction, representing a random background with very small amplitude. It is possible that one of the components are relic GWs from the Big Bang.

- Burst GWs, representing unmodeled signals from unknown sources (some hypothetical sources are supernovae and GRBs).

In this work I consider GWs from NSNS and BHNS mergers, thus the second category.

2.2 Coalescence of compact binaries

The term "compact binaries" indicates binary systems whose components are compact objects (BHs or NSs[1]), representing the relics of massive stars' evolution. In the current LVC network configuration BHBH, BHNS and NSNS mergers are detectable in the last inspiral phase (from $\sim$ fractions of second before the merger for BHBH to ~ 100 seconds for NSNS). In this infinitesimal time with respect to the binary's lifetime (from Myr to Gyr) the components emit a considerable fraction of their reduced mass-energy as GWs.

In Newtonian gravity two binary point masses move on circular/elliptical orbits around the system's center of mass. The Keplerian frequency is $f_{\rm K} = (GM_{\rm tot}/a^3)^{1/2}/(2\pi)$, with a the orbit's semi-major axis and $M_{\rm tot}$ the system's total mass. In GR GWs emission causes a loss of orbital energy and angular momentum, decreasing a and increasing $f_{\rm K}$.

The first and long lasting phase is the "inspiral", during which the two objects can be considered as point masses whose dynamics is described by Post Newtonian (PN) theory (Blanchet 2014). During this phase the amplitude and frequency of the GWs slowly increase. Thanks to its long duration, the signal from inspiral is fundamental to constrain the binary parameters by matching it with waveform templates.

The second phase is the "merger", including the last orbits and the coalescence. During this phase, due to the strong gravitational fields and the extreme velocity ($\sim 1/3\,c$), PN formalism is no longer valid and the system can be described only with Numerical Relativity (NR). Finite-size effects must be taken into account for NSs, as they are characterised by a surface and they are deformable. NR simulations including the non-linearities of the Einstein's equation can accurately describe the system's dynamics and GW emission.

The final phase is the "ringdown", through which the system reaches a new stationary equilibrium. The particular shape of the GW signal in this phase depends on the remnant properties. For BHBH and BHNS mergers the remnant is obviously a BH. For NSNS mergers the remnant can be a BH, an unstable hyper-massive NS (HMNS) or supra-massive NS (SMNS) that after some time collapses to a BH, or a stable NS, depending on the total mass of the system and the EoS.

---

[1] We do not consider white dwarves as the expected GW frequencies from binaries containing them are outside the current LVC network sensitivity range.

2.2.1 Energy loss and GW signal frequency evolution

The reference frequency for GWs from coalescing compact binaries is

$$f_{\rm coal} = \frac{c^3}{\pi 6^{3/2} GM}, \tag{2.18}$$

representing the double of $f_{\rm K}$ for a test mass particle orbiting at the innermost stable circular orbit $R_{\rm ISCO}$ around a Schwarzschild BH (non-spinning) with mass M. The binary's "chirp mass" $M_{\rm c}$ is defined as

$$M_{\rm c} = \frac{(M_1 M_2)^{3/5}}{(M_1 + M_2)^{1/5}}, \tag{2.19}$$

where M_1 and M_2 are the components's masses, with $M_1 > M_2$. Defining the binary's symmetric mass ratio $\nu = M_1 M_2 / M_{\rm tot}^2$ and reduced mass $\mu = M_1 M_2 / M_{\rm tot}$, the chirp mass can be also expressed as $M_{\rm c} = \nu^{3/5} M_{\rm tot} = \mu^{3/5} M_{\rm tot}^{2/5}$. During the inspiral, the GW luminosity averaged over a period (assuming a circular orbit) can be described to the leading order as

$$\dot{E}_{\rm GW}^{\rm circ} = \frac{32 c^5}{5G} \Big(\pi \frac{G M_{\rm c}}{c^3} f \Big)^{10/3} = \frac{32 c^5}{5 \cdot 6^5 G} \nu^2 \tilde{f}^{10/3}, \tag{2.20}$$

where $f = 2 f_{\rm K}$ is the emitted GW frequency and $\tilde{f} = f / f_{\rm coal}$. Close to coalescence ($\tilde{f} \sim 1$) the GW luminosity depends only on the symmetric mass ratio: $\dot{E}_{\rm GW}^{\rm circ}(\tilde{f} \sim 1) \sim 3.6 \times 10^{59} \nu^2$ erg s^{-1}.

The binary orbital angular momentum L loss rate is (averaging over a period and considering circular orbits)

$$\dot{L}_{\rm GW}^{\rm circ} = \frac{32}{5} M_{\rm c} c^2 \Big(\frac{G M_{\rm c}}{c^3} \pi f \Big)^{7/3} = \frac{32}{5 \cdot 6^{7/2}} \nu^2 M_{\rm tot} c^2 \tilde{f}^{7/3}. \tag{2.21}$$

Close to coalescence, $\dot{L}_{\rm GW}^{\rm circ}$ depends on $M_{\rm tot}$ and ν: $\dot{L}_{\rm GW}^{\rm circ}(\tilde{f} \sim 1) \sim 32 \nu^2 M_{\rm tot} c^2 / (5 \cdot 6^{7/2})$.

According to the virial theorem, the binary's orbital energy is

$$E_{\rm bin} = -\frac{G \nu M_{\rm tot}^2}{2a} = -\frac{1}{2} \nu M_{\rm tot}^2 (G M_{\rm tot})^{1/3} (\pi f)^{2/3}. \tag{2.22}$$

From energy conservation $\dot{E}_{\rm bin} = -\dot{E}_{\rm GW}$. Calculating $dE_{\rm bin}/df$ from eq. 2.22 and considering $\dot{E}_{\rm bin} = dE_{\rm bin}/df \times df/dt$, the frequency evolution can be obtained:

$$\dot{f} = \frac{96}{5} \pi^{8/3} \Big(G M_{\rm c} / c^3 \Big)^{5/3} f^{11/3}. \tag{2.23}$$

This relation shows that the GW frequency evolution depends only on the chirp mass (to the first order, considering circular orbits). Solving eq. 2.23 one can find the time dependence of the GW frequency

$$f(t) = \frac{5^{3/8}}{(256)^{3/8}\pi}\Big(\frac{GM_{\rm c}}{c^3}\Big)^{-5/8}(t_{\rm coal} - t)^{-3/8}, \tag{2.24}$$

where $t_{\rm coal}$ is the time of the merger. Inverting this relation, the remaining time to merger as a function of the GW frequency is

$$\tau^{\rm circ}(f) = \frac{5}{256\pi^{8/3}\nu f^{8/3}}\Big(\frac{c^3}{GM_{\rm tot}}\Big)^{5/3} \tag{2.25}$$

or, as a function of $\tilde{f}$,

$$\tau^{\rm circ}(\tilde{f}) = \frac{6480 GM_{\rm tot}}{256 c^3 \nu \tilde{f}^{8/3}}. \tag{2.26}$$

Finally the energy spectrum $dE_{\rm gw}/df$ and the total energy radiated in GWs $E_{\rm GW}$ are (in the quadrupole approximation)

$$\frac{dE_{\rm gw}}{df} = \frac{\pi^{2/3}}{3G}(GM_{\rm c})^{5/3}f^{-1/3}; E_{\rm GW} \sim \frac{\pi^{2/3}}{2G}(GM_{\rm c})^{5/3}f_{\rm max}^{2/3}, \tag{2.27}$$

where $f_{\rm max}$ is maximum frequency at which the inspiral signal is observed.

2.3 GW signal analysis

2.3.1 Waveform and detection

The two polarisation states of the GWs emitted by a binary at distance d, assuming circular orbits, are

$$\begin{aligned} h_+(t) &= \frac{4}{d}\Big(\frac{GM_{\rm c}}{c^2}\Big)^{5/3}\Big(\frac{\pi f(t_{\rm ret})}{c}\Big)^{2/3}\frac{1+\cos^2\iota}{2}\cos\Phi_{\rm N}(t_{\rm ret}), \\ h_\times(t) &= \frac{4}{d}\Big(\frac{GM_{\rm c}}{c^2}\Big)^{5/3}\Big(\frac{\pi f(t_{\rm ret})}{c}\Big)^{2/3}\cos\iota\sin\Phi_{\rm N}(t_{\rm ret}), \end{aligned} \tag{2.28}$$

where ι is the angle between the observer's line of sight and the binary's orbital momentum, $f(t_{\rm ret})$ is the instantaneous GW frequency (eq. 2.24) evaluated at the retarded time $t_{\rm ret} = t - d/c$ and $\Phi_{\rm N} = 2\pi\int f(t')dt'$ is the lowest order contribution to the orbital phase. The latter quantity is given by

$$\Phi_{\rm N}(t) = \Phi_0 - 2\Big(\frac{5GM_{\rm c}}{c^3}\Big)^{-5/8}(t_{\rm coal} - t)^{5/8}, \tag{2.29}$$

where Φ_0 is the orbital phase at merger. Using eq. 2.19 h_+ and $h_\times$ result proportional to $\nu M_{\rm tot}^{5/3}$. Thus for a given $M_{\rm tot}$ the equal mass configuration produces a stronger GW signal with respect to unequal mass configurations. The ratio $h_+/h_\times$ depends on the angle ι. For face-on observers ($\iota = 0$ rad) the two polarisation components are out of phase by $\pi/2$ rad, while for edge-on observers ($\iota = \pi/2$ rad) $h_\times = 0$.

A single interferometer measures a linear combination of h_+ and $h_\times$, the "strain amplitude"

$$h(t) = F_+(\alpha, \delta, \psi)h_+ + F_\times(\alpha, \delta, \psi)h_\times, \tag{2.30}$$

where F_+ and $F_\times$ are the detector antenna pattern functions, describing the detector's response to each polarisation component depending on the source sky position. Indeed F_+ and $F_\times$ depends on the right ascension α, declination δ and polarisation angle ϕ Schutz (2011). By defining $F = \sqrt{F_+^2 + F_\times^2}$ and $\tan\xi = F_\times/F_+$ the strain amplitude can be written as $h(t) = F(t) \cdot [\cos(\xi)h_+ + \sin(\xi)h_\times]$, removing the dependence on ψ.

The signal is extracted from the detector's output through matched filtering techniques, obtaining the "effective strain amplitude“

$$h_{\text{eff}} = \sqrt{\mathcal{N}_{\text{cycles}}}h, \tag{2.31}$$

where $\mathcal{N}_{\text{cycles}} = \int_{f_{\min}}^{f_{\max}} (f/\dot{f})df$ is the number of cycles for which the GW signal remains in the detector's sensitivity frequency band. Using eq. 2.23 this quantity can be expressed as

$$\mathcal{N}_{\text{cycles}} = \frac{1}{32\pi^{8/3}}\Big(\frac{GM_{\text{c}}}{c^3}\Big)^{-5/3}\big(f_{\min}^{-5/3} - f_{\max}^{-5/3}\big). \tag{2.32}$$

Moreover, considering that $f_{\min} \ll f_{\max}$ and using $\tilde{f}$ eq. 2.32 can be simplified to

$$\mathcal{N}_{\text{cycles}}(\tilde{f}_{\min}) = \frac{6^{5/2}}{32\pi\nu}\tilde{f}_{\min}^{-5/3}. \tag{2.33}$$

Passing from time domain to frequency domain is convenient to compare GW waveforms with detector's sensitivity and to calculate the signal-to-noise ratio (SNR). The Fourier transforms of h_+ and $h_\times$ are

$$\begin{aligned}\tilde{h}_+(f) &= A\frac{c}{d}\Big(\frac{GM_{\text{c}}}{c^3}\Big)^{5/6}e^{i\phi_+(f)}\frac{1}{f^{7/6}}\Big(\frac{1+\cos^2\iota}{2}\Big),\\ \tilde{h}_\times(f) &= A\frac{c}{d}\Big(\frac{GM_{\text{c}}}{c^3}\Big)^{5/6}e^{i\phi_\times(f)}\frac{1}{f^{7/6}}\cos\iota,\end{aligned} \tag{2.34}$$

with $A = \sqrt{5/12}/\pi^{2/3}$. The Fourier transform of the strain amplitude, $\tilde{h}(f)$, includes the antenna pattern function. The SNR is then given by

$$\text{SNR}^2 = \int_0^\infty d\ln f\frac{|2\tilde{h}(f)\sqrt{f}|^2}{S_{\text{noise}}(f)}, \tag{2.35}$$

where $S_{\text{noise}}(f)$ is the "spectral strain sensitivity" [Hz^{-1}], describing the noise in the detector.

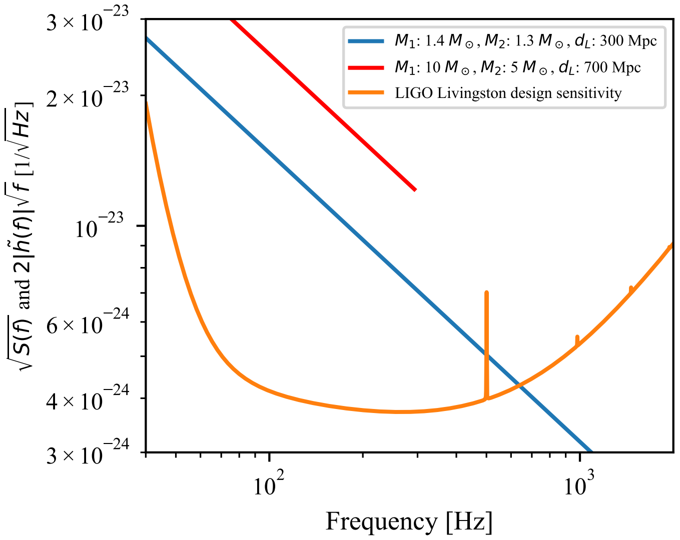

Fig. 2.2 Comparison of example GW signals observed in LIGO Livingston with respect to the detector's sensitivity $S_{\text{noise}}(f)$. The blue line represents $2\tilde{h}(f)\sqrt{f}$ for a NSNS merger with $M_1 = 1.4M_\odot$, $M_2 = 1.3M_\odot$ and $d_L = 300$ Mpc, while the red line represents a BHBH merger with $M_1 = 10M_\odot$, $M_2 = 5M_\odot$ and $d_L = 700$ Mpc. The orange line indicates the LIGO Livingston detector's design sensitivity.

Fig. 2.2 shows a comparison of example GW signals $2\tilde{h}(f)\sqrt{f}$ observed in LIGO Livingston with respect to the detector's sensitivity $S_{\text{noise}}(f)$, namely the numerator and denominator of the fraction in the integral of Eq. 2.35. It is interesting to note that the more massive system (BHBH with $M_1 = 10M_\odot$ and $M_2 = 5M_\odot$, red line) merges at a lower frequency with respect to the lighter one (NSNS with $M_1 = 1.4M_\odot$ and $M_2 = 1.3M_\odot$, blue line), as expected from Eq. 2.18. Indeed (neglecting stars' deformations) the two NSs merge when the orbit's radius is $\sim 20-25$ km (assuming that the stars's radii are $\sim 10-12$ km), while the two (non-spinning) BHs merge when the orbit's radius is ~ 45 km ($\sim$ the sum of their Schwarzschild radii).

2.3.2 Parameter estimation

The GW signal from a compact binary coalescence depends on intrinsic parameters, characterizing the system's dynamics and the waveform, and on extrinsic parameters, encoding the position of the source with respect to the detector network (LVC 2019*d*). For BHBH binaries the intrinsic parameters are the masses M_{i} and the spin vectors $\vec{S}_{\text{i}}$. The dimensionless spin vectors are defined as $\vec{\chi}_i = c\vec{S}_{\text{i}}/(GM_{\text{i}}^2)$, whose magnitude is limited in the range [0,1]. The individual spins are not precisely estimated from the GW signal, while a combination of the two, the effective aligned spin χ_{eff} is more constrained. χ_{eff} is the projection of the mass-weighted mean spin along $\hat{L}_{\text{N}}$, the normal to the orbital plane:

$$\chi_{\rm eff} = \frac{(M_1\vec{\chi}_1 + M_2\vec{\chi}_2)}{M_1 + M_2} \cdot \hat{L}_{\rm N} \tag{2.36}$$

The extrinsic parameters are the right ascension α, the declination δ, the luminosity distance $d_{\rm L}$, the polarization angle ψ, the viewing angle ι, the phase at coalescence $\phi_{\rm c}$ and the time of the merger $t_{\rm c}$.

As shown above, the GW phase evolution during the inspiral dependends at the leading order on the chirp mass $M_{\rm c}$. This quantity is more precisely measured for low-mass binaries (whose inspiral phase lasts longer and whose GW signal performs more cycles in the detector's band), while for massive binaries the relative error on $M_{\rm c}$ is larger. As an example, the relative error on the inferred chirp mass for GW170817 is less than 0.1%, while for BHBH events it is $\sim 5{-}15\%$. The system's mass ratio $q = M_1/M_2$ and $\chi_{\rm eff}$ affect the phase at higher orders. NSNS binaries have additional parameters, related to their deformation in a tidal field. The dominant term is the quadrupolar tidal deformation ($\ell = 2$), described by the dimensionless tidal deformability

$$\Lambda_{\rm i} = \frac{2}{3}k_2\Big(\frac{R_{\rm i}c^2}{GM_{\rm i}}\Big)^5, \tag{2.37}$$

where $R_{\rm i}$ is the NS radius and k_2 is the dimensionless Love number corresponding to $\ell = 2$ (Flanagan and Hinderer 2008), namely

$$k_2 = \frac{3}{2}G\lambda R_{\rm NS}^{-5}, \tag{2.38}$$

where λ is the quadrupolar polarizability (ratio of the induced quadrupole moment Q_{ij} and the tidal field E_{ij}), $Q_{ij} = -\lambda E_{ij}$. $\Lambda_{\rm NS}$ depends on the EoS and the NS mass. The GW phase is mostly affected by the binary effective tidal deformability parameter $\tilde{\Lambda}$, a combination of the individual Λs:

$$\tilde{\Lambda} = \frac{16}{13}\frac{(M_1 + 12M_2)M_1^4\Lambda_1 + (M_2 + 12M_1)M_2^4\Lambda_2}{M_{\rm tot}^5.} \tag{2.39}$$

Fig. 2.3 shows an example of parameter estimation results for the BHBH merger GW190412[2]. For simplicity I show only the samples for M_1, M_2, $q = M_2/M_1$, $M_{\rm c}$, $\chi_{\rm eff}$ and $d_{\rm L}$.

---

[2] Posterior samples publicly available at `https://dcc.ligo.org/LIGO-P190412/public/`

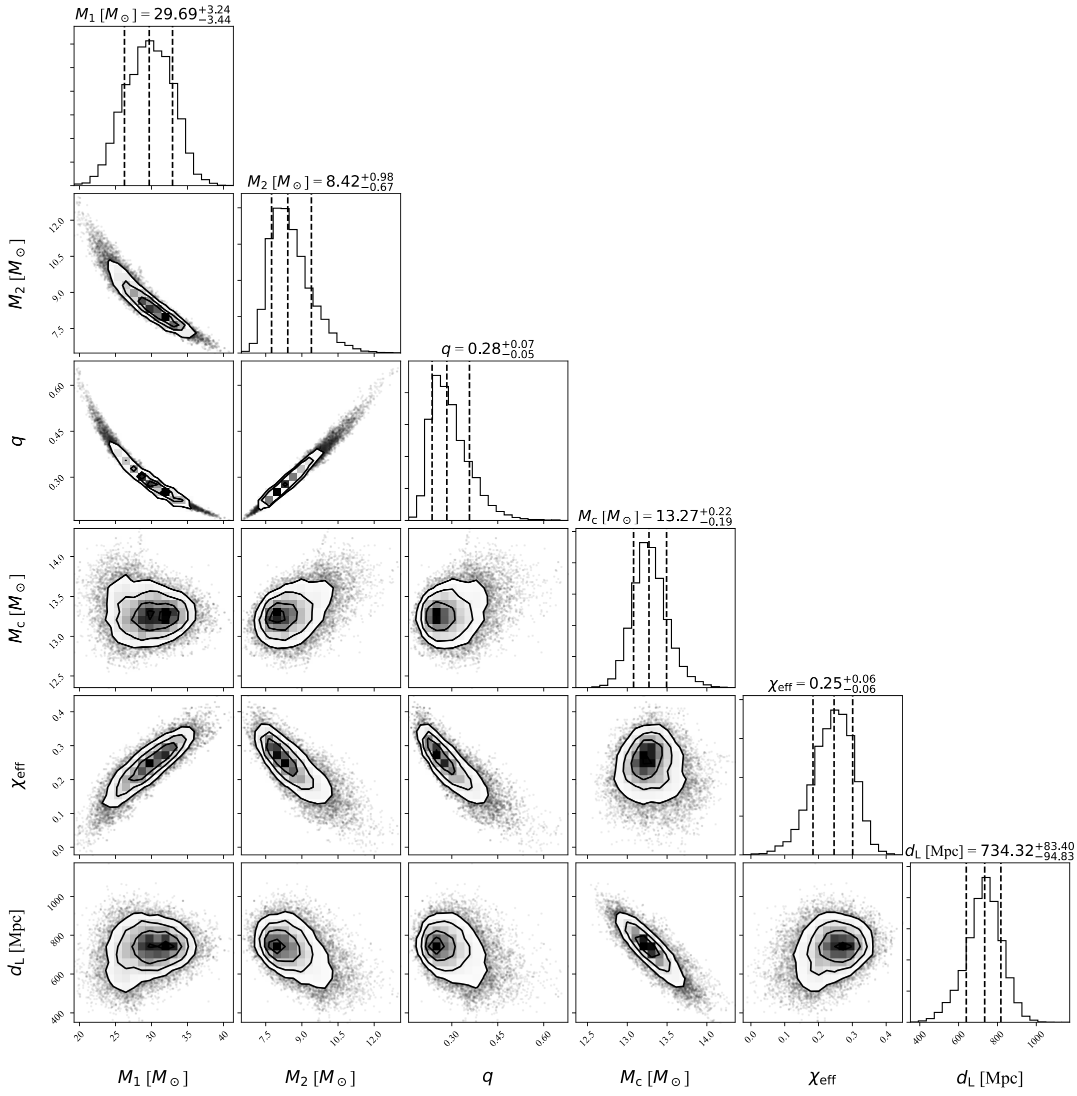

Fig. 2.3 Parameter estimation results for the BHBH merger GW190412. Indicated errors are 1-σ intervals.

CHAPTER 3

Ejecta from NSNS/BHNS mergers

In this chapter I present the different ejecta production mechanisms and the properties of each ejecta component from NSNS and BHNS mergers (§ 3.1-3.3). In § 3.4 I present the adopted fitting formulae and approximations to compute the ejecta properties.

3.1 Merger remnant and ejecta production

Ejecta from NSNS and BHNS mergers can be divided in two categories (see i.e. Fernández and Metzger 2016, Metzger 2019, Shibata and Hotokezaka 2019). Some NS material is released on the dynamical timescale ($\sim$ ms) due to partial NS disruption (induced by tidal forces) or to shock-heating (when the NS surfaces collide). A fraction of this material is gravitationally unbound and immediately leaves the merger region. This represents the "dynamical" ejecta. The remaining gravitationally bound material (that does not immediately fall on the central remnant object) can have enough angular momentum to form an accretion disc around the remnant. On a longer timescale (up to s) two outflows can arise from the accretion disc. Neutrino-matter interactions and magnetic processes produce the "wind" ejecta, while the disc spreading due to viscous processes and the following nuclear recombination produce the "secular" ejecta (Perego et al. 2017).

In BHNS mergers the simplified condition for ejecta production is that the distance $d_{\rm tid}$ at which tidal disruption takes place must be larger than the BH innermost stable circular orbit (ISCO) $R_{\rm ISCO}$. Indeed, if $d_{\rm tid} < R_{\rm ISCO}$ any released material is fated to fall in the BH. As explained in Foucart (2012), $R_{\rm ISCO} \propto M_{\rm BH}$ (for a given BH spin $\chi_{\rm BH}$) and $d_{\rm tid} \propto R_{\rm NS}(M_{\rm BH}/M_{\rm NS})^{1/3}$. Therefore the NS is significantly tidally disrupted if the BH is low-massive and/or rapidly spinning. Otherwise the NS directly plunges into the BH and no ejecta is produced (and, consequently, the event has no EM counterpart).

In NSNS mergers, the ejecta properties are strongly dependent on the fate of the central remnant, which is in turn determined primarily by the total binary mass $M_{\rm tot}$ (Shibata and Uryū 2000, Shibata and Taniguchi 2006). If $M_{\rm tot}$ is larger than a threshold value $M_{\rm thr}$ the merger results in a prompt BH formation (collapse time $t_{\rm coll} \lesssim 1$ ms). The value $M_{\rm thr}$ depends on the NS compactness $C_{\rm NS}$ and the maximum mass for non-rotating NSs $M_{\rm NS}^{\rm max}$ (Bauswein et al. 2013)[1]. If instead $M_{\rm tot} < M_{\rm thr}$ the merger produces a rapidly-spinning remnant NS, that can be indefinitely stable or temporarily stable before collapsing to a BH. The remnant mass is roughly

$$M_{\rm rem} = M_{\rm tot} - M_{\rm GW} - M_{\rm ej} - M_{\nu}, \tag{3.1}$$

where $M_{\rm GW}$ and M_{ν} are the mass lost through GW and neutrino emission, respectively, while $M_{\rm ej}$ is the ejecta mass. For rapidly-spinning NSs (close to break-up velocity) the maximum mass is larger than the value for non-rotating stars, tipically $M_{\rm NS,rot}^{\rm max} \sim 1.2 M_{\rm NS,non-rot}^{\rm max}$ (Baumgarte et al. 2000, Kaplan et al. 2014). If $M_{\rm tot}$ is close to $M_{\rm thr}$ the remnant is a "hypermassive" NS (HMNS), a star that is supported only by differential rotation and collapses to a BH once it has been removed (through GW emission and internal hydromagnetic torques), typically after $t_{\rm coll}$ ~tens-hundreds of ms (Shibata and Taniguchi 2006, Siegel et al. 2013). If the remnant is less massive it is a "supramassive" NS (SMNS), a star that can be supported also by solid rotation and collapses to a BH after a significant angular momentum loss (through less efficient processes, such as GW emission from small asymmetries and/or magnetic dipole radiation), with $t_{\rm coll} \gg$ hundreds of ms. Finally, if $M_{\rm tot}$ is very small, $M_{\rm rem} < M_{\rm NS}^{\rm max}$ and thus the remnant is an indefinitely stable NS (Metzger et al. 2008, Giacomazzo and Perna 2013) that will never collapse to a BH.

As an example, in Fig. 3.1 I show the relative probability for each remnant scenario for a population of NSNS binary mergers. I consider the NS mass distribution given in Kiziltan et al. (2013), namely a gaussian with $\mu = 1.32\ M_{\odot}$ and $\sigma = 0.11\ M_{\odot}$. I assume two EoS, namely "DD2" (Hempel and Schaffner-Bielich 2010, Typel et al. 2010) and "APR4" (Akmal et al. 1998, Read et al. 2009). They are, respectively, one of the stiffest and one of the softest among the EoS consistent with the constraints from both NICER results (Miller et al. 2019a, Riley et al. 2019) and GW170817/GW190425 signals (LVC 2019*e*, Kiuchi et al. 2019, Radice et al. 2018b, LVC 2020*c*). Fig. 3.1 is inspired by Fig. 4 of Margalit and Metzger (2019), however I calculate the merger remnant's mass differently. Indeed, starting from the same NS mass distribution, for each EoS I compute $M_{\rm rem}$ as explained in Eq. 5.1 (§ 5), thus neglecting the mass loss through neutrino emission. If $M_{\rm rem} < M_{\rm NS}^{\rm max}$ I classify the remnant as a stable NS. If $M_{\rm NS}^{\rm max} < M_{\rm rem} < \xi M_{\rm NS}^{\rm max}$, with $\xi = 1.18$, I classify the remnant as a SMNS (following Margalit and Metzger 2019, and references therein). If the total binary mass $M_{\rm tot}$ is larger than the threshold value $M_{\rm thr}$ for prompt collapse to a BH (Bauswein et al. 2013), I classify the remnant as a "prompt BH". Otherwise I classify the remnant as a HMNS. For the assumed NS mass distribution, for DD2 EoS $\sim 60\%$ of mergers end with a

---

[1] Bauswein et al. (2013) found that $M_{\rm thr}$ does not depend on the mass ratio $q = M_2/M_1$, for $q \gtrsim 0.7$. However Kiuchi et al. (2019) found that for asymmetric mergers the "prompt collapse" can happen on a timescale $t_{\rm coll}$ ~few ms, larger than the dynamical timescale of $\lesssim$1 ms.

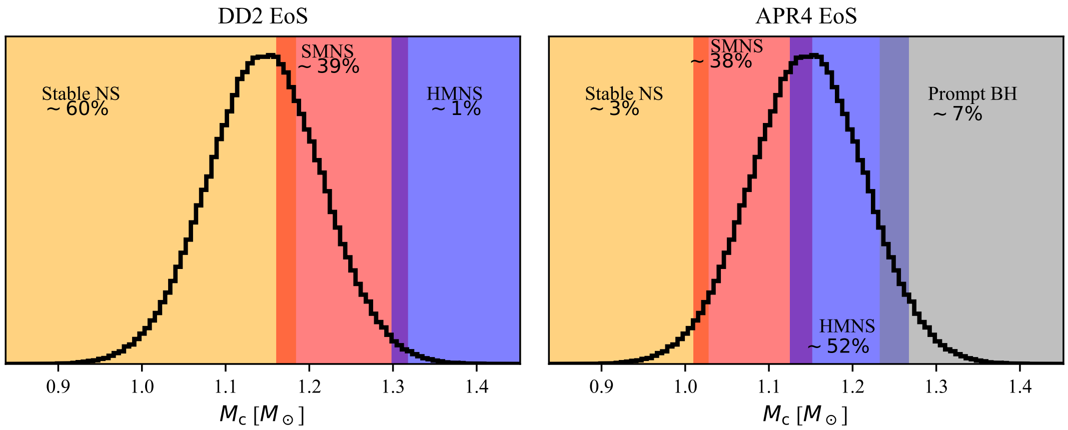

Fig. 3.1 Relative probability for each remnant scenario for a population of NSNS binary mergers. The black line indicates the chirp mass distribution (assuming the NS mass distribution given in Kiziltan et al. 2013). Left (right) panel shows the results for DD2 (APR4) EoS. Systems with chirp mass in the orange, red and blue region produce, respectively, a stable NS remnant, a SMNS and a HMNS. Systems in the gray region promptly collapse to a BH. This figure is inspired by Fig. 4 of Margalit and Metzger (2019), however here the merger remnant's mass is computed differently (see text for description).

stable NS, $\sim 39\%$ with a SMNS and $\sim 1\%$ with a HMNS. For APR4 EoS instead a stable NS forms only in $\sim 3\%$ of mergers, a SMNS in $\sim 38\%$, a HMNS in $\sim 52\%$, while a BH promptly forms in $\sim 7\%$ of mergers. This is consistent with expectations. Indeed stiff EoS (as DD2) support large $M_{\rm NS}^{\rm max}$ and produce massive ejecta (large NS deformabilities), while the contrary holds for soft EoS (as APR4).

3.2 Dynamical ejecta

In NSNS mergers dynamical ejecta are produced through two main processes. First, in the last phase of inspiral, tidal forces induce partial NS disruption, forming spiral arms that expand outwards (close to the equatorial plane) as a consequence of angular momentum transport (due to hydrodynamic processes). Then, when the NSs collide, surface material in the contact region is shocked and the quasi-radial remnant's pulsation pushes it outwards almost isotropically (see i.e. Hotokezaka et al. 2013). NSNS merger simulations found dynamical ejecta masses and velocities in the range, respectively, $\sim 10^{-4} - 10^{-2}\,\mathrm{M}_\odot$ and $0.1 - 0.3c$ (Hotokezaka et al. 2013, Radice et al. 2016, Bovard et al. 2017). The NSNS dynamical ejecta mass mainly depend on the total mass $M_{\rm tot}$, the mass ratio q and the NS EoS. I.e. for systems with $M_{\rm tot} > M_{\rm thr}$ that promptly form a BH the shock-driven ejection is suppressed; asymmetric mergers ($q \ll 1$) produce more massive ejecta (Bauswein et al. 2013, Bernuzzi et al. 2020); for soft EoS the NSs are less deformable, thus tidal disruption is less significant, producing less massive dynamical ejecta. Moreover, rapidly spinning NS produce more massive dynamical ejecta (Dietrich et al. 2017, Most et al. 2019). The opacity of NSNS dynamical ejecta depends on the remnant fate. Indeed if a SMNS/HMNS phase exists before the collapse to a BH, the strong neutrino irradiation can increase Y_e/lower κ (at least in the region close to the polar axis, where the neutrino wind is more intense), otherwise the opacity is large (very neutron-rich material).

In BHNS mergers dynamical ejecta are produced only by tidal disruption of the NS, as the BH has no crust (thus no shock happens when the two objects "collide"). Therefore these systems produce dynamical ejecta close to the equatorial plane and mainly in $\sim$half of the azimuthal angle (Kawaguchi et al. 2015, 2016, Fernández et al. 2017, Foucart et al. 2018). BHNS merger simulations found dynamical ejecta masses up to $\sim 0.1\,\mathrm{M}_\odot$ with velocities similar to the NSNS case. The BHNS dynamical ejecta mass mainly depends on χ_{BH}, $Q = M_1/M_2$ and NS EoS. I.e. low mass/rapidly spinning BHs have smaller R_{ISCO}, favoring the condition $d_{\mathrm{tid}} > R_{\mathrm{ISCO}}$ and producing massive dynamical ejecta; tidal disruption is favored for low Q, enhancing the dynamical ejecta mass (unless for large NS masses, corresponding to low deformabilities); for stiff EoS NSs are more deformable thus the dynamical ejecta are more massive. Due to the lack of an intermediate/stable NS remnant producing strong neutrino irradiation, the BHNS dynamical ejecta have large opacity (low Y_e).

3.3 Disk ejecta

BHNS mergers where NS tidal disruption takes place outside the R_{ISCO} and the majority of NSNS mergers lead to the formation of an accretion disc around the remnant object. NSNS/BHNS merger simulations found disc masses in the range $\sim 10^{-3} - 0.3\,\mathrm{M}_\odot$ (see i.e. Radice et al. 2018a, Kiuchi et al. 2019, Kyutoku et al. 2015, Kawaguchi et al. 2015, Foucart et al. 2019). In NSNS mergers the disc mass mainly depends on M_{tot}, q and the EoS. The production of massive discs involves the redistribution of angular momentum and mass of the remnant in the transition from differential to solid rotation. This can not happen in systems with large M_{tot} that promptly collapse to a BH and thus produce very low mass discs (or do not produce any disc). Kiuchi et al. (2019) found that asymmetric mergers $q < 1$ produce more massive accretion discs. For the same reason explained above, stiff EoS favor large disc masses. In BHNS mergers the disc mass mainly depends on χ_{BH}, Q and the NS EoS (same arguments as for dynamical ejecta).

The outflows from the accretion disc, namely the wind and secular ejecta, depending on the binary properties can be negligible or significant with respect to dynamical ejecta, affecting the kilonova emission.

3.3.1 Wind ejecta

After the disc formation, at early times the mass accretion rate on the central remnant is large and the disc produces thermal neutrinos (Popham et al. 1999). Neutrino heating produces mass outflow from the disc's surface, the wind ejecta. Another mechanism responsible of wind ejecta production could be the formation of spiral density waves in the disc, caused by oscillations of the NS remnant (Nedora et al. 2019). For NSNS mergers, in case of a prompt BH formation only a small fraction ξ_{w} of the disc's mass flows in the wind ejecta ($\xi_{\mathrm{w}} \sim 1\%$, see Fernández and Metzger 2013, Just et al. 2015), otherwise $\xi_{\mathrm{w}} \sim 5\%$[2] (Perego et al. 2017). In the case of a NS/SMNS/HMNS remnant, the strong neutrino irradiation increase the material's Y_e, producing wind ejecta with very low opacity κ. However Miller et al. (2019), performing Monte Carlo simulations with radiation transport, found that also in the case of prompt collapse to a BH the early disc evolution can produce wind ejecta with large Y_e. For BHNS mergers ξ_{w} is always $\sim 1\%$ (due to the lack of strong neutrino winds). However, by extending the Miller et al. (2019) results, also for BHNS mergers the wind ejecta can be assumed to have small κ.

3.3.2 Secular ejecta

Spiral density waves and/or magnetohydrodynamic turbulences produced by magneto-rotational instabilities transport angular momentum outwards. Over time ($\sim s$) the accretion rate on the central remnant decreases and the disc changes its state from neutrino-cooled to radiatively inefficient. This happens because the temperature decreases and consequently also the neutrino cooling rate (see Metzger 2019, and references therein). In the radiatively inefficient state, nuclear recombination and viscous turbulent heating are not balanced by neutrino cooling (Kohri et al. 2005). This produces additional mass outflows, the secular ejecta. This material, being in the center of the disk, had previously avoided neutrino irradiation and at the moment of its ejection the neutrino luminosity is very low. Therefore secular ejecta maintain a low Y_e. Accretion disc evolution simulations for NSNS mergers producing prompt BH formation and BHNS mergers showed that in secular ejecta all the r-process elements can be produced, having $Y_e \sim 0.2 - 0.4$ (Fernández and Metzger 2013, Just et al. 2015). Results from several 2-D and 3-D simulations indicate that a fraction $\xi_{\mathrm{s}} \sim 20\%$[3] of the accretion disc mass flows into secular ejecta (Just et al. 2015, Fernández et al. 2015, Kiuchi et al. 2015, Siegel and Metzger 2017, Fernández et al. 2019). Instead in NSNS

---

[2] Moreover a HMNS/SMNS can contribute to wind ejecta by expelling some of its own material due to the large neutrino luminosity ($\sim 10^{-3}\,\mathrm{M}_{\odot}$, see Perego et al. 2014, Martin et al. 2015) and/or during angular momentum redistribution in the case of differential rotation (Fujibayashi et al. 2018, Radice et al. 2018c).

[3] ξ_{s} values range from $\sim 30 - 40\%$ for rapidly spinning BH to $\sim 5\%$ for non-spinning BH (Just et al. 2015, Fernández et al. 2015, Siegel and Metzger 2017).

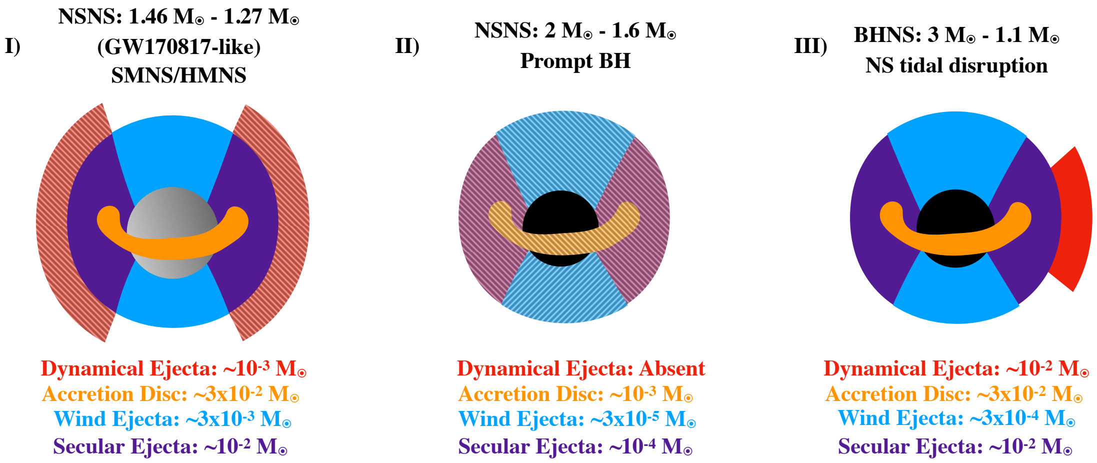

Fig. 3.2 Simple sketch representing the outcome of NSNS/BHNS mergers. Case I is a NSNS merger producing an intermediate SMNS/HMNS remnant, case II is a NSNS merger promptly forming a BH, case III is a BHNS merger where the NS is partially tidally disrupted. Solid-colored ejecta are relatively massive, while hatched-colored ones are relatively low-massive. Blue color indicates low opacity $\kappa \sim 0.5 - 1$ cm^2 g^{-1}, purple indicates intermediate opacity $\sim 1 - 5$ cm^2 g^{-1}, while red indicates large opacity $\gtrsim 10$ cm^2 g^{-1}.

mergers whose remnant is a SMNS/HMNS up to 90% of the disc mass can flow in disc ejecta, due to the more intense neutrino irradiation and the presence of a surface on the remnant (Metzger and Fernández 2014, Fahlman and Fernández 2018). In such cases the strong neutrino irradiation also increases Y_e in the disc ejecta. Indeed Fig. 6 in Metzger (2019) shows that for longer $t_{\rm coll}$ a larger disc ejecta Y_e is produced. In particular, for SMNS remnant ($t_{\rm coll} \gtrsim 300$ ms) the majority of ejecta has $Y_e \gtrsim 0.3$ (lanthanide-free, see Metzger and Fernández 2014, Kasen et al. 2015, Lippuner et al. 2017). Due to the large values of $\xi_{\rm s}$, the secular ejecta can be more massive than the dynamical ones. Indeed estimates of total ejecta mass from GW170817 are much larger than the typical dynamical ejecta mass found in simulations. This indicates that the majority of ejecta come from the disc outflows (see i.e. Siegel and Metzger 2017).

Table 3.1 summarises the ejecta parameters, with their description and typical values for NSNS/BHNS mergers.

In Fig. 3.2 I show a simple sketch representing the outcome of NSNS/BHNS mergers. Solid-colored ejecta are relatively massive, while hatched-colored ones are relatively low-massive. Blue color indicates low opacity $\kappa \sim 0.5 - 1$ cm^2 g^{-1}, purple indicates intermediate opacity $\sim 1 - 5$ cm^2 g^{-1}, while red indicates large opacity $\gtrsim 10$ cm^2 g^{-1}. Case I is a NSNS merger with component masses similar to the GW170817 event. The merger results in the formation of a SMNS/HMNS intermediate phase. Dynamical ejecta have low mass, while massive disc and wind/secular ejecta are produced. Case II is a NSNS merger promptly forming a BH. Dynamical ejecta are not produced, while accretion disc and wind/secular ejecta are low-massive. Finally case III is a BHNS

Parameter	Description	NSNS	BHNS
$m_{\rm dyn}$	Dynamical ejecta mass	$10^{-4} - 10^{-2}\ M_\odot$	$0 - 0.1\ M_\odot$
$\rm v_{dyn}$	Dynamical ejecta velocity	$0.1 - 0.3$ c	$0.1 - 0.3$ c
$\kappa_{\rm dyn}$	Dynamical ejecta opacity	$\sim 1 - 30$ cm^{2}g^{-1}	$\sim 15 - 30$ cm^{2}g^{-1}
$\theta_{\rm dyn}$	Dynamical ejecta latitudinal opening angle (measured from the equatorial plane)	$80 - 90$ deg	$10 - 20$ deg
$\phi_{\rm dyn}$	Dynamical ejecta azimuthal opening angle	2π rad	$\sim \pi$ rad
$m_{\rm disc}$	Accretion disc mass	$10^{-3} - 0.3\ M_\odot$	$0 - 0.3\ M_\odot$
$\xi_{\rm w}$	Disc mass fraction flowing in wind ejecta	$1 - 10\%$	$\sim 1\%$
$\rm v_w$	Wind ejecta velocity	$\sim 0.05 - 0.1$ c	~ 0.1 c
$\kappa_{\rm w}$	Wind ejecta opacity	$\sim 0.1 - 1$ cm^{2}g^{-1}	~ 1 cm^{2}g^{-1}
$\theta_{\rm w}$	Wind ejecta opening angle (measured from the polar axis)	~ 60 deg	~ 60 deg
$\xi_{\rm s}$	Disc mass fraction flowing in secular ejecta	$\sim 20 - 90\%$	$\sim 4 - 40\%$
$\rm v_s$	Secular ejecta velocity	$\sim 0.01 - 0.05$ c	~ 0.1 c
$\kappa_{\rm s}$	Secular ejecta opacity	$\sim 1 - 5$ cm^{2}g^{-1}	$\sim 5 - 10$ cm^{2}g^{-1}

Table 3.1 Ejecta properties for NSNS and BHNS mergers.

merger where the NS is partially tidally disrupted before plunging in the BH. Massive ejecta are produced. In all cases wind ejecta are confined in $\theta_{\mathrm{w}} \sim 60$ deg from the polar axis. Dynamical ejecta are almost isotropically produced in NSNS mergers, while in BHNS mergers they lie close to the equatorial plane ($\theta_{\mathrm{dyn}} \sim 20$ deg) spanning over $\sim$ half of the azimuthal angle ($\phi_{\mathrm{dyn}} \sim \pi$ rad).

3.4 Adopted fitting formulae for ejecta properties

In order to calculate the dynamical ejecta mass and velocity and the accretion disc mass I adopt fitting formulae calibrated on results from numerical simulations of NSNS/BHNS mergers.

Radice et al. (2018a) found that the dynamical ejecta mass from NSNS mergers is given by

$$\frac{m_{\mathrm{dyn}}}{10^{-3} M_{\odot}} = \left[\alpha \left(\frac{M_1}{M_2} \right)^{1/3} \left(\frac{1-2C_2}{C_2} \right) + \beta \left(\frac{M_2}{M_1} \right)^{n} + \gamma \left(1 - \frac{M_2}{M_2^*} \right) \right] M_2^* + (1 \leftrightarrow 2) + \delta, \tag{3.2}$$

where $\alpha = -0.657$, $\beta = 4.254$, $\gamma = -32.61$, $\delta = 5.205$, $n = -0.773$, M^* is the NS baryonic mass and $C = GM/(Rc^2)$ is the NS compactness, with R the star's radius. The symbol $(1 \leftrightarrow 2)$ means repeating the previous expression exchanging indices 1 and 2.

Radice et al. (2018a) found that the dynamical ejecta velocity from NSNS mergers is given by

$$\mathrm{v}_{\mathrm{dyn}} = \left[\alpha \left(\frac{M_2}{M_1} \right) (1 + \gamma C_2) \right] + (1 \leftrightarrow 2) + \beta, \tag{3.3}$$

where $\alpha = -0.287$, $\beta = 0.494$ and $\gamma = -3$.

In Barbieri et al. (2020b) a new fitting formula for the accretion disc mass from NSNS mergers was presented:

$$m_{\mathrm{disc}} = \frac{1}{4}(2 + x_1)(x_1 - 1)^2 M_2 + (1 \leftrightarrow 2), \tag{3.4}$$

where

$$x_1 \sim 2 \left[\left(1 + \frac{M_2}{M_1} \right)^{-1} + \lambda_1^{-1} - 1 \right] \tag{3.5}$$

and

$$\lambda_1 = \left(\frac{\tilde{\Lambda}}{\Lambda_0} \right)^{\alpha} \left(\frac{M_2}{M_1} \right)^{\beta}, \tag{3.6}$$

with $\Lambda_0 = 245$, $\alpha = 0.097$ and $\beta = 0.241$. This formula is consistent with both symmetric and asymmetric mergers[4] (simulations from Radice et al. 2018a, Kiuchi et al.

---

[4] Kiuchi et al. (2019) found the fitting formula from Radice et al. (2018a) to underestimate the accre-

2019). As a final tuning, a floor disc mass of $m_{\rm disc,min} = 10^{-3}\,{\rm M_\odot}$ is assumed (as in Radice et al. 2018a).

For what concerns BHNS mergers, Kawaguchi et al. (2016) reported the fitting formulae for dynamical ejecta mass,

$$\frac{m_{\rm dyn}}{M^*_{\rm NS}} = \max\left\{a_1 Q^{n_1}(1-2C)C^{-1} - a_2 Q^{n_2}\tilde{r}_{\rm ISCO}(\chi_{\rm eff}) + a_3\left(1 - \frac{M_{\rm NS}}{M^*_{\rm NS}}\right) + a_4, 0\right\}, \tag{3.7}$$

where $Q = M_{\rm BH}/M_{\rm NS}$, $a_1 = 4.464 \times 10^{-2}$, $a_2 = 2.269 \times 10^{-3}$, $a_3 = 2.431$, $a_4 = -0.4159$, $n_1 = 0.2497$, $n_2 = 1.352$, $\chi_{\rm eff} = \chi_{\rm BH} \cos \iota_{\rm tilt}$, with $\iota_{\rm tilt}$ the angle between the binary angular momentum and the BH spin. $\tilde{r}_{\rm ISCO}$ is the BH dimensionless innermost stable circular orbit, given by (Kawaguchi et al. 2016)

$$\tilde{r}_{\rm ISCO}(\chi) = 3 + Z_2 - sign(\chi)\sqrt{(3 - Z_1)(3 + Z_1 + 2Z_2)}, \tag{3.8}$$

where

$$Z_1 = 1 + (1 - \chi^2)^{1/3}\{(1+\chi)^{1/3} + (1-\chi)^{1/3}\} \tag{3.9}$$

and

$$Z_2 = \sqrt{3\chi^2 + Z_1^2}. \tag{3.10}$$

Kawaguchi et al. (2016) also found that the velocity of dynamical ejecta from BHNS mergers is given by

$$\frac{{\rm v}_{\rm dyn}}{c} = (aQ + b), \tag{3.11}$$

where $a = 1.533 \times 10^{-2}$ and $b = 0.1907$. Foucart et al. (2018) found that the mass remaining outside the remnant BH in a BHNS merger is given by

$$\frac{m_{\rm out}}{M^*_{\rm NS}} = \left[\max\left(\alpha\frac{1-2C}{\eta^{1/3}} - \beta\tilde{r}_{\rm ISCO}\frac{C}{\eta} + \gamma, 0\right)\right]^{\delta}, \tag{3.12}$$

where $\eta = Q/(1+Q)^2$ is the symmetric mass ratio, $\alpha = 0.406$, $\beta = 0.139$, $\gamma = 0.255$ and $\delta = 1.761$.

For BHNS mergers the accretion disc mass can be computed as

$$M_{\rm disc} = \max(m_{\rm out} - m_{\rm dyn}, 0). \tag{3.13}$$

All the different BHNS merger simulations to date (with BHs in the mass range $4 - 10M_\odot$), found unbound ejecta never exceeding few percent of $M_{\rm NS}$. Foucart et al. (2019) performed BHNS merger simulations in the near-equal-mass regime ($M_{\rm BH} \sim 1.4M_\odot$), finding the largest unbound component to be $\sim 28\%$ of $m_{\rm out}$. I assume that

---

tion disc mass in asymmetric mergers.

the dynamical ejecta mass is limited to

$$m_{\rm dyn}^{\rm max} = f m_{\rm out}. \tag{3.14}$$

Numerical simulations of tidal disruption events (Rees 1988) for an unbound star caused by a massive BH found that $\sim 50\%$ of the star's material forms an accretion disc and the other $\sim 50\%$ is unbounded. Although in BHNS mergers the NS is bound to the BH and tidal disruption will proceed differently, the value $f = 0.5$ can be assumed as the maximum ratio between $m_{\rm dyn}$ and $m_{\rm out}$.

The above formulae depend on the NS baryonic mass

$$M_{\rm NS}^{*} = {\rm B.E.} + M_{\rm NS}, \tag{3.15}$$

where B.E. is the binding energy. Lattimer and Prakash (2001) expressed this quantity as a function of the NS compactness and mass, namely

$${\rm B.E.} = M_{\rm NS} \frac{0.6C}{1 - 0.5C}. \tag{3.16}$$

Therefore $M_{\rm NS}^{*}$ is given by

$$M_{\rm NS}^{*} = M_{\rm NS} \left(1 + \frac{0.6C}{1 - 0.5C}\right) \tag{3.17}$$

Moreover, as explained in Barbieri et al. (2019a), I compute the NS compactness C using the "C-Love" relation (Yagi and Yunes 2017), a "quasi-universal" (EoS-independent) relation between the NS dimensionless tidal deformability Λ and its compactness:

$$C = \sum_{k=0}^{k=2} a_k (\ln \Lambda)^k, \tag{3.18}$$

where $a_0 = 0.36$, $a_1 = -3.55 \times 10^{-2}$ and $a_2 = 7.05 \times 10^{-4}$.

CHAPTER 4

Kilonovae

In this chapter I present the physics of kilonova emission. In § 4.1 I briefly summarize the history and bases of kilonova models. In § 4.2 I present the adopted kilonova model for NSNS mergers and the developed model for BHNS mergers. In § 4.3 I show some example kilonova light curves.

4.1 History of kilonovae

4.1.1 The r-process in the Universe

The "rapid neutron-capture process", or r-process, is a mechanism to form heavy elements, namely the lanthanides and attanides (with $A > 140$, beyond iron), through neutrons capture by lighter seed nuclei. This process takes place in dense and neutron-rich environments, there the β-decay timescale is longer than the neutron capture one. The r-process form neutron rich nuclei that are unstable (far from the "valley of stability"). Burbidge et al. (1957), Cameron (1957) indicated the r-process as the synthesis mechanism of about half of the heavy elements (beyond iron) in the Universe. The astrophysical environments where r-process can take place remained unclear for decades. A key quantity for the possibility of r-process occurrence is the material "electron fraction":

$$Y_e = \frac{n_p}{n_n + n_p}, \tag{4.1}$$

where n_n and n_p are, respectively, the neutrons and protons densities. In ordinary stellar material $n_p > n_n$ ($Y_e \geq 0.5$). The occurrence of r-process requires an excess of neutron ($Y_e < 0.5$).

Neutrino-heated winds from the proto-NSs formed in core collapse supernovae (SNae) have long been considered as the most promising r-process sites (see i.e. Duncan et al. 1986, Takahashi et al. 1994), but more recent works disfavoured this hypothesis (see i.e. Arcones et al. 2007, Roberts et al. 2012). A possible exception could be hyper-energetic SNae (with very massive proto-NSs and ultra-strong ordered magnetic fields). Such energetic events represent only $\sim 1/1000$ of all core collapse SNae. In order to reproduce the Galactic abundances, each event should release $\gtrsim 10^{-2}\,\mathrm{M}_\odot$ of r-process material, that will subsequently mix with the outer SN ejecta, containing the ^{56}Ni that causes the SN optical luminosity. The mix of such large amount of r-process material in the outer ejecta would redden the SN light curve. This is inconsistent with observed hyper-energetic SNae (see Metzger 2019, and references therein).

The mergers of BHNS and NSNS systems were proposed as viable sites of r-process through the decompression of neutron-rich ejecta (Lattimer and Schramm 1974, 1976 for BHNS and Symbalisty and Schramm 1982 for NSNS). Freiburghaus et al. (1999), analysing a NSNS merger simulation, first showed that the ejecta produced abundance patterns consistent with the r-process in the solar system. In SNae some material from the proto-NS's surface is pushed away, forming the neutrino-driven wind. Close to the NS surface the electron fraction Y_e is low, but interaction of nucleons with neutrinos (i.e. $\nu_e + n \to p + e^-$) increases the Y_e. Instead in NSNS/BHNS mergers, due to different geometry and more dynamical nature of the systems, some of the ejecta do not soffer strong neutrino irradiation, preserving a low $Y_e \lesssim 0.2$. In order to match the Galactic r-process abundances, a production rate of heavy elements ($A > 140$) $\sim 2 \times 10^{-7}\,\mathrm{M}_\odot\,\mathrm{yr}^{-1}$ is required (Qian 2000). The corresponding mass yield per merger is roughly (Metzger et al. 2009, Vangioni et al. 2016)

$$M_{r-\mathrm{proc}} \sim 10^{-2}\,\mathrm{M}_\odot \left(\frac{\mathcal{R}_{\mathrm{NSNS}}}{10\mathrm{yr}^{-1}}\right), \tag{4.2}$$

where $\mathcal{R}_{\mathrm{NSNS}}$ is the NSNS detection rate by LVC (design sensitivity). In support of NSNS/BHNS mergers being the source of r-process, numerical simulations indicate $M_{r-\mathrm{proc}} \sim 10^{-3} - 10^{-1}\,\mathrm{M}_\odot$ and $M_{r-\mathrm{proc}} \sim 0.03 - 0.06\,\mathrm{M}_\odot$ is consistent with the observed kilonova associated with GW170817. Moreover several evidences (see Metzger 2019, and references therein) support rare–high yield events (such as NSNS/BHNS mergers) to produce r-process with respect to common–low yield events (such as core collapse SNae). Thus NSNS/BHNS mergers are the likely dominant sources of r-process in the Universe[1].

4.1.2 The “birth” of kilonovae

As explained above, r-process nucleosynthesis produces nuclei far from the “valley of stability”. They are thus unstable and radioactively decay. Li and Paczyński (1998) first indicated the radioactive NSNS/BHNS ejecta as viable source of thermal transient emission. Having the ejecta low mass and large velocity, they rapidly become transparent to

---

[1] However there are some arguments that requires alternative sources. I.e. SN kicks could move the NSNS/BHNS binary far from the galaxy core, preventing the pollution of r-process nuclei in the galaxy. Moreover recent works suggest that SNae could better explain the r-process elements abundances in low-metallicity environments with respect to NSNS/BHNS mergers. These arguments seem to support an alternative r-process source at low metallicity, that could be the collapsars (massive rotating stars), whose collapse also powers long GRBs.

their own radiation. Thus this transient emission peaks at very early time (~ 1 day) and it has a much faster decay with respect to SNae (whose peak is at $\sim$ weeks/months).

Metzger et al. (2010) first determined the luminosity scale of these transients, using radioactive heating rates derived from nuclear reaction network calculation of r-process nucleosynthesis. They called these transients "kilonovae"[2], as their peaks are $\sim$1000 times brighter than novae. Metzger et al. (2010) also first stressed the connection between the r-process sources and GWs, short GRBs and kilonovae from NSNS/BHNS mergers (that today is common thought).

Besides the radioactive heating rate $\dot{\epsilon}_{\rm nuc}$, another important property to characterise the kilonova emission is the ejecta opacity κ. This quantity affects the kilonova peak and the time at which ejecta become transparent to different wavelengths. Kasen et al. (2013) showed that the opacity of heavy r-process elements is larger than $\kappa_{\rm Fe}$, as lanthanides and actinides have complex atomic structure producing a dense "forest" of line transitions. In ejecta with $Y_e \lesssim 0.2$ the r-process nucleosynthesis can form heavy lanthanides and attinides nuclei ($A \gtrsim 195$), giving a large opacity. Instead in ejecta with intermediate-large electron fraction $0.25 \lesssim Y_e \lesssim 0.4$ the ratio of free neutrons to seed nuclei is smaller and only the lighter lanthanides can be produced ($A \lesssim 130$). Although the opacity strongly depends on wavelength and evolves with time, kilonova emission can be modeled assuming an effective constant "gray" (wavelength independent) opacity κ. Tanaka et al. (2019) found that for $Y_e \lesssim 0.2$ the opacity is $\kappa \sim 20 - 30$ cm^2 g^{-1}, for $0.25 \lesssim Y_e \lesssim 0.35$ is $\kappa \sim 3 - 5$ cm^2 g^{-1} and for $Y_e \sim 0.4$ is $\kappa \sim 1$ cm^2 g^{-1} (at $T = 5000 - 10000$ K, the typical ejecta temperature around the peak emission time)[3].

For very large κ the kilonova peaks later (~ 1 week), at larger wavelengths (near-infrared) and at a lower luminosity with respect to low κ ejecta case (peaking at $\sim$1 day in the optical/UV band) (Barnes and Kasen 2013). Therefore Metzger and Fernández (2014) defined the emission from lanthanide-rich (low Y_e) ejecta "red" kilonova and the emission from lanthanide-poor (large Y_e) ejecta "blue" kilonova. They also suggested that both emissions could be present in an observed kilonova light curve, being produced by ejecta components with different properties. This hypothesis was confirmed with the first (and, at the moment of writing, the only) observed kilonova associated with GW170817. Indeed the observed light curve is consistent with a "blue + red" emission, powered by different ejecta components (see i.e. Perego et al. 2017).

---

[2] In the literature these transients are sometimes called "macronova". This term was introduced by Kulkarni (2005), who assumed the radioactive heating rate coming from free neutrons or ^{56}Ni. This assumption was later discredited, as free neutrons are captured during r-process and ^{56}Ni is not produced in NSNS/BHNS ejecta.

[3] However there is still some uncertainty on the lanthanides/actinides opacity calculations, due to their complex atomic states (partially filled f valence shells). Indeed the corresponding line strengths have not been measured in experiments and theoretically these large Z atoms are still an open problem.

4.2 Kilonova model

4.2.1 NSNS

I calculate the NSNS kilonova emission following Perego et al. (2017) (based on Grossman et al. 2014, Martin et al. 2015). They present a semi-analytical model that is axisymmetric with respect to the direction of the binary's total angular momentum. They divide the polar plane in 30 equally spaced slices (in $\cos\theta$) and they assume homologous expansion in each slice (as a reference see Fig. 15 in Martin et al. 2015, although there the polar plane is divided in 4 slices equally spaced in θ). In each slice the thermal emission at the photosphere is computed as in Grossman et al. (2014), Martin et al. (2015).

Results from numerical simulations (i.e. Rosswog et al. 2013) and analytical arguments (Wollaeger et al. 2018) indicate that the mass distribution in velocity space is described by

$$\frac{dm}{dv} \propto \left(1-\left(\frac{v}{v_{\max}}\right)^2\right)^3 v^2, \tag{4.3}$$

where $v_{\max}$ is the maximum ejecta velocity. In the following I consider the velocity as Lagrangian coordinate and I define "shell" the ejecta part with the same velocity. The bolometric luminosity in the j-th angular slice at time t from the i-th ejecta component is given by:

$$L_{ij}^{\rm bol}(t, m_{ij}, Y_{\mathrm{e},ij}) = \dot{\epsilon}_{\rm nuc}(t, Y_{\mathrm{e},ij}) m_{\mathrm{rad},ij}(t, m_{ij}, Y_{\mathrm{e},ij}). \tag{4.4}$$

In the above equation i refers to dynamical, wind or secular ejecta and j to one of the 30 angular slices. m_{ij} and $Y_{\mathrm{e},ij}$ are the mass and electron fraction of the i-th ejecta in the j-th slice. $\dot{\epsilon}_{\rm nuc}$ is the nuclear heating rate for r-process products radioactive decay. $m_{\mathrm{rad},ij}$ is the radiating shell's mass, described below.

The quantity m_{ij} is calculated considering that dynamical and secular ejecta are more concentrated close to the equatorial plane. (Perego et al. 2017) indicated their mass distributions in the polar plane as $F(\theta) \propto \sin^2\theta$, where θ is the polar angle, measured from the polar axis (direction of the binary's total angular momentum). Instead the wind ejecta propagates along the polar axis, with a constant mass distribution inside its opening angle $\theta_{\rm w} = 60$ deg. Thus its angular mass distribution can be expressed as $F(\theta) = \mathrm{const.}$ for $\theta \leq 60$ deg. Therefore m_{ij} for dynamical and secular ejecta is given by

$$m_{ij} = \frac{m_{i,\rm tot}}{16}\left(\cos 3\theta_{j+1} - 9\cos\theta_{j+1} - \cos 3\theta_{j-1} + 9\cos\theta_{j-1}\right), \tag{4.5}$$

while for wind ejecta

$$m_{ij} = \frac{m_{i,\rm tot}}{2(1-\cos\theta_{\rm w})}(\cos\theta_{j-1} - \cos\theta_{j+1}) \qquad \text{for} \quad \theta < \theta_{\rm w}, \tag{4.6}$$

where θ_{j+1} and θ_{j-1} are, respectively, the upper and lower bound of the j-th angular slice.

For simplicity in the following I fix a single choice ij and I drop the indices, as the treatment is the same for the two ejecta components and in all the angular slices.

Korobkin et al. (2012) found a fitting formula for $\dot{\epsilon}_{\rm nuc}$, based on detailed nucleosynthesis calculations:

$$\dot{\epsilon}_{\rm nuc}(t) = \epsilon_0 \frac{\epsilon_{\rm th}}{0.5} \left[\frac{1}{2} - \frac{1}{\pi} \arctan \left(\frac{t - t_0}{\sigma} \right) \right], \tag{4.7}$$

where $\sigma = 0.11$ s, $t_0 = 1.3$ s and $\epsilon_{\rm th}$ is the thermalization efficiency (for which in this work is assumed a constant value $\epsilon_{\rm th} = 0.5$). Korobkin et al. (2012) estimated the parameter ϵ_0 to be $\sim 1.2 \times 10^{18}$ erg g^{-1} s^{-1}. However, as indicated by Perego et al. (2017), there are large uncertainties in the decay models and nuclear mass, thus ϵ_0 is usually assumed in the range $\sim 10^{18} \lesssim \epsilon_0 \lesssim 2 \times 10^{19}$ erg g^{-1} s^{-1} (Mendoza-Temis et al. 2015, Rosswog et al. 2017).

Perego et al. (2017) introduced an additional term, $\epsilon_{\rm Y_e}$, in $\dot{\epsilon}_{\rm nuc}$. This term depends on the ejecta electron fraction $Y_{\rm e}$ and takes into account that large $Y_{\rm e}$ (low opacity) ejecta have a short decay half-life ($\sim$ few hours), thus at early times their emission is "boosted":

$$\epsilon_{\rm Y_e}(t) = \begin{cases} 0.5 + 2.5 \left\{ 1 + e^{\left[4\left(\frac{t}{1\,{\rm d}} - 1\right)\right]} \right\}^{-1} & \text{if } Y_e \geq 0.25, \\ 1 & \text{otherwise.} \end{cases} \tag{4.8}$$

In Eq. 4.4 the term $m_{\rm rad}$ is the mass of the radiating shell, that is the region between the diffusion surface and the photosphere. The former is the shell where the optical depth $\tau = \kappa \bar{\rho} \Delta r = c/{\rm v}$ (κ is the ejecta opacity), while the latter is the shell where $\tau = 2/3$. Below the diffusion surface the density is too large and photons can not escape (the diffusion timescale is larger than the dynamical one), while above the photosphere the density is too low and photon thermalisation in inefficient. Assuming homologous expansion, the ejecta mass distribution is stationary in velocity space. The mass of ejecta with velocity larger than a given value v can be expressed as:

$$m_{>{\rm v}}({\rm v}) = m_{\rm ej} \left[1 + F \left(\frac{\rm v}{{\rm v}_{\rm max}} \right) \right], \tag{4.9}$$

where, for the assumed mass distribution (see Eq. 4.3), $F(x)$ is given by

$$F(x) = \frac{35}{16} x^9 - \frac{135}{16} x^7 + \frac{189}{16} x^5 - \frac{105}{16} x^3. \tag{4.10}$$

As explained above, diffusion is effective when the optical depth is smaller than c/v:

$$\tau = \kappa\bar{\rho}\Delta r = \frac{\kappa m_{>\mathrm{v}}}{4\pi(\mathrm{v}t)^2} \leq \frac{c}{\mathrm{v}}. \tag{4.11}$$

By inverting this relation, the shell with velocity v corresponds to the diffusion surface at the time

$$t_{\mathrm{diff}} = \sqrt{\frac{\kappa m_{>\mathrm{v}}}{4\pi \mathrm{v} c}}. \tag{4.12}$$

Following the same reasoning, the shell with velocity v corresponds to the photosphere at the time

$$t_{\mathrm{phot}} = \sqrt{\frac{3\kappa m_{>\mathrm{v}}}{8\pi \mathrm{v}^2}}. \tag{4.13}$$

By inverting Eqs. 4.12-4.13 the evolution in time of the diffusion surface and photosphere can be computed. Finally, at each time, the mass of the radiating shell is given by:

$$m_{\mathrm{rad}}(t) = m_{>\mathrm{v}_{\mathrm{diff}}(t)} - m_{>\mathrm{v}_{\mathrm{phot}}(t)}. \tag{4.14}$$

The kilonova emission is assumed to be described by a blackbody. When ejecta are launched their temperature T is larger than 10.000 K and during their expansion they cool down. Barnes and Kasen (2013) found that when T reaches the first ionisation temperature of lanthanides, T_{La}, ejecta opacity rapidly drops due to the lanthanides recombination. The photosphere recedes inwards, following the front of recombination, and its temperature remains constant ($T = T_{\mathrm{La}}$). Before recombination the photospheric radius is given by

$$R_{\mathrm{phot}} = \mathrm{v}_{\mathrm{phot}} t, \tag{4.15}$$

Instead after recombination, using Stefan-Boltzmann law:

$$L_{\mathrm{bol}} = A\sigma_{\mathrm{SB}}T^4 = R^2\Omega\sigma_{\mathrm{SB}}T^4, \tag{4.16}$$

and fixing the temperature to T_{La}, the photospheric radius is give by:

$$R_{\mathrm{phot}} = \sqrt{\frac{L_{\mathrm{bol}}}{\Omega\sigma_{\mathrm{SB}}T_{\mathrm{La}}^4}}, \tag{4.17}$$

where Ω is the subtended solid angle and σ_{SB} is the Stefan-Boltzmann constant. At each time R_{phot} is the minimum of Eq. 4.15 and 4.17. Summarizing:

$$\begin{cases} R_{\mathrm{phot}} = \mathrm{v}_{\mathrm{phot}} t,\ T = \left(\frac{L_{\mathrm{bol}}}{\Omega\sigma_{\mathrm{SB}}R_{\mathrm{phot}}^2}\right)^{1/4} & \text{before recombination,} \\ T = T_{\mathrm{La}},\ R_{\mathrm{phot}} = \sqrt{\frac{L_{\mathrm{bol}}}{\Omega\sigma_{\mathrm{SB}}T_{\mathrm{La}}^4}} & \text{after recombination,} \end{cases} \tag{4.18}$$

Martin et al. (2015) computed the observed spectral flux as a superposition of Planckian distributions. For each angular bin, they project the emitting surface along the observer's line of sight. The observed spectral flux at a given time t and frequency ν is

$$F_\nu(\mathbf{w}, \mathrm{t}) = \sum_j B_\nu(T_j(t)) \int_{\hat{\mathbf{n}}_\mathbf{j} \cdot \mathbf{w} > 0} \mathbf{w} \cdot d\mathbf{\Omega}, \tag{4.19}$$

where $B_\nu(T_j(t))$ is the blackbody spectrum in the j-th angular slice, $\mathbf{w}$ is the observer's direction, $\hat{\mathbf{n}}_\mathbf{j}$ is the unit vector orthogonal to the j-th angular slice's photosphere. The integral in Eq. 4.19, which represents the projection factors, is time independent. Thus it can be computed once and used as weighting factors $p_j(\mathbf{w})$, obtaining

$$F_\nu(\mathbf{w}, \mathrm{t}) = \sum_j p_j(\mathbf{w}) B_\nu(T_j(t)). \tag{4.20}$$

At each time B_ν is given by

$$B_\nu = \left(\frac{R_\mathrm{phot}}{d_\mathrm{L}}\right)^2 \frac{2h\nu^3}{c^2} \frac{1}{e^{h\nu/(k_\mathrm{B}T)} - 1}, \tag{4.21}$$

where h is the Planck constant, k_B the Boltzmann constant and d_L the luminosity distance.

4.2.2 BHNS

I model the wind and secular ejecta kilonova emission for BHNS mergers as in the NSNS case. As explained in §3.2 BHNS mergers produce dynamical ejecta with a "crescent-like" geometry, close to the equatorial plane, that is not axisymmetric with respect to the binary's total angular momentum direction (contrary to the other ejecta components). Kawaguchi et al. (2016), Fernández et al. (2017) found that dynamical ejecta from BHNS mergers extend in the latitudinal and azimuthal directions, respectively, over $\theta_\mathrm{dyn} \sim 0.2 - 0.5$ rad and $\phi_\mathrm{dyn} \sim \pi$. I calculate the BHNS dynamical ejecta kilonova emission as presented in (Barbieri et al. 2020a).

I assume that dynamical ejecta mass distribution in velocity space is the same as Eq. 4.9. Each shell in the dynamical ejecta can emit from the photosphere in the latitudinal or radial direction, depending on which diffusion time is the shortest. The diffusion approximation is the same as above. If θ is the angular distance from the equatorial plane, dynamical ejecta are found in the region from $-\theta_\mathrm{dyn}$ to θ_dyn. In the following I consider only half of this region ($\theta > 0$), as the other one can be treated in the same way (reversing the signs). Considering a photon produced at an angle θ, its latitudinal direction diffusion time is

$$t_\mathrm{d,lat} \sim \frac{(\theta_\mathrm{dyn} - \theta)^2 \kappa_\mathrm{dyn}\, dm/d\mathrm{v}}{c\, \theta_\mathrm{dyn} \phi_\mathrm{dyn}\, t}, \tag{4.22}$$

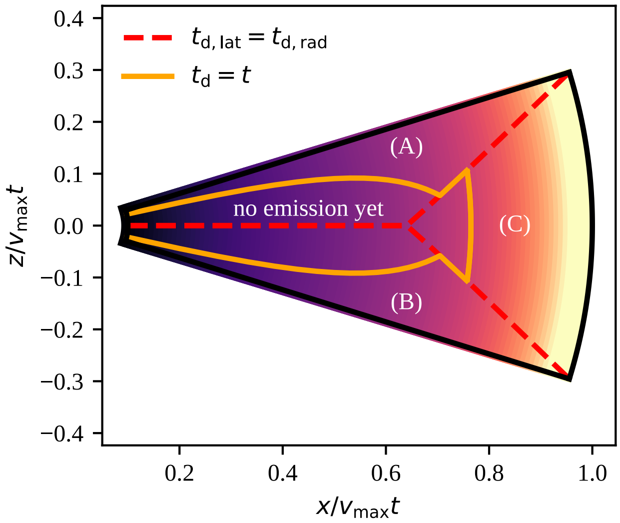

Fig. 4.1 Sketch of a section in the dynamical ejecta. The equatorial plane is at $z = 0$. Purple regions are denser than yellow ones (density decreases outwards). The orange solid line contains the ejecta region for which radiative diffusion has not reached the surface yet (thus emission is not possible yet). The red dashed line identifies three ejecta regions, according to the surface to which the diffusion time is the shortest. Region A emits from the upper latitudinal surface, region B from the lower latitudinal surface, region C from the radial surface. Image from Barbieri et al. (2019a), copyright by the authors.

with κ_{dyn} the dynamical ejecta opacity. Instead its radial direction diffusion time is

$$t_{\mathrm{d,rad}} \sim \frac{\kappa_{\mathrm{dyn}} m_{\mathrm{dyn},>\mathrm{v}}(\mathrm{v}_{\mathrm{max}} - \mathrm{v})}{c\,\theta_{\mathrm{dyn}}\phi_{\mathrm{dyn}}\mathrm{v}^2 t}. \tag{4.23}$$

By comparing the two times, the angle θ_{lat} above which photons diffuse in the latitudinal direction ($t_{\mathrm{d,lat}} < t_{\mathrm{d,rad}}$) is

$$\theta_{\mathrm{lat}}(\mathrm{v}) = \theta_{\mathrm{dyn}} - \min\left(\theta_{\mathrm{dyn}}, \sqrt{\frac{m_{\mathrm{dyn},>\mathrm{v}}(\mathrm{v}_{\mathrm{max}} - \mathrm{v})}{\mathrm{v}^2 dm/d\mathrm{v}}}\right). \tag{4.24}$$

Therefore three regions can be identified in the dynamical ejecta. Those with $\theta > \theta_{\mathrm{lat}}(\mathrm{v})$ and $\theta < -\theta_{\mathrm{lat}}(\mathrm{v})$ (A and B in Fig. 4.1) emit in the latitudinal direction (respectively above and below the equatorial plane), while the other one (C in Fig. 4.1) emit in the radial direction.

In region A the diffusion time $t_{\mathrm{d,lat}}$ equals the elapsed time at the angle

$$\theta_{\mathrm{d}}(\mathrm{v}, t) = \theta_{\mathrm{dyn}} - t\sqrt{\frac{c\,\theta_{\mathrm{dyn}}\phi_{\mathrm{dyn}}}{\kappa_{\mathrm{dyn}} dm/d\mathrm{v}}}. \tag{4.25}$$

Assuming that the energy released by nuclear heating above θ_{d} immediately contributes to the emission and that the density distribution in the latitudinal direction is uniform, the luminosity per unit velocity in the latitudinal direction is

$$\frac{dL_{\rm lat}}{d{\rm v}}({\rm v},t) = \frac{1}{2}\dot{\epsilon}(t)\frac{dm}{d{\rm v}} \times \max\left(1 - \frac{\theta_{\rm lat}({\rm v})}{\theta_{\rm dyn}}, 1 - \frac{\theta_{\rm d}({\rm v},t)}{\theta_{\rm dyn}}\right), \tag{4.26}$$

where the term $1/2$ indicates that only the region with $\theta > 0$ has been considered. The latitudinal surface for each shell is given by

$$\frac{dS_{\rm lat}}{d{\rm v}}({\rm v},t) = \phi_{\rm dyn}{\rm v}\, d{\rm v}\, t^2, \tag{4.27}$$

and its black-body effective temperature is

$$T_{\rm BB,lat}({\rm v},t) = \left(\frac{dL_{\rm lat}/d{\rm v}}{\sigma_{\rm SB}(dS_{\rm lat}/d{\rm v})}\right)^{1/4}. \tag{4.28}$$

Considering the occurrence of lanthanides recombination, the latitudinal surface effective temperature is given by

$$T_{\rm lat}({\rm v},t) = \max(T_{\rm BB,lat}({\rm v},t), T_{\rm La}). \tag{4.29}$$

For what concerns the radially-emitting region (C), the relative velocity between the emitting surface and the shell must be taken into account. Photons can escape from a region if their diffusion velocity is larger than the local expansion velocity. The value $\rm v_d$, above which photons can escape, can be estimated from the implicit equation

$$t = \sqrt{\frac{\kappa_{\rm dyn} m_{\rm dyn,>v_d}}{\theta_{\rm dyn}\phi_{\rm dyn}{\rm v_d} c}}. \tag{4.30}$$

The radial luminosity is thus given by

$$L_{\rm rad}(t) = \dot{\epsilon}(t)\; m_{\rm rad,>v_d}(t), \tag{4.31}$$

where $m_{\rm rad,>v}$ is the dynamical ejecta mass in region C with velocity larger than v, namely

$$m_{\rm rad,>v} = \int_{\rm v}^{\rm v_{phot}} \frac{\theta_{\rm lat}({\rm v})}{\theta_{\rm dyn}}\frac{dm}{d{\rm v}}d{\rm v}. \tag{4.32}$$

The upper extremum of this integral is $\rm v_{phot}$, because material beyond the photosphere does not contribute to emission (as explained above). The radial emission surface is

$$S_{\rm rad}(t) \sim \phi_{\rm dyn}\theta_{\rm dyn}{\rm v}_{\rm phot}^2 t^2\,, \tag{4.33}$$

where the photosphere's velocity $\mathrm{v}_{\rm phot}$ is calculated from the relation

$$\tau = \frac{2}{3} = \frac{\kappa_{\rm dyn} m_{>\mathrm{v}_{\rm phot}}}{\theta_{\rm dyn}\phi_{\rm dyn}\mathrm{v}^2_{\rm phot} t^2}\,. \tag{4.34}$$

The effective temperature of radial photosphere is

$$T_{\rm rad}(t) = \max\left[\left(\frac{L_{\rm rad}(t)}{\sigma_{\rm SB} S_{\rm rad}(t)}\right)^{1/4}, T_{\rm La}\right]. \tag{4.35}$$

Under the assumption that dynamical ejecta is geometrically thin, the projection factor of latitudinal emission in the observer's direction $\theta_{\rm v}$ (with respect to the polar axis) is

$$f_{\rm lat} = \cos(\theta_{\rm v}), \tag{4.36}$$

while the projection factor of radial emission is

$$f_{\rm rad} = \pi\cos(\theta_{\rm v})\sin^2(\theta_{\rm dyn}) + 2\sin(\theta_{\rm v})[\theta_{\rm dyn} + \sin(\theta_{\rm dyn})\cos(\theta_{\rm dyn})]. \tag{4.37}$$

4.3 Kilonova example light curves

In Fig. 4.2 I show some example of kilonova light curves, in the g-band (484 nm, left column) and J-band (1250 nm, right column). The first row distinctly shows the contributions to the total kilonova light curve (solid red) from the dynamical (dashed blue), wind (dot-dashed orange) and secular (dotted green) ejecta. This kilonova corresponds to a NSNS merger producing $m_{\rm dyn} \sim 2.5 \times 10^{-4} M_\odot$ and $m_{\rm disc} \sim 0.13 M_\odot$ (consequently $m_{\rm wind} \sim 5.6 \times 10^{-3} M_\odot$ and $m_{\rm sec} \sim 2.6 \times 10^{-2} M_\odot$), whose distance is $d_{\rm L} = 40$ Mpc. The behaviour of each ejecta component depends on its properties. In the other rows of Fig. 4.2 I show the kilonova emission dependence on the opacity κ, velocity v and mass m. The second row shows that emission from ejecta with large κ has slower evolution, dimmer peak and more contribution at larger wavelengths with respect to low κ ejecta. The third row shows that emission from ejecta with large v has a faster evolution and brighter peak with respect to low v ejecta. The fourth row shows that emission from massive ejecta has a slower evolution and brighter peak with respect to ejecta with low mass. For the considered case in the first row, the wind ejecta dominates the emission in the first ~ 3 days, after which the kilonova is dominated by the secular ejecta. The dynamical ejecta is faster than the other components ($v_{\rm dyn} \sim 0.18$c, $v_{\rm w} \sim 0.06$, $v_{\rm s} \sim 0.04$), thus it has an earlier peak but it is sub-dominant as it is very low-massive. Moreover the dynamical and secular ejecta, having large opacity κ, produce larger emission in the J-band (near-infrared), as also explained in §4.1.2.

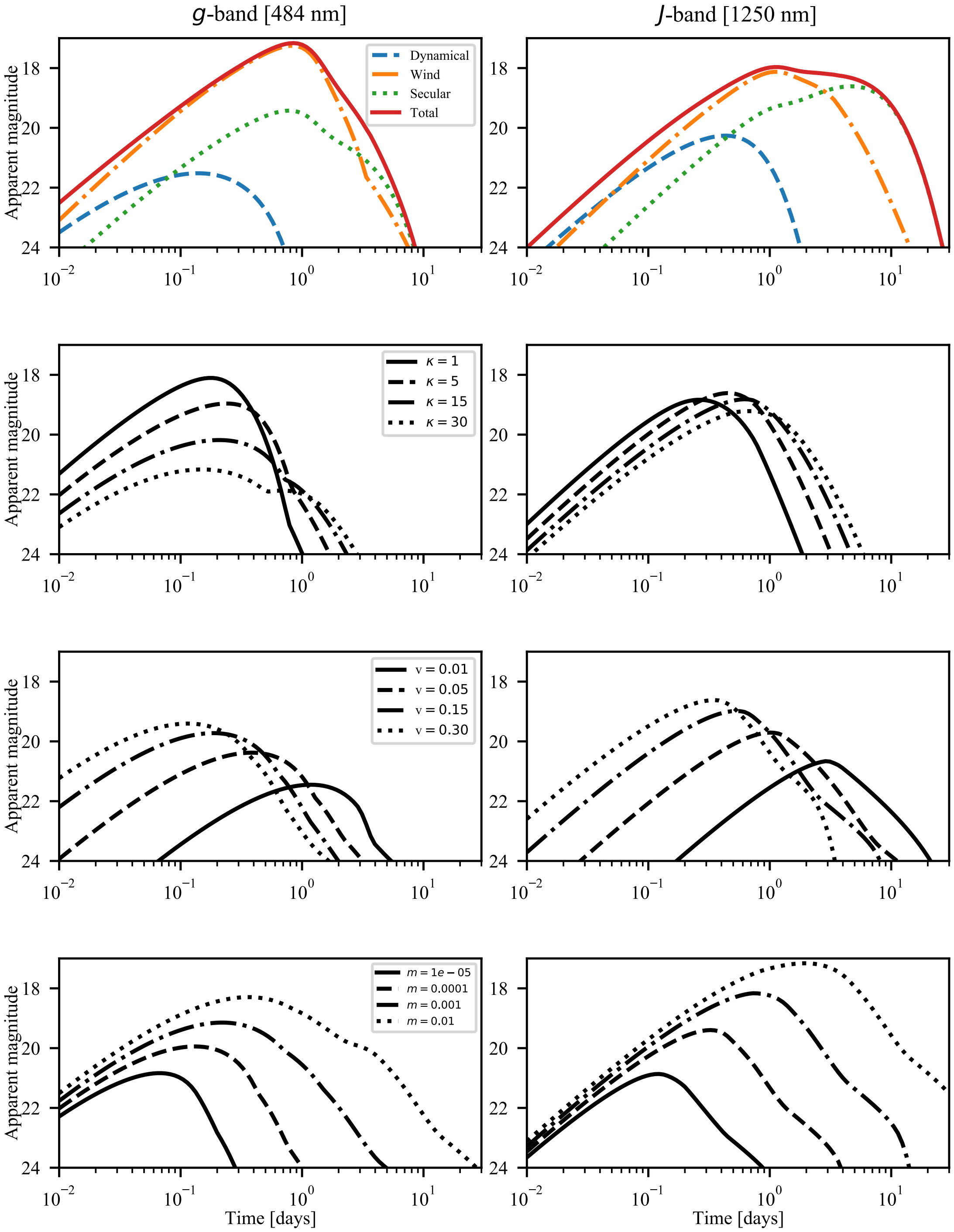

Fig. 4.2 Example kilonova light curves in the g- (left column) and J-band (right column). The first row shows the contributions to the total kilonova light curve (solid red) from the dynamical (dashed blue), wind (dot-dashed orange) and secular (dotted green) ejecta. The other rows show the kilonova emission dependence on the opacity κ (second row), velocity v (third row) and mass m (last row).

CHAPTER 5

Gamma-Ray Bursts

In this chapter I present the basic physics of GRBs. In §5.1 I briefly resume the GRB observation history. In §5.2 I introduce the mechanisms of GRB prompt and afterglow emission. In §5.3.1 I explain the necessary conditions for GRB jet launch. In §5.3.2 I show how to calculate the jet's energy. In §5.3.3 I describe the assumed jet's structure. In §5.4-5.5 I present the assumed GRB prompt and afterglow emission models.

5.1 A brief history

GRBs are intense and short pulses of gamma-rays. They are the most luminous known events in the Universe, with an isotropic luminosity of $\sim 10^{51-52}$ erg/s. Their duration varies from fractions up to hundreds of seconds. The gamma-ray emission is defined "prompt". It is followed by a longer lasting and lower energy emission in the X-ray, optical and radio bands, defined "afterglow".

The first GRB prompt emission was detected in 1967. In the early '90s the Burst And Transient Source Experiment (BATSE) instrument performed an all-sky survey, finding that GRBs are isotropically distributed, favoring a cosmological origin. Therefore, considering the large distances, the measured fluxes imply very large energy. Furthermore, considering the rapid time variability, this energy must be emitted in a short time in a small volume. Following these arguments, a relativistically expanding fireball was proposed as the emission mechanism of GRBs (see i.e. Paczynski 1986). The first GRB afterglow emission was detected in the late '90s by Beppo-SAX satellite, in the X-rays. The corresponding measured redshift distance confirmed that GRBs are cosmological sources (Metzger et al. 1997, Djorgovski et al. 1998). In the following years other afterglows were detected, also in optical and radio bands, over timescales of months (van Paradijs et al. 2000, see i.e.). The observations are consistent with the fireball model.

In 2004 the Swift satellite started its mission, leading to the multi-wavelength observation of several GRBs from $\sim$ minutes to $\sim$ hours after the burst trigger. This allowed a deeper understanding of the transition from prompt to afterglow emission, discovering i.e. several X-ray early behaviours.

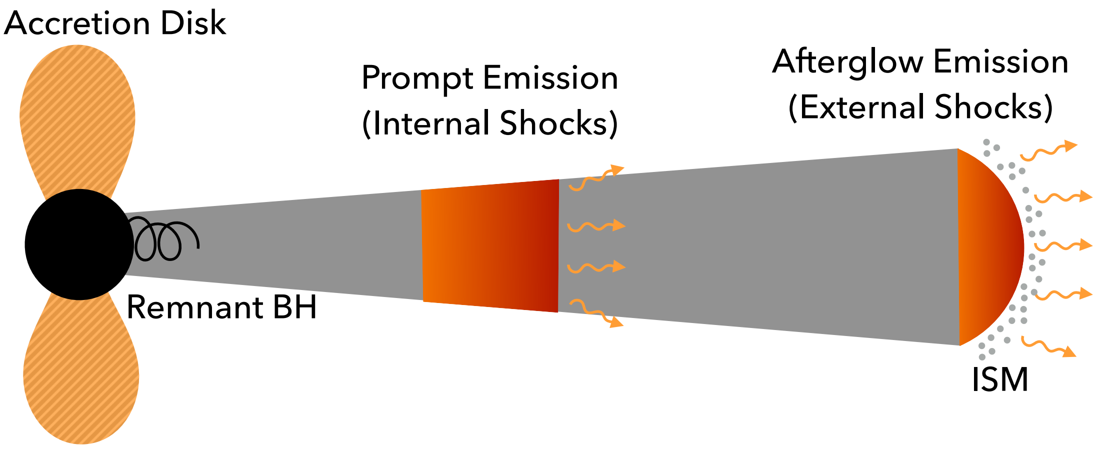

Fig. 5.1 Schematic representation of a GRB jet.

5.2 Basis of GRBs

Depending on the gamma-ray emission duration, GRBs can be divided in two categories: the short GRBs (sGRBs) emission lasts less than 2 seconds, while the long GRBs (LGRBs) have a longer lasting emission.

GRBs are generated by matter accretion from a disk on a compact object. In particular, LGRBs are produced after core collapse of very massive stars, while sGRBs production sites are NSNS and BHNS mergers (under some conditions, described in the following). The matter accretion on a compact object leads to the launch of a collimated relativistic outflow (jet). It can be thought as a series of shells propagating with different velocities. These shells can collide, producing the so-called “internal shocks” that convert a fraction of the jet’s kinetic energy in photons. Thus “internal shocks” are supposed to be the cause of GRB Prompt emission (although other processes, such as magnetic reconnection, have been proposed). After the Prompt emission the relativistic jet continues expanding in the ISM. Due to the interaction with the latter, the jet is decelerated, leading to the formation of a strong relativistic forward shock (“external shock”). Close to this shock, ISM electrons are accelerated trough Fermi process and produce synchrotron emission, powering the GRB afterglow emission. Fig. 5.1 is a schematic representation of a GRB jet.

However, before expanding in the ISM, the jet must propagate in the matter surrounding the region where it is created. In particular, for LGRBs the jet must overcome the dense stellar wind produced in the core collapse explosion, while for sGRBs it must overcome the ejecta produced during the merger. If the jet has a large enough kinetic energy to overcome the surrounding matter (“breakout”) it is defined a “successful jet” and it produces the above mentioned emissions. Otherwise the jet can not overcome the surrounding matter and its energy is transferred to the ambient (“choked jet”). In this case there is no GRB emission.

In the following I will consider only sGRBs, as they are produced in NSNS and BHNS mergers.

5.3 Relativistic jet

5.3.1 Jet launch and breakout condition

For what concerns BHNS mergers, the remnant is always a BH. Therefore a relativistic jet is launched if the NS is partially tidally disrupted before falling in the BH and an accretion disc is created. The jet is assumed to be launched perpendicularly to the binary orbital plane (polar direction). As explained in §4, very low ejecta mass is expected to be launched in the polar direction. Therefore jets from BHNS mergers will always be "successful".

For what concerns NSNS mergers, Ciolfi (2020) indicated that if the remnant is a long-lived massive NS the produced outflow is not consistent with a sGRB jet, as the baryon content is large and the maximum achievable Lorentz factor is too low. Therefore[1] the jet launch condition for these systems is the formation of a BH. One can thus impose that the merger remnant mass $M_{\rm rem}$ is larger than the maximum NS mass $M_{\rm NS}^{\rm max}$:

$$M_{\rm rem} = M_1 + M_2 - M_{\rm dyn} - M_{\rm disk} - M_{\rm GW} > M_{\rm NS}^{\rm max}, \tag{5.1}$$

where M_1 and M_2 are the component masses, $M_{\rm dyn}$ and $M_{\rm disk}$ are the dynamical ejecta and accretion disk masses, $M_{\rm GW} = E_{\rm GW}/c^2$ is the mass loss corresponding to energy emission in GWs. Zappa et al. (2018) proposed the following relation to calculate the energy emitted in GWs:

$$e_{\rm GW} \sim a j_{\rm rem}^2 + b j_{\rm rem} + c, \tag{5.2}$$

where $a = 0.005$, $b = -0.4$, $c = 0.9$, $e_{\rm GW} = E_{\rm GW}/(M_{\rm tot}\nu)$ and $j_{\rm rem} = J_{\rm rem}/(M_{\rm tot}^2\nu)$, with $M_{\rm tot}$ the total binary mass, ν the symmetric mass ratio and $J_{\rm rem}$ the remnant angular momentum. The latter quantity is related to the dimensionless spin parameter χ through the relation $\chi = cJ/GM^2$. Coughlin and Dietrich (2019) proposed a fitting formula to calculate $\chi_{\rm rem}$:

$$\chi_{\rm rem} = \tanh[a\nu^2(M_{\rm tot} + b\tilde{\Lambda}) + c], \tag{5.3}$$

where $\tilde{\Lambda}$ is the binary effective tidal deformability parameter. Fig. 5.2 shows the NSNS binary configurations producing a BH remnant (on the right of the purple line) or a

---

[1] I stress that this is not the only picture in the literature. Indeed i.e. Mösta et al. (2020) performed three-dimensional magnetohydrodynamic simulations, studying the effect of magnetic fields in post-merger remnant evolution. They found that HMNS can produce a jet with $\Gamma \sim 5$. However they argued that including radiative processes in the jet and neutrino pair-annihilation Γ could increase, showing that also HMNS could produce sGRBs. In this work I will follow the indication by Ciolfi (2020).

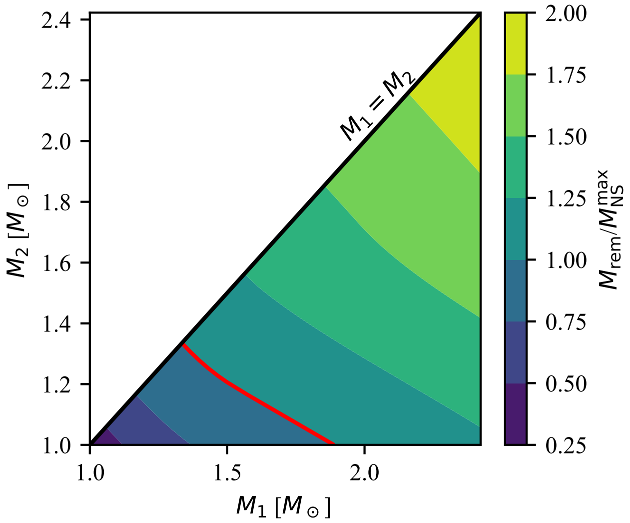

Fig. 5.2 Ratio of NSNS merger remnant mass and maximum NS mass, assuming DD2 EoS. The red line divides binary configurations producing a long-lived NS (on its left) from those whose remnant is a BH (on its right).

long-lived NS (on the left), assuming DD2 EoS.

Even if the remnant is a BH, the GRB emissions will be produced only if the jet overcomes the ejecta[2]. Therefore the jet's energy must be larger than the minimum energy for breakout ($E_{\rm bkt}$). Duffell et al. (2018) described this quantity as:

$$E_{\rm bkt} = 0.05 E_{\rm ej} \theta_{\rm j}^2, \tag{5.4}$$

where $\theta_{\rm j}$ is the initial jet opening angle and $E_{\rm ej}$ is the kinetic energy of the ejecta encountered by the jet. We calculate this quantity assuming the ejecta mass angular distribution presented in §4 and calculating the different component masses in the cone centered on the polar axis with opening angle $\theta_{\rm j}$. Fig. 5.3 shows the NSNS binary configurations producing a "successful jet", assuming DD2 EoS. Excluding the cases where a jet is not launched, due to the formation of a stable NS remnant (bottom-left light gray region), it is evident that the jet is always "successful". Indeed even for NSNS mergers the ejecta densities are not comparable to the large density of stellar winds, that can cause the "choking" of LGRBs.

5.3.2 Jet launch

In NSNS/BHNS mergers where NS tidal disruption produces a disk around the remnant BH, a relativistic jet can be launched during matter accretion through the Blandfor-

---

[2] In reality if the jet is "choked", all its energy is given to the ejecta. The energized ejecta could produce a dimmer "cocoon-like" emission (Mooley et al. 2018, Gottlieb et al. 2018, Salafia et al. 2019b). However in this work I consider only GRB emission from "successful" jets.

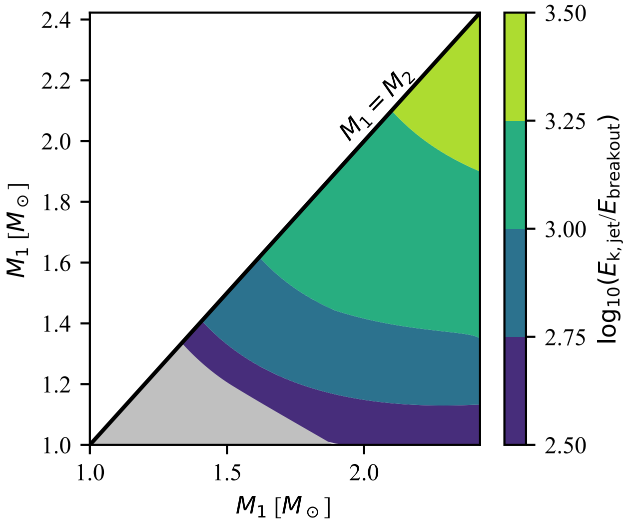

Fig. 5.3 Ratio of jet's kinetic energy and minimum required energy for breakout, assuming NSNS mergers with DD2 EoS. Light gray region (bottom left) indicates binary configurations that do not produce a jet due to a long-lived NS remnant.

Znajek mechanism (Blandford and McKee 1976, Komissarov 2001). Tchekhovskoy et al. (2010) expressed the luminosity of this process as:

$$L_{\mathrm{BZ}} \propto \frac{G^2}{c^3} M_{\mathrm{BH}}^2 B^2 \Omega_{\mathrm{H}}^2 f(\Omega_{\mathrm{H}}), \tag{5.5}$$

where B is the magnetic field's amplitude at the BH horizon, Ω is the dimensionless BH angular velocity at the horizon ($0 \leq \Omega_{\mathrm{H}} \leq 1/2$),

$$\Omega_{\mathrm{H}} = \frac{\chi_{\mathrm{BH}}}{2(1 + \sqrt{1 - \chi_{\mathrm{BH}}^2}}, \tag{5.6}$$

and $f(\Omega_{\mathrm{H}})$ is a high-spin correction,

$$f(\Omega_{\mathrm{H}}) = 1 + 1.38\Omega_{\mathrm{H}}^2 - 9.2\Omega_{\mathrm{H}}^4. \tag{5.7}$$

For BHNS mergers we calculate the remnant spin using Eq. 11 from Pannarale (2013), while for NSNS mergers we use Eq. 5.3 (Coughlin and Dietrich 2019).

Giacomazzo et al. (2015) found that after the merger the magnetic field energy density can be amplified by magneto-rotational and Kelvin-Helmholtz instabilities up to a fraction of the rest-mass energy density of the accretion disk, given by

$$B^2 \propto \frac{c^5}{G^2} \dot{M} M_{\mathrm{BH}}^{-2}, \tag{5.8}$$

with $\dot{M}$ the mass accretion rate on the BH. Substituting this relation in Eq. 5.5 one can find

$$L_{\rm BZ} \propto \dot{M}\Omega_{\rm H} f(\Omega_{\rm H}). \tag{5.9}$$

General-relativistic hydrodynamic (GRHD) simulations of NSNS/BHNS mergers with a launched jet are consistent with this scaling (Shapiro 2017).

As explained above, for BHNS case very low-mass ejecta pollute the polar direction, thus the jet is always "successful" and the energy loss in overcoming the ejecta is negligible. Its kinetic energy can be expressed as

$$E_{\rm K,j} = L_{\rm BZ} \times t_{\rm acc}, \tag{5.10}$$

where $t_{\rm acc}$ is the disc accretion duration,

$$t_{\rm acc} = \frac{(1-\xi_{\rm w}-\xi_{\rm s})M_{\rm disk}}{\dot{M}}. \tag{5.11}$$

$\xi_{\rm w}$ and $\xi_{\rm s}$ represent the disk mass fraction flowing in wind and secular ejecta, respectively. Thus $(1-\xi_{\rm w}-\xi_{\rm s})$ is the mass that is effectively accreted on the BH. Substituting Eq. 5.9 in Eq. 5.10 one can find

$$E_{\rm K,jet} = \epsilon(1-\xi_{\rm w}-\xi_{\rm s})M_{\rm disk}c^2\Omega_{\rm H}^2 f(\Omega_{\rm H}), \tag{5.12}$$

where ϵ is a dimensionless constant depending on the large-scale geometry of the magnetic field, the disk aspect ratio (Tchekhovskoy et al. 2010) and the ratio of magnetic field energy density to disk pressure at saturation (Hawley et al. 2015). Shapiro (2017) indicate that ϵ only slightly changes for different system configurations. In order to find a likely value for ϵ, we compare the maximum achievable jet's kinetic energy with the maximum of observed sGRB energy distribution. The most energetic sGRB observed to date is GRB090510, with $E_{\gamma,\rm iso} \sim 7.4 \times 10^{52}$ erg (D'Avanzo et al. 2014). Assuming that 10% of the kinetic energy is converted in γ-rays and a jet opening angle $\theta_{\rm j} = 5$ deg (that is the typical measured value for sGRBs, see i.e. Fong et al. 2015), the inferred kinetic energy for GRB090510 is $E_{\rm K,j} \sim 3 \times 10^{51}$ erg. In Eq. 5.12 the upper limit for the factor $\Omega_{\rm H}^2 f(\Omega_{\rm H})$ is 0.2 and the upper limit for the disk mass is the total NS mass ($\sim 2-2.5M_\odot$, depending on the EoS). Therefore setting $\epsilon = 0.015$ the corresponding maximum achievable jet's kinetic energy is $\sim 10^{52}$ erg, consistent with observations.

5.3.3 Jet structure

The GRB jets have a structure, that describes the angular distribution of energy (Salafia et al. 2015, Kathirgamaraju et al. 2019). The "core" is the very narrow central region with uniform distributions. The core opening angles for constant kinetic energy $\theta_{\rm c,E}$

and constant Lorentz factor $\theta_{\rm c,\Gamma}$ can be different. The "wings" are all the jet regions outside the core ($\theta > \theta_{\rm c}$, where θ is measured from the jet's axis). Salafia et al. (2019b), Kathirgamaraju et al. (2019) indicated an educated guess for the angular distributions of Lorentz factor and kinetic energy per solid angle in the jet:

$$\Gamma(\theta) = 1 + (\Gamma_{\rm c} - 1)e^{-(\theta/\theta_{\rm c,\Gamma})^2}, \tag{5.13}$$

$$\frac{dE}{d\Omega}(\theta) = E_{\rm c}e^{-(\theta/\theta_{{\rm c},E})^2}, \tag{5.14}$$

where $\theta_{\rm c,E} = 0.1$ rad, $\theta_{\rm c,\Gamma} = 0.2$ rad, $\Gamma_{\rm c}$ is the core's Lorentz factor and $E_{\rm c}$ is the core's kinetic energy,

$$E_{\rm c} = E_{\rm K,jet}/(\pi\theta^2_{\rm c,E}). \tag{5.15}$$

Fig 5.4 shows the angular distribution of the Lorentz factor (solid blue line) and of the isotropic equivalent energy $E_{\rm k,iso} = 4\pi dE/d\Omega(\theta)$ normalised to the core's value (dashed grey line).

5.4 GRB prompt emission

I calculate the GRB prompt emission following Salafia et al. (2015, 2019a,b). As explained above, internal shocks and/or magnetic reconnection cause the prompt emission by dissipating a fraction η of the jet's kinetic energy in γ-ray photons. A typical value is $\eta = 10\%$ (Salafia et al. 2019a). Considering an observer whose viewing angle is $\theta_{\rm v}$, the measured GRB prompt isotropic equivalent energy is obtained by integrating the emission over the jet (also accounting for relativistic beaming). In order to do so, the jet's front ("head") can be divided in sub-regions with angular coordinates θ and ϕ (see Fig. 5.5). One thus obtain:

$$E_{\rm iso}(\theta_{\rm v}) = \eta \int \frac{\delta^3}{\Gamma}\frac{dE}{d\Omega}d\Omega, \tag{5.16}$$

where δ is the relativistic Doppler factor,

$$\delta = \frac{1}{\Gamma(1-\beta\cos\alpha)}, \tag{5.17}$$

with $\beta = v/c$. α is the angle between each jet's head sub-region's unit normal vector and the observer's line of sight, namely

$$\alpha = \cos\theta\cos\theta_v + \sin\phi\sin\theta\sin\theta_v, \tag{5.18}$$

where θ and ϕ are the angular coordinates of each sub-regions in the jet's head (see Figs. 5.5-5.6). Fig. 5.4 shows the observed prompt emission isotropic equivalent energy $E_{\rm iso}$

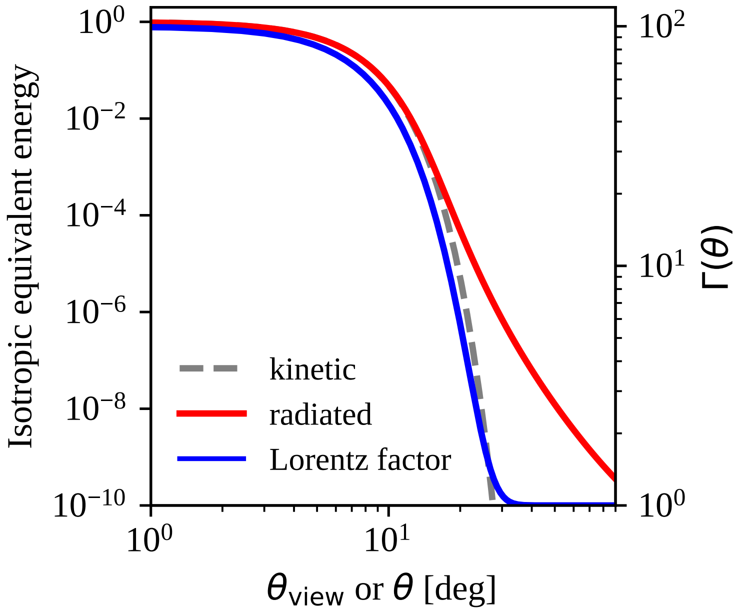

Fig. 5.4 Angular distribution of the Lorentz factor (solid blue line, values on the right y-axis) and of the isotropic equivalent energy $E_{\text{k,iso}} = 4\pi dE/d\Omega(\theta)$ normalised to the core's value (dashed grey line, values on the left y-axis). The solid red line shows the observed prompt emission isotropic equivalent energy E_{iso} as a function of the observer's viewing angle, normalised to $E_{\text{iso}}(\theta_{\text{v}} = 0)$ (on-axis observer).

as a function of the observer's viewing angle (red solid line), normalised to $E_{\text{iso}}(\theta_{\text{v}} = 0)$ (on-axis observer).

5.5 GRB afterglow emission

If the jet has enough energy to overcome the ejecta ("breakout") it continues expanding in the ISM, sweeping material. When the rest mass energy of the swept material times the jet's Lorentz factor squared equals $E_{\text{K,j}}$, the jet begins to decelerate, inducing the formation of a relativistic forward shock. ISM electrons close to the shock are accelerated and produce syncrotron radiation, powering the GRB afterglow emission.

The electrons in the "upstream" region (behind the forward shock) are accelerated through the Fermi process, reaching a non-thermal power-law energy distribution. Fermi process simulations in magnetised relativistic shocks (Sironi et al. 2013) indicate that the index of the electron distribution is $p = 2.3$. The total energy density in the upstream region can be calculated using shock jump conditions (Blandford and McKee 1976). A fraction ϵ_{e} of the total energy is given to the electrons, while a fraction ϵ_{B} to the magnetic field. From the analysis of the ratio of radio to GeV emission energy in LGRBs Nava et al. (2014), Beniamini and van der Horst (2017) found $\epsilon_{\text{e}} \sim 0.1$. However several degeneracies exist, so it is difficult to reliably constrain ϵ_{e} from observed

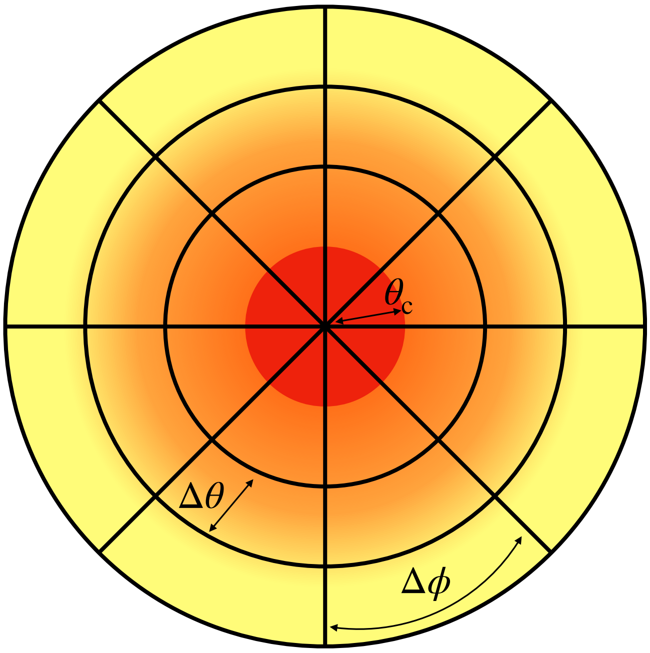

Fig. 5.5 Schematic representation of jet's head sub-regions. The red central region is the jet's core.

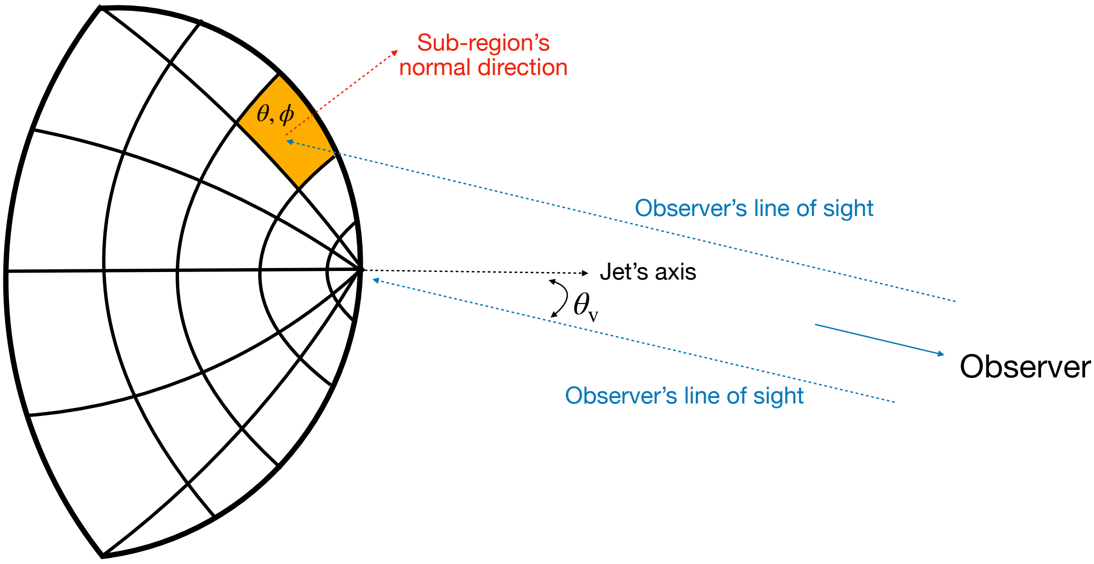

Fig. 5.6 Schematic representation of observer's position with respect to a given jet's head sub-region.

GRB afterglows. Granot and van der Horst (2014), Santana et al. (2014), Zhang et al. (2015), Beniamini et al. (2016) constrained $\epsilon_{\rm B}$ in the range $10^{-4} \lesssim \epsilon_{\rm B} \lesssim 10^{-1}$.

I adopt forward shock dynamics and synchrotron emission models from Salafia et al. (2019a) (that is an upgrade of models from D'Avanzo et al. 2018, Ghirlanda et al. 2019). I assume a constant ISM density $n = 10^{-3}$ cm^{-3}. This value is consistent with both estimates from GW170817 associated GRB analysis (Ghirlanda et al. 2019) and typical observed sGRBs with modelled afterglow emission (Fong et al. 2015). Moreover the assumption of such a low-density environment is consistent with expectations that, due to supernova kicks, the NSNS/BHNS merging sites are displaced with respect to the initial star-forming region birth sites (Voss and Tauris 2003).

5.5.1 Dynamics

Fig. 5.5 shows the assumed spherical coordinate system on the jet's head. The jet's axis coincides with the z-axis, θ is the latitudinal angle and ϕ is the azimuthal angle. Fig. 5.6 shows that the viewing angle $\theta_{\rm v}$ is the angle between the jet's axis and the observer's line of sight. In the following, I will refer to a jet's head sub-region with latitudinal angle $\theta - d\theta < \theta < \theta + d\theta$ as "annulus". I consider each annulus to be independent from the others, thus I neglect lateral expansion (that is caused by energy exchanges between the annuli).

At a distance R from the launch region ("radius") the jet has swept an ISM mass per unit solid angle given by

$$\mu(R) = \frac{R^3}{3} n m_{\rm p}, \tag{5.19}$$

where $m_{\rm p}$ is the proton mass (under the assumption that the ISM is only composed of hydrogen). Following Panaitescu and Kumar (2000), Granot and Kumar (2003) the forward shock dynamics can be computed imposing energy conservation. The upstream material's Lorentz factor is given by

$$\Gamma(R,\theta) = \frac{\mu_0}{2\mu(R)} \left[\sqrt{1 + \frac{4\mu(R)[\mu(R) + \mu_0 + c^{-2} dE/d\Omega(R,\theta)]}{\mu_0^2}} - 1 \right], \tag{5.20}$$

where

$$\mu_0(\theta) = \frac{dE/d\Omega(R=0,\theta)}{\Gamma(R=0,\theta)c^2}. \tag{5.21}$$

Blandford and McKee (1976) found that the upstream shocked material lies in a thin layer. Its thickness ΔR can be calculated imposing electron number conservation and assuming that inside the layer there is a uniform radial density distribution. Using shock jump conditions (Blandford and McKee 1976), the shocked region's electron number density is

$$n_{\rm s} = n\frac{\gamma_{\rm a}\Gamma+}{\gamma_{\rm a}-1}, \tag{5.22}$$

where $\gamma_{\rm a}$ is the adiabatic index in the region ahead the shock ("downstream"), computed as in Pe'er (2012). ΔR is given by

$$\Delta R = \frac{R(\gamma_{\rm a}-1)}{3(\gamma_{\rm a}\Gamma+1)\Gamma}. \tag{5.23}$$

The shocked material is slower than the forward shock, thus ΔR increases with time. Blandford and McKee (1976) found that the Lorentz factor of the forward shock is given by

$$\Gamma_{\rm s} = [\gamma_{\rm a}(\Gamma-1)+1]\sqrt{\frac{\Gamma+1}{\gamma_{\rm a}(2-\gamma_{\rm a})(\Gamma-1)+2}}. \tag{5.24}$$

5.5.2 Equal-arrival time surfaces

At each time, the observer receives photons that were emitted by the shocked regions at different times. Since the thickness of the emitting region is negligible when compared to the radius ($\Delta R \ll R$), the assumption that photons are emitted by the jet's head is a good approximation. The arrival time for photons emitted by the jet's head sub-region with coordinates θ and ϕ, when the jet's radius is R, to the observer whose viewing angle is $\theta_{\rm v}$ is given by

$$t_{\rm obs}(R,\theta_{\rm v},\theta,\phi) = (1+z)\int_0^R \frac{1-\beta_{\rm s}\cos\alpha}{\beta_{\rm s}c}dR, \tag{5.25}$$

where $\beta_{\rm s}$ is the shock's velocity divided by c, α is defined in Eq. 5.18 and z is the redshift. The shock's surface brightness can be expressed as

$$I_\nu(\nu,\theta,\phi,R) = \Delta R' j'_{\nu'}(\nu/\delta)\delta^3, \tag{5.26}$$

where the primes indicate quantities calculated in the comoving frame. δ is the shocked material's Doppler factor (see Eq. 5.17, $\Delta R' = \Gamma\Delta R$ and $j'_{\nu'}$ is the synchrotron emissivity (see next subsection). Dividing the jet's head in sub-regions (see Fig. 5.5), I consider N bins for θ in the range $10^{-4} \leq \theta \leq \pi/2$ and M bins for ϕ in the range $-\pi/2 \leq \phi \leq \pi/2$. Thus I only compute the emission from one half of the surface, as the other half gives the same contribution (for simmetry). For a given observer time $t_{\rm obs}$, for each sub-region I calculate I_ν at the radius corresponding to $t_{\rm obs}$ (obtained by inverting Eq. 5.25). By integrating over the jet's head (θ and ϕ) the observed flux density at time $t_{\rm obs}$ is

$$F_\nu(\nu, t_{\rm obs}) = 2\frac{1+z}{d_{\rm L}^2}\int_0^1 d\cos\theta \int_{-\pi/2}^{\pi/2} d\phi R^2 I_\nu(\nu(1+z), R), \tag{5.27}$$

where the factor 2 includes the emission from the other half of the jet's head, as explained above. Eq. 5.27 indicates the emission from a single jet. When a BH accretes matter from a disk it is expected to launch two jets, in the opposite directions perpendicularly to the equatorial plane. The jet in the opposite semi-space with respect to the observer is defined "counter-jet". The flux received by the counter-jet can be computed in the same way, adding π to $\theta_{\rm v}$.

5.5.3 Radiation

I adopt the synchrotron emission model for shocked material presented in Sari et al. (1998), Panaitescu and Kumar (2000). As explained above, ISM electrons are accelerated by the forward shock, obtaining a power-law energy distribution:

$$\frac{dn_{\rm s}}{d\gamma} \propto \gamma^{-p}, \tag{5.28}$$

with $p > 2$. As explained above, a fraction $\epsilon_{\rm e}$ of the upstream energy density is given to the electrons:

$$e_{\rm e} = \epsilon_{\rm e} e = \epsilon_{\rm e}(\Gamma - 1)n_{\rm s} m_{\rm p} c^2. \tag{5.29}$$

Sari et al. (1998) indicate the minimum ("injection") Lorentz factor of electrons $\gamma_{\rm m}$ as

$$\gamma_{\rm m} = \max\left[1, \frac{p-2}{p-1}(\Gamma - 1)\frac{m_{\rm p}}{m_{\rm e}}\right], \tag{5.30}$$

with $m_{\rm e}$ the electron's mass. As clear from Eq. 5.28, the electron's γ distribution is a decreasing power-law, thus the majority of them have $\gamma = \gamma_{\rm m}$.

As explained above, a fraction $\epsilon_{\rm B}$ of the upstream energy density is given to the magnetic field. Therefore the magnetic energy density $e_{\rm B}$ is given by

$$e_{\rm B} = \frac{B^2}{8\pi} = \epsilon_{\rm B} e. \tag{5.31}$$

The upstream electrons' peak synchrotron emissivity in the comoving frame is given by van Eerten et al. (2012) (with the upgrade by Sironi et al. 2013, to include the "deep newtonian" regime):

$$j'_{\nu',\rm max} \sim 0.66\frac{q_{\rm e}^3}{m_{\rm e}^2 c^4}\frac{p-2}{3p-1}\frac{B\epsilon_{\rm e} e}{\gamma_{\rm m}}, \tag{5.32}$$

where q_e is the electron's charge. Using Eq. 5.26 the emitting surface brightness is

$$I_\mathrm{nu}(\nu) = \delta^3 \Delta R' j'_{\nu',\mathrm{max}} S(\nu'), \tag{5.33}$$

where $\nu' = \nu/\delta$ and $S(\nu')$ is the normalized spectral shape, given by a sequence of power laws that include all spectral orderings (see Granot and Sari 2002). The different power-law branches connect in correspondence of particular break frequencies, namely ν_m, ν_c, ν_a and ν_ac.

ν_m is the synchrotron frequency for "injection" electrons:

$$\nu_\mathrm{m} = \frac{\gamma_\mathrm{m}^2 q_\mathrm{e} B}{2\pi m_\mathrm{e} c}. \tag{5.34}$$

Above a particular value of the Lorentz factor, γ_c, the electrons loose their energy through synchrotron emission on a timescale that is smaller than the expansion dynamical timescale (over which "new" electrons are injected upstream). γ_c is given by

$$\gamma_\mathrm{c} = \frac{6\pi m_\mathrm{e} c^2 \Gamma \beta}{\sigma_\mathrm{T} B^2 R}, \tag{5.35}$$

where σ_T is the Thomson cross section. ν_c is the synchrotron frequency corresponding to γ_c.

If $\nu_\mathrm{m} > \nu_\mathrm{c}$ the electrons loose their energy faster than the "new electrons refill" of the shocked region. This regime is the "fast cooling". If instead $\nu_\mathrm{m} < \nu_\mathrm{c}$ the majority of electrons have $\gamma < \gamma_\mathrm{c}$, thus the timescale of their energy loss through synchrotron emission is longer than the expansion timescale. This regime is the "slow cooling". Free-free transitions can cause re-absorption by electrons of emitted photons before they leave the shocked region. This process is the synchrotron "self-absorption" and happens below the frequency ν_a (Panaitescu and Kumar 2000). In the fast cooling regime there is another break frequency $\nu_\mathrm{ac} < \nu_\mathrm{a}$ in the spectral region that is self-absorbed, because electrons at different cooling stages produce a non-homogeneous distribution (Granot et al. 2000).

5.5.4 GRB afterglow example light curves

Fig. 5.7 shows some GRB afterglow example light curves. I considered a BHNS merger with $M_\mathrm{BH} = 5M_\odot$, $\chi_\mathrm{BH} = 0.5$, $M_\mathrm{NS} = 1.4M_\odot$, $\Lambda_\mathrm{NS} = 334$ (corresponding to SFHo EoS), at a distance $d_\mathrm{L} = 250$ Mpc. Using the fitting formula presented in §3.4 and Eq. 5.12 the launched jet's energy is $E_\mathrm{K,jet} \sim 2 \times 10^{49}$ erg. The corresponding jet's core isotropic equivalent energy is $E_\mathrm{c} \sim 8 \times 10^{51}$ erg. Fig. 5.7 shows the emission in the radio (red), optical (green) and X (black) bands. The three panels refer to different viewing angles: $\theta_\mathrm{v} = 0$ deg (on-axis observer, left panel), $\theta_\mathrm{v} = 30$ deg (central panel)

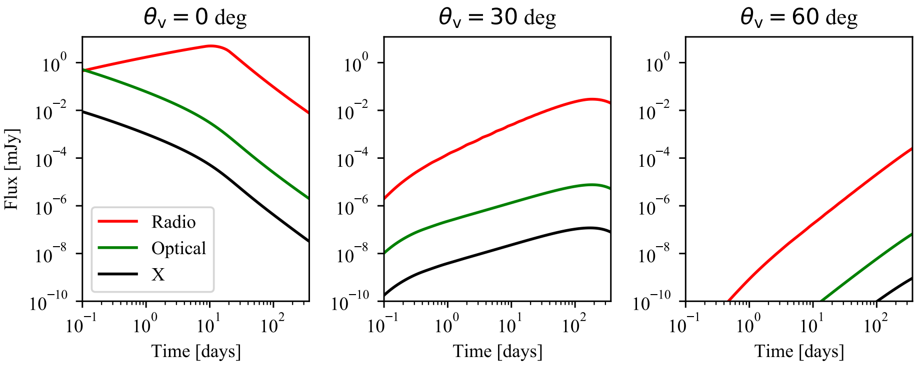

Fig. 5.7 Example GRB afterglow light curves in the radio (red), optical (green) and X (black) bands. The left panel refers to $\theta_v = 0$ deg (on-axis observer), the central panel to $\theta_v = 30$ deg and the right panel to $\theta_v = 60$ deg.

and $\theta_v = 60$ deg (very off-axis observer, right panel). It is evident that for larger viewing angles the observed GRB afterglow light curves are dimmer and peak later.

Indeed on-axis observers immediately receive photons emitted by the jet's core. Thus they see an initially bright light curve that decreases in time as the jet's emissivity decreases during its expansion. The only exception is the radio band, where at early time the emission is self-absorbed. Instead off-axis observers initially receive photons only from the outer jet regions (due to relativistic beaming). These regions are less energetic (Eq. 5.14) and their emissivity is lower. Over time, the Lorentz factor decreases (Eq. 5.13), and the observers receive photons from inner (more energetic) regions (thanks to the widening of the relativistic beaming cone). Thus they see an increasing light curve until they receive the jet core's emission, representing the observed peak. The brightness of this peak is much lower with respect to the on-axis case, as the jet's core emission is observed at later time, when the core's emissivity has decreased. After that, the off-axis observers see a decreasing light curve. Fig. 5.8 is a simple sketch showing this effect. The aforementioned argument is the reason why I neglect the counter-jet emission, as it would be a dim contribution at late times, due to the large angle with respect to the observer's direction ($\theta_v + \pi$).

5.6 Kilonova radio remnant

After powering the KN emission, the NSNS/BHNS merger ejecta continue their propagation in the ISM. The outer (and faster) ejecta regions have supersonic velocity (v$\gtrsim 0.3$ c) and a shock is created. Progressively the inner slower ejecta cross the reverse shock and transfer their energy to the shocked region. Hotokezaka et al. (2016) found a relation between the shocked material's Γ and the forward shock radius R (using energy

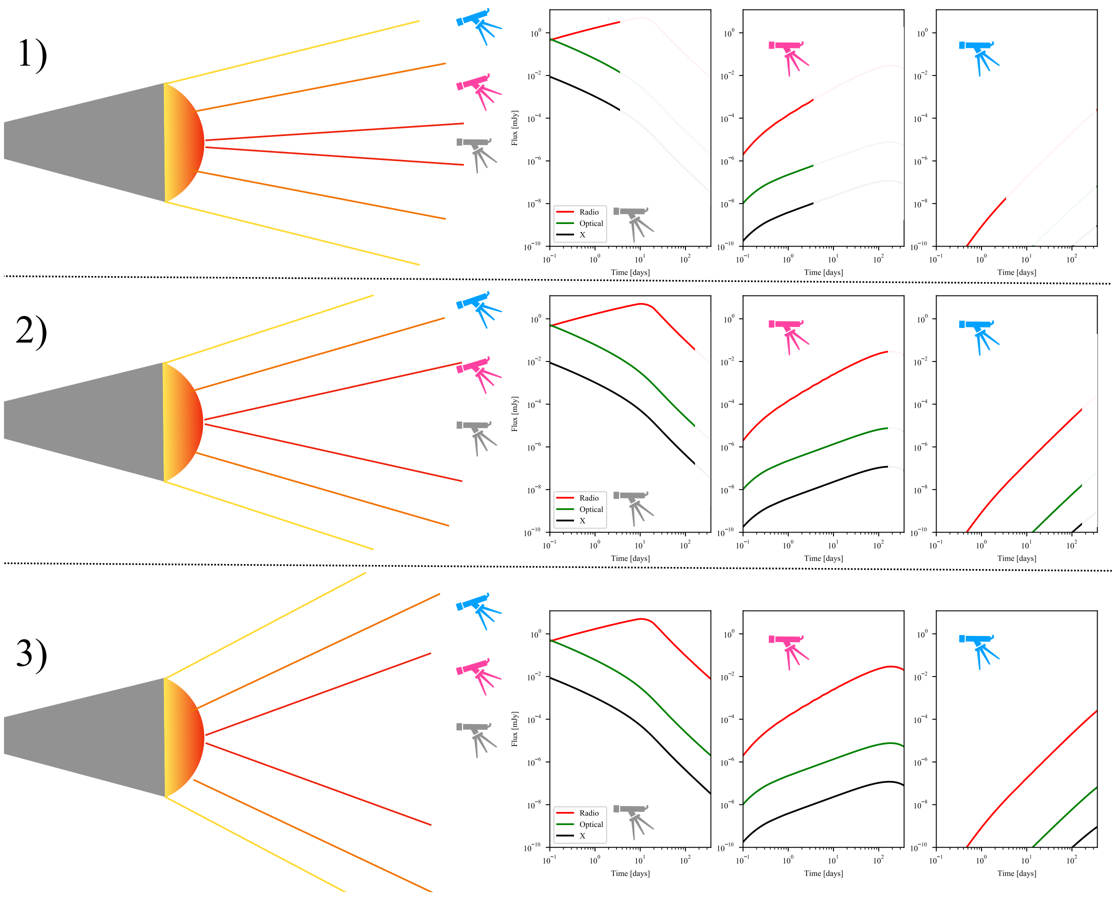

Fig. 5.8 Simple sketch showing how the viewing angle affects the observed GRB afterglow light curve. Here I consider on-axis (gray), slightly off-axis (pink) and off-axis (blue) observers. At early time (1) only the on-axis observer receives the jet's core emission (red cone). Then (2) also the slightly off-axis observer receives photons from the jet's core (corresponding to the observed peak). At late time (3) the off axis observer still detects a dim increasing light curve, as he does not receive yet the photons from the jet's core. See text for a full description. For simplicity the GRB afterglow light curves are the same of Fig. 5.7.

and momentum conservation)

$$\Omega\frac{R^3}{3}m_{\rm p}n(c\beta\Gamma)^2 \sim E(>\beta), \tag{5.36}$$

where $m_{\rm p}$ is the proton mass, n is the ISM number density, Ω is the ejecta solid angle. $E(>\beta)$ is the kinetic energy of ejecta with velocity above βc, namely

$$E(>\beta) = \int_{\beta c}^{v_{\rm max}} (\Gamma - 1)\frac{dm}{d{\rm v}}c^3 d\beta, \tag{5.37}$$

where $dm/d{\rm v}$ is given by Eq. 4.3. After all the inner shells crossed the reverse shock, the ejecta continue expanding quasi-adiabatically, with $\Gamma\beta \propto R^{-3/2}$. As for the GRB afterglow, ISM electrons close to the shock produce synchrotron radiation, mostly in the radio band. Nakar and Piran (2011) defined this emission “radio flare”. In Barbieri et al. (2019a), due to the slow evolution of this transient ($\sim$ years) and to the similarity with supernova radio remnant, this emission was defined “kilonova radio remnant”. Hotokezaka and Piran (2015) presented example light curves of kilonova radio remnant produced by NSNS and BHNS mergers. They found that these light curves can have a peak flux $\sim$ mJy at very late times (several years). However the kilonova radio remnant light curves strongly depend on the assumed model parameters (i.e. n). In Barbieri et al. (2019a) I modelled synchrotron emission for this transient similarly to GRB afterglows. I only considered dynamical ejecta, as the other components have smaller velocities and decelerate even later. I found that the kilonova radio remnant light curves become relevant only at $t \gtrsim 30$ years.

CHAPTER 6

Analysis

In this chapter I present the different analysis performed during my PhD research and the main achieved results. § 6.1 shows the results from Barbieri et al. (2019a, 2020a). § 6.2 shows the results from Barbieri et al. (2019a,b, 2020b). Finally, § 6.3 represents the starting point of a future work (Barbieri et al. 2020c, in preparation).

6.1 EM counterparts dependence on BH and NS properties

In this section I investigate the EM counterparts dependence on the NSNS/BHNS binary properties. As explained above, the kilonova and GRB afterglow light curve behaviour is affected by the ejecta properties (besides the modeling parameters). Therefore it is important to understand how binary properties affect the ejecta production and, consequently, the EM emission.

6.1.1 NSNS

The properties of ejecta from NSNS mergers are computed using Eqs. 3.2-3.3 (Radice et al. 2018a) and Eq. 3.4 (Barbieri et al. 2020b). Thus they depend on the NS masses and tidal deformabilities (using Eqs. 3.17-3.18 to compute the NS baryonic mass and compactness). Assuming that both NSs are described by the same EoS, in Fig. 6.1 I show the ejecta mass dependence on the NS masses for APR4, SFHo and DD2 EoS (all consistent with actual constraints from GW signals GW170817/GW190425 and the NICER results, see LVC 2019*e*, 2020*c*, Miller et al. 2019a, Riley et al. 2019). The black dashed line indicates the equal-mass limit ($M_1 = M_2$). In general more massive ejecta are produced for low-mass secondary NS, as it is more deformable. For stiffer EoS, the production of massive dynamical ejecta requires large mass ratios (asymmetric binaries). Moreover for $M_2 \gtrsim 1.5-1.6 M_\odot$ (depending on the EoS) no dynamical ejecta are produced.

In Fig. 6.2 I show kilonova light curves for several NSNS binary configurations and EoS in two bands. According to Fig. 6.1, stiffer EoS correspond to more deformable NSs, whose merger produce more massive ejecta and consequently brighter kilonovae. This effect can be seen moving from left panel (APR4 EoS, soft) to right panel (DD2

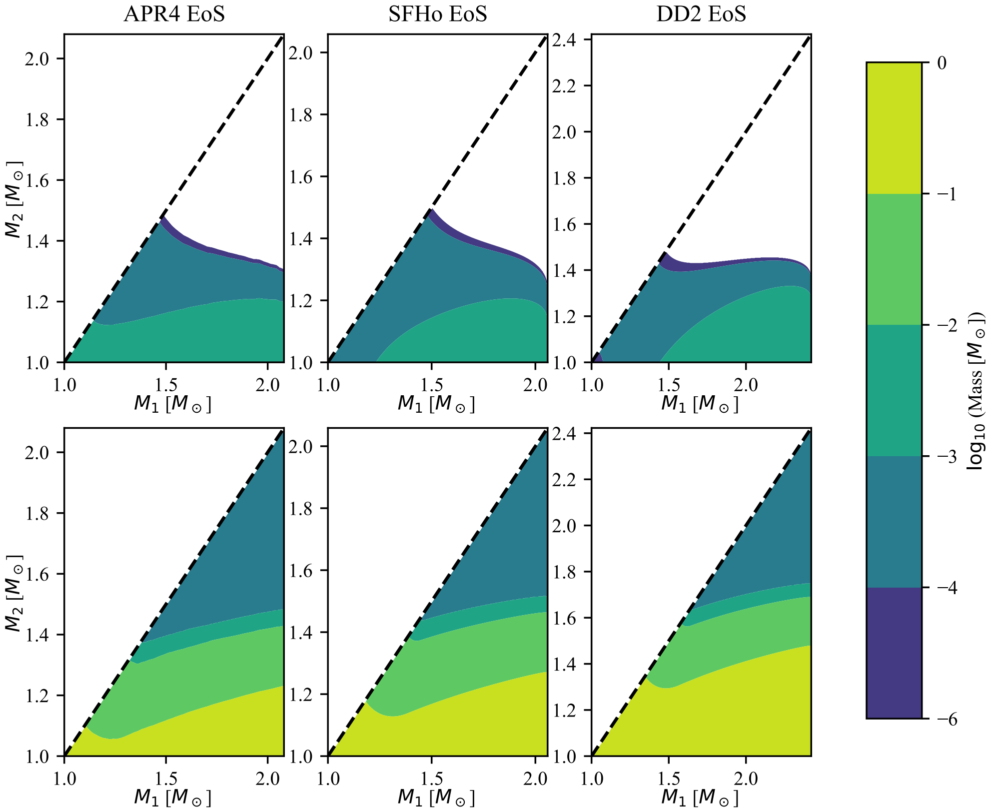

Fig. 6.1 NSNS dynamical ejecta (top row) and accretion disc (bottom row) mass dependence on the NS masses for APR4 (left column), SFHo (central column) and DD2 EoS (right column). The black dashed line indicates the equal-mass limit ($M_1 = M_2$).

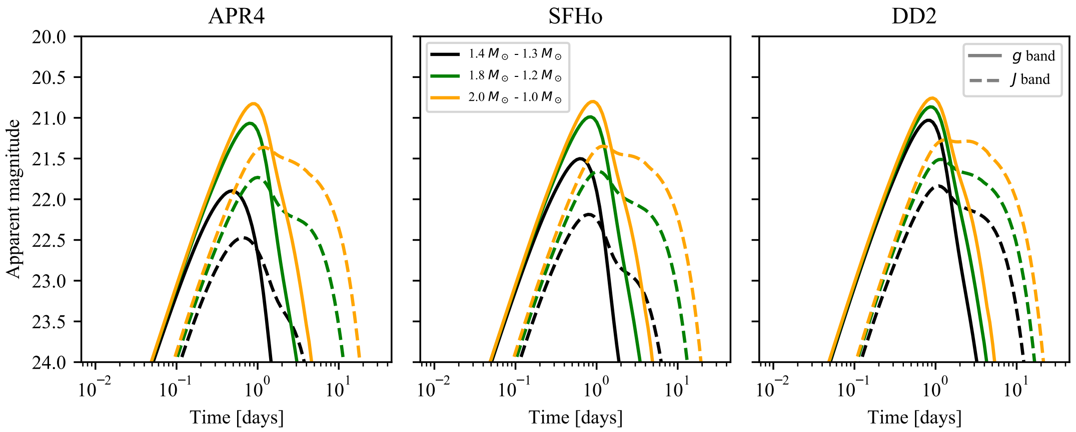

Fig. 6.2 Kilonova light curves dependence on NSNS binary configurations (different colors) and EoS (different columns) in two bands (different linestyles).

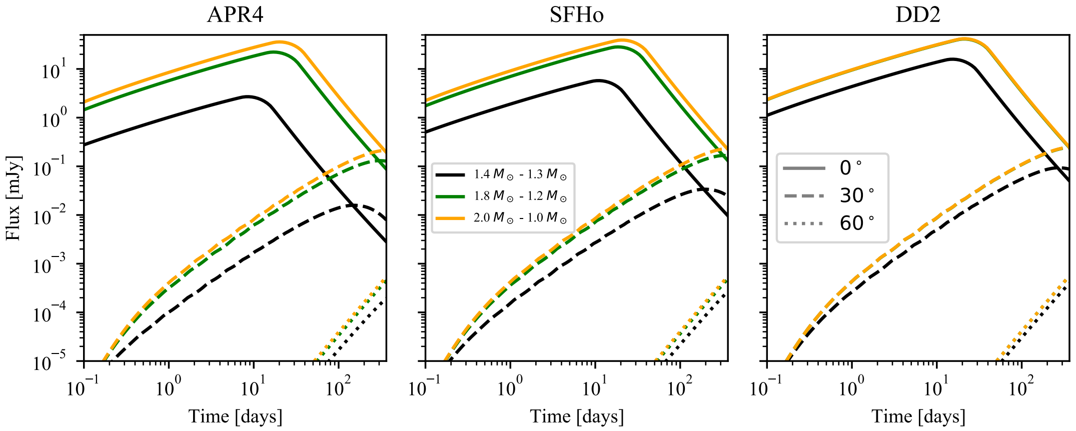

Fig. 6.3 GRB afterglow light curves dependence on NSNS binary configurations (different colors) and EoS (different columns) for three viewing angles (different linestyles).

EoS, stiff). As shown above, asymmetric NSNS binaries hosting a low-mass secondary NS also produce more massive ejecta and consequently brighter kilonovae, as can be seen moving from black lines ($M_1 = 1.4M_\odot - M_2 = 1.3M_\odot$, almost symmetric) to orange ones ($M_1 = 2M_\odot - M_2 = 1M_\odot$, very asymmetric).

The same arguments as above hold also for GRB afterglow light curves, presented in Fig. 6.3.

6.1.2 BHNS

The properties of ejecta from BHNS mergers are computed using Eqs. 3.7-3.11 (Kawaguchi et al. 2016) and Eq. 3.12 (Foucart et al. 2018). Thus they depend on[1] $M_{\rm BH}$, $M_{\rm NS}$, $\Lambda_{\rm NS}$,

---

[1] As explained in Barbieri et al. (2019a), I neglect the NS spin. Indeed even if the NS forms rapidly spinning it has time to spin-down (through dipole emission) before the merger. Moreover the NS can not spin-up through matter accretion, as its companion is a BH. Thus before tidal locking the NS spin is ~ 0

$\chi_{\rm BH}$ and $\iota_{\rm tilt}$. For simplicity in the following I consider $\iota_{\rm tilt} = 0$, corresponding to non-precessing binaries, with aligned BH spin vector and orbital angular momentum. In Fig. 6.4 I show the BHNS ejecta mass dependence on the binary parameters. The first row indicates how the BH properties ($M_{\rm BH}$ and $\chi_{\rm BH}$) affect the ejecta mass, fixing the NS mass and tidal deformability ($M_{\rm NS} = 1.4M_\odot$ and $\Lambda_{\rm NS} = 330$, corresponding to SFHo EoS). The general result is that more massive ejecta are produced for low-mass/rapidly-spinning BHs. Indeed such BHs have smaller $R_{\rm ISCO}$, favoring the NS tidal disruption to happen outside the event horizon. The second row instead indicates how $M_{\rm NS}$ and $\Lambda_{\rm NS}$ affect the ejecta mass, for a given BH ($M_{\rm BH} = 5M_\odot$ and $\chi_{\rm BH} = 0.3$). Of course not all $M_{\rm NS} - \Lambda_{\rm NS}$ configurations are possible, as the two parameters must obey an EoS. APR4, SFHo and DD2 EoS are plotted with gray symbols. Moving along these lines (representing physically possible NS configurations) it is clear that more massive ejecta are produced for low-mass/large-deformability NSs.

In Fig. 6.5 I show kilonova light curves for several BHNS binary configurations and EoS in two bands. According to Fig. 6.4, more massive ejecta and consequently brighter kilonovae are produced for low-mass BHs (fixing $\chi_{\rm BH}$, $M_{\rm NS}$ and $\Lambda_{\rm NS}$), as can be seen in the top-left panel (moving from pink to purple lines). Instead fixing $M_{\rm BH}$, $M_{\rm NS}$ and $\Lambda_{\rm NS}$, brighter kilonova emission is produced for rapidly-spinning BHs, as shown in the top-right panel (moving from blue to black lines). Moreover fixing $M_{\rm BH}$, $\chi_{\rm BH}$ and the EoS, binaries with low-mass NSs produce more massive ejecta, as can be seen in the bottom-left panel (moving from yellow to red lines). Finally, fixing $M_{\rm BH}$, $\chi_{\rm BH}$ and $M_{\rm NS}$, brighter kilonovae are produced for stiffer EoS, as shown in the bottom-right panel (moving from aqua to dark green lines).

The same arguments as above hold also for GRB afterglow light curves, presented in Fig. 6.6.

6.2 GW+EM multi-messenger astronomy

As can be seen in Figs. 6.2-6.6 there is a large degree of degeneracy between kilonova and GRB light curves from different BHNS/NSNS configurations. Moreover, there is a degeneracy also between the two different system natures. Indeed similar EM counterparts can be produced by some combinations of BHNS and NSNS binary parameters. As an example, in Fig. 6.7 I show some BHNS configurations whose kilonova mimic the one observed for GW170817 (for additional examples see Barbieri et al. 2020a).

Therefore, due to these large degeneracies, it is impossible to infer the binary properties only through the EM observations. Similarly, in some cases the nature of the merging system can not be identified only through the GW signal detection (as I will

---

and it remains negligible because the timescale for GW-driven inspiral is smaller than the tidal spin-up one (Kochanek 1992, Bildsten and Cutler 1992)

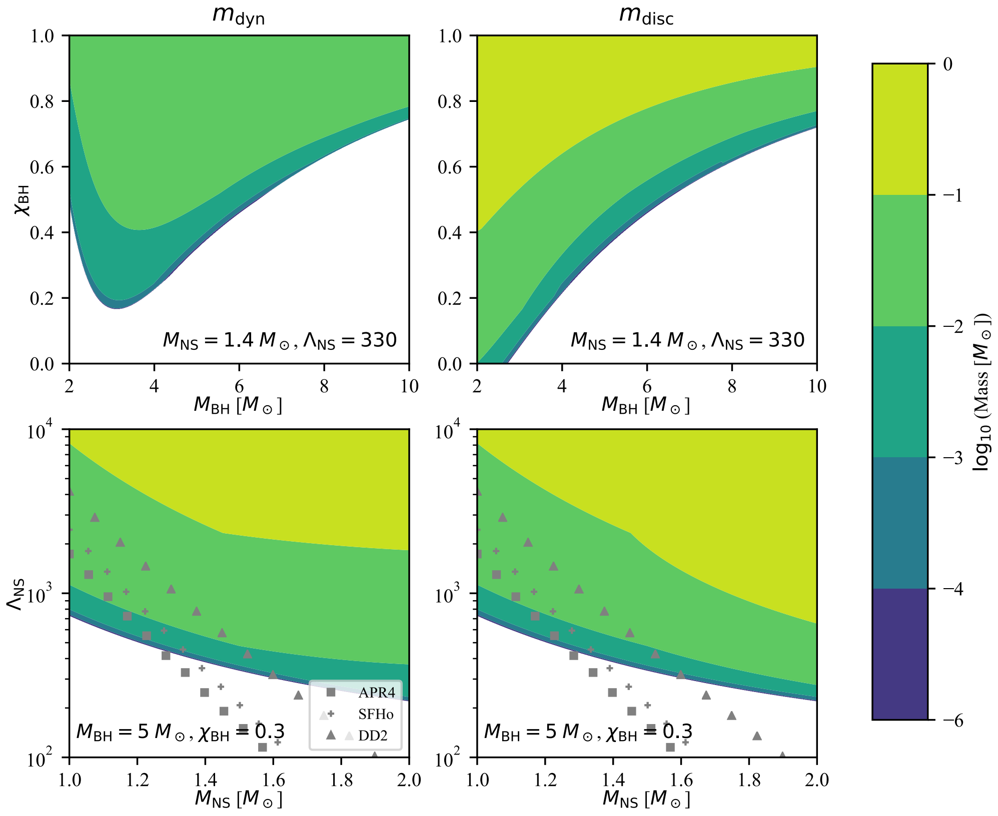

Fig. 6.4 BHNS dynamical ejecta (left column) and accretion disc (right column) mass dependence on the BH properties $M_{\rm BH} - \chi_{\rm BH}$ (top row) and NS properties $M_{\rm NS} - \Lambda_{\rm NS}$. Gray symbols indicate physically possible $M_{\rm NS} - \Lambda_{\rm NS}$ configurations, satisfying different EoS.

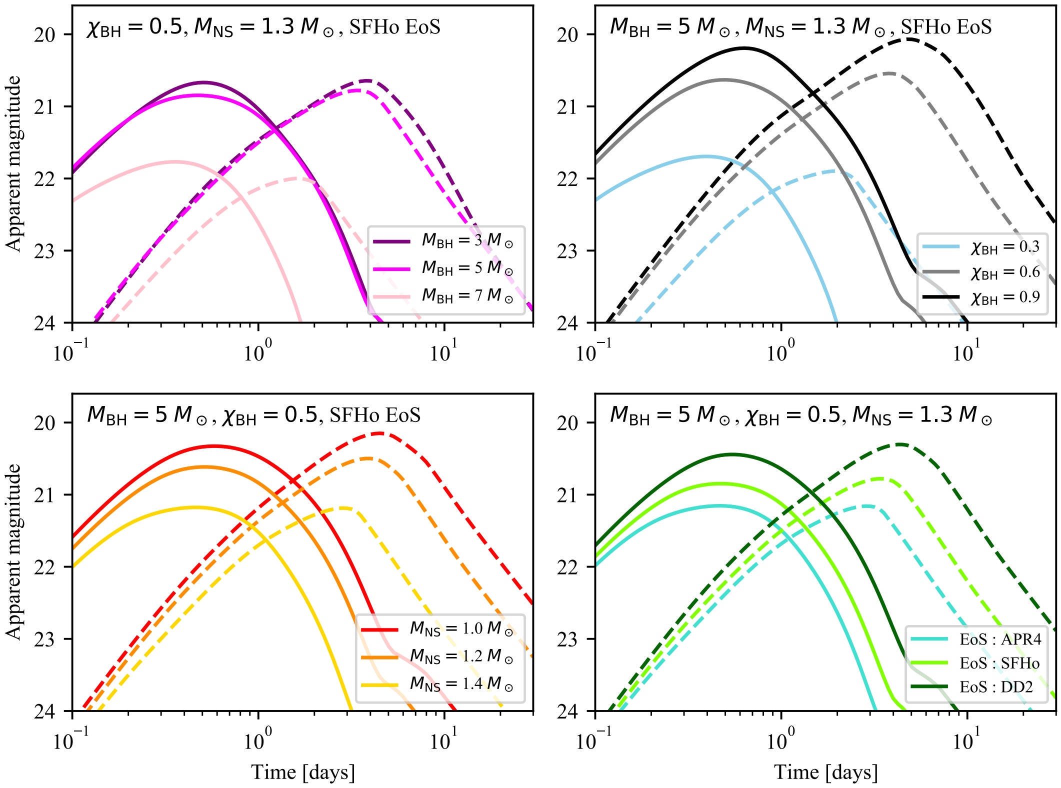

Fig. 6.5 Kilonova light curves dependence on BH mass (top-left), BH spin (top-right), NS mass (bottom-left) and EoS (bottom-right). Here I considered g (solid lines) and K (dashed lines) bands.

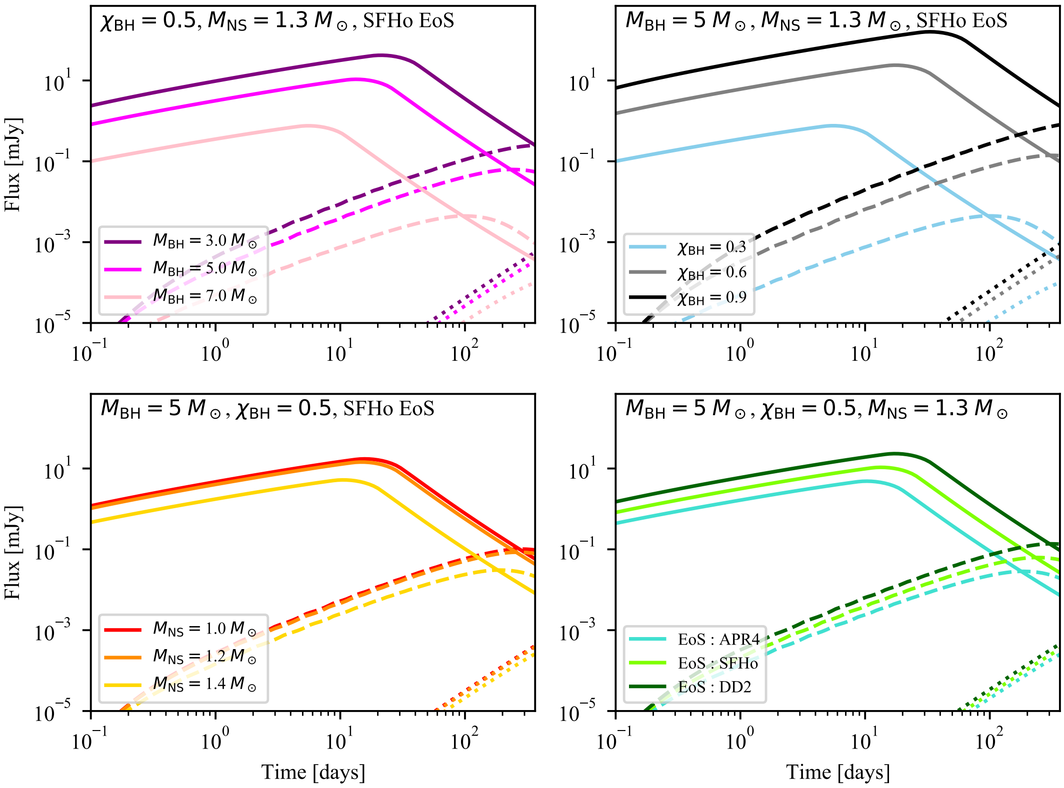

Fig. 6.6 GRB afterglow light curves dependence on BH mass (top-left), BH spin (top-right), NS mass (bottom-left) and EoS (bottom-right). Here I considered radio band and three viewing angles, namely $\theta_v = 0$ deg (solid lines), $\theta_v = 30$ deg (dashed lines and $\theta_v = 60$ deg (dotted lines).

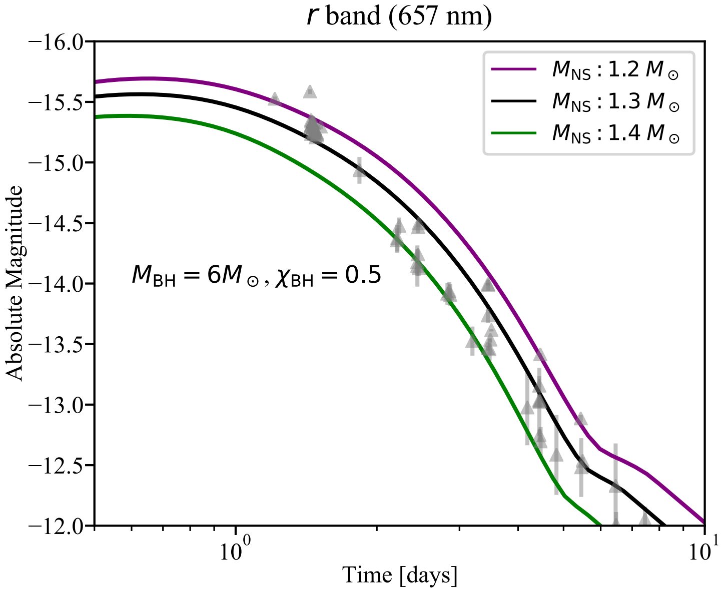

Fig. 6.7 BHNS system configurations producing a kilonova emission in the r band that mimic the GW170817 observed light curve (gray symbols). Here I consider DD2 EoS.

explain below). However combining both GW and EM observations and performing a joint analysis may succeed in breaking this degeneracy.

6.2.1 Binary parameter estimation improvement

Important constraints on the component masses and luminosity distance can be obtained in very low-latency from the GW signal analysis. Indeed the inferred d_{L} is generally released in the "Gamma-ray Coordinates Network" (GCN) few minutes after the trigger, together with the sky-localisation and the binary nature classification. The latter is based on the inferred chirp mass value (as I explain below). M_{c}, the combination of the two component masses (see Eq. 2.19), is one of the most precisely estimated binary parameters (as explained in §2.3.2). Using the Bayes' theorem, given the inferred M_{c}, the probability of having a system configuration with $M_1 - M_2$ is:

$$P(M_1, M_2|M_{\mathrm{c}}) = \frac{P(M_{\mathrm{c}}|M_1, M_2)P(M_1)P(M_2)}{P(M_{\mathrm{c}})}. \tag{6.1}$$

The uncertainty on the inferred M_{c} can be assumed as a Gaussian around the true value:

$$P(M_{\mathrm{c}}|M_1, M_2) \propto \exp\left[-\frac{1}{2}\left(\frac{M_{\mathrm{c}} - \frac{(M_1 M_2)^{3/5}}{(M_1+M_2)^{1/5}}}{\sigma_{\mathrm{c}}}\right)\right]. \tag{6.2}$$

In Fig. 6.8 I show an example of binary components' masses constraints given by the inferred chirp mass. I consider a BHNS merger with $M_{\mathrm{BH}} = 6M_{\odot}$ and $M_{\mathrm{NS}} = 1.4M_{\odot}$, whose $M_{\mathrm{c}} = 2.402M_{\odot}$. Assuming a 2% relative error, the considered measured chirp mass is $M_{\mathrm{c}} = 2.403 \pm 0.05M_{\odot}$.

As shown in Barbieri et al. (2019a), the 2D $M_1 - M_2$ posterior from GW signal analysis can be used as prior for the EM analysis.

6.2.1.1 Test case

As in Barbieri et al. (2019a) I consider a test case to show how the joint GW+EM analysis can improve the binary parameter estimation. Assuming a BHNS merger with $M_{\mathrm{BH}} = 6M_{\odot}$, $\chi_{\mathrm{BH}} = 0.8$, $M_{\mathrm{NS}} = 1.4M_{\odot}$, $\Lambda_{\mathrm{NS}} = 330$. (corresponding to SFHo EoS). As explained above, the corresponding chirp mass for such a system is $M_{\mathrm{c}} = 2.402M_{\odot}$. I assume a distance $d_{\mathrm{L}} = 230$ Mpc, a non-precessing binary ($\iota_{\mathrm{tilt}} = 0$ rad) and $\theta_{\mathrm{v}} = 0.1$ rad. As the kilonova radio remnant is difficult to detect (dim peak at very late times) and the GRB afterglow strongly depends on the viewing angle, for simplicity I consider only the kilonova emission. I assume that some loose contraints on d_{L} and θ_{v} are obtained by the low-latency GW signal analysis, and the following identification of the kilonova lead to the host galaxy identification, redshift measurement and better constraint on d_{L}. I construct a mock observed light curve in the r (657 nm) and K (2143 nm) bands,

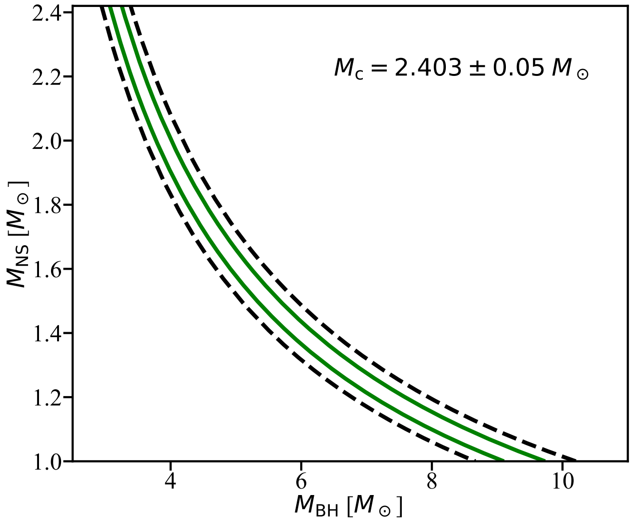

Fig. 6.8 Example of binary components' masses constraints given by the inferred chirp mass. The solid green and black dashed lines indicate, respectively, the 50% and 90% confidence levels.

assuming that observations start ~ 2.5 hours after the trigger and three observations per night are produced. I assume constant errors on magnitudes (0.2 mag for r band and 0.3 mag for K band) and observing limiting magnitudes of 24 mag (r) and 22 mag (K). In order to estimate the binary properties, I run a Markov chain Monte Carlo (MCMC) with $M_{\rm BH}$, $\chi_{\rm BH}$, $M_{\rm NS}$ and $\Lambda_{\rm NS}$ as free parameters, using the `emcee` sampler (Foreman-Mackey et al. 2013). I assume a log-flat prior on the NS tidal deformability ($1 < \log_{10}\Lambda_{\rm NS} < 4$) and flat prior on the BH spin ($0 < \chi_{\rm BH} < 1$). For $M_{\rm BH}$ and $M_{\rm BH}$ I use the 2D posterior from GW signal analysis ($M_{\rm c}$ measurement) as prior for the EM analysis, as explained above.

In Fig. 6.9 I show the joint posterior distributions for parameter pairs together with the marginalised distributions for each parameter. Red lines are the adopted priors, while blue lines indicate the "true" value with which the mock light curves were created. The best-fitting values[2] are reported in Table 6.1 (left column). Fig. 6.10 shows the mock light curves together with those obtained with the best-fitting parameters. The fit results are consistent with the "true" values, showing that the joint GW+EM analysis has the potentiality to break the degeneracy on the binary properties[3]. The binary parameter uncertainties are mainly due to the non-informative prior on $\Lambda_{\rm NS}$. As an example, I consider that in the next future the NS EoS is precisely constrained (i.e. through many NSNS GW signals and/or NICER observations) to be the SFHo. Then I repeat the MCMC with only $M_{\rm BH}$, $\chi_{\rm BH}$ and $M_{\rm NS}$ as free parameters. Indeed at each

---

[2] Obtained following the method presented in Ghirlanda et al. (2019).

[3] Of course I made some optimistic assumptions, as a close/bright enough event to be detected, a very precise sky-localisation by GW signal analysis, a very rapid and efficient EM follow-up.

	log-flat prior on $\Lambda_{\rm NS}$	fixing EoS to SFHo
$M_{\rm BH}$ [$\rm M_\odot$]	$5.74^{+0.78}_{-0.76}$	$5.93^{+0.49}_{-0.53}$
$\chi_{\rm BH}$	$0.76^{+0.11}_{-0.12}$	$0.81^{+0.04}_{-0.05}$
$M_{\rm NS}$ [$\rm M_\odot$]	$1.46^{+0.17}_{-0.14}$	$1.42^{+0.11}_{-0.08}$
$\log(\Lambda_{\rm NS})$	$2.60^{+0.17}_{-0.37}$	-

Table 6.1 MCMC best-fitting parameters. Left column refers to the run with $M_{\rm BH}$, $\chi_{\rm BH}$, $M_{\rm NS}$ and $\Lambda_{\rm NS}$ as free parameters. Right column to the run with fixed EoS (SFHo), thus $M_{\rm BH}$, $\chi_{\rm BH}$ and $M_{\rm NS}$ as free parameters.

step $\Lambda_{\rm NS}$ is computed using $M_{\rm NS}$ and assuming SFHo EoS. The best-fitting values are reported in Table 6.1 (right column). Fig. 6.11 is the analogous of Fig. 6.9. Clearly in this case the inferred binary parameters are closer to the "true" ones.

However in both cases the BH spin is constrained with an unprecedented precision. This result is very important for future observations, as to date $\chi_{\rm BH}$ is one of the less constrained parameters.

6.2.2 Distinguishing the nature of "ambiguous" systems

6.2.2.1 The mass gap and "ambiguous" systems

Up to date, the mass distribution of observed stellar BHs in coalescing binaries spans the range from $7.6^{+1.3}_{-2.1}M_\odot$ to $50^{+16.6}_{-10.2}M_\odot$ (LVC 2019*d*). For what concerns BHs observed in Galactic X-ray binaries, the mean mass is $\sim 7.8 \pm 1.2 M_\odot$ (Özel et al. 2010). Instead NSs in NSNS binaries observed to date have masses in the range $\sim 1.165 - 1.590 M_\odot$ (Zhang et al. 2019). The largest and most reliably estimated NS mass is that of the J0740+6620 radio pulsar, with $M_{\rm NS} = 2.14^{+0.10}_{-0.09}M_\odot$ (Cromartie et al. 2020). Therefore observations seem to indicate that NS and BH mass distributions are disjointed. This discontinuity is always referred to as "mass gap", extending from the maximum NS mass (computed from causality arguments, depending on the EoS) and the estimated minimum BH mass, namely from $\sim 3M_\odot$ to $\sim 5M_\odot$ (Lattimer and Prakash 2001). The compact objects' mass spectrum strongly depends on the carbon-oxygen core mass at the end of stellar evolution, on the supernova explosion engine and on the compactness at bounce of the collapsing core (Belczynski et al. 2012, Fryer et al. 2012). Besides observations, "rapid" SN explosion models (happening within $\sim 10^2$ ms after bounce) predict the existence of a mass gap. However "delayed" SN explosions (happening over more time, favoring an important amount of fallback) produce a continuous remnant mass spectrum. Interestingly, during LVC O3 observing run several candidates were reported with at least one binary component in the mass gap (i.e. LVC 2019*a*,*b*, 2020*a*,*b*). Among the others, GW190814 (LVC 2020*d*) has an inferred secondary mass $M_2 \sim 2.6M_\odot$, which could represent the most massive NS or the lightest BH ever observed. Moreover, Thompson et al. (2019) discovered a BH-red giant non-interacting

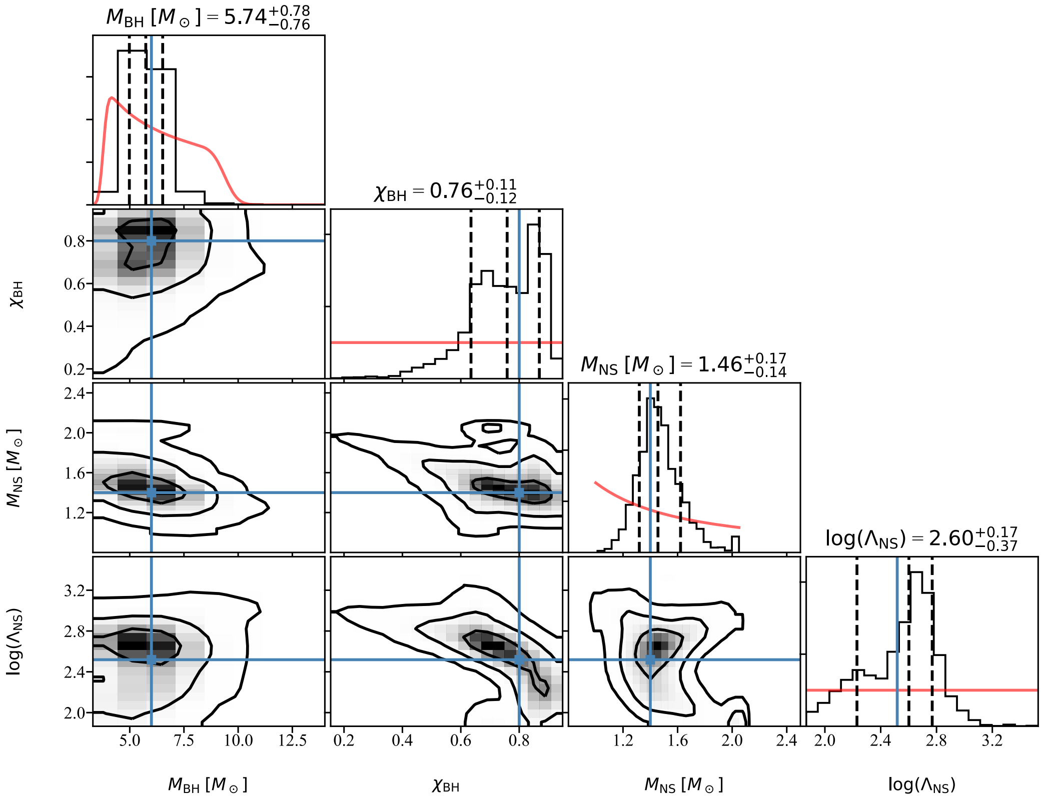

Fig. 6.9 Joint posterior distributions for parameter pairs and marginalised distributions, where the free parameters are M_{BH}, χ_{BH}, M_{NS} and Λ_{NS}. Red lines are the adopted priors, while blue lines indicate the "true" value with which the mock light curves were created. Black dashed lines in the maginalised distributions indicate the 16-th (left line), 50-th (central line) and 84-th (right line) perecentiles. Black solid lines in the joint distributions indicate 1-, 2- and 3-σ contours.

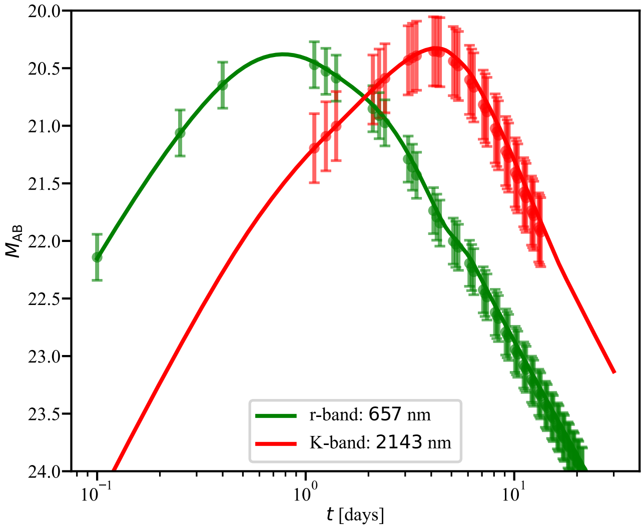

Fig. 6.10 Kilonova computed using the best-fitting parameters, in the r (green) and K (red) band. The points represent the mock light curves with $1-\sigma$ errors.

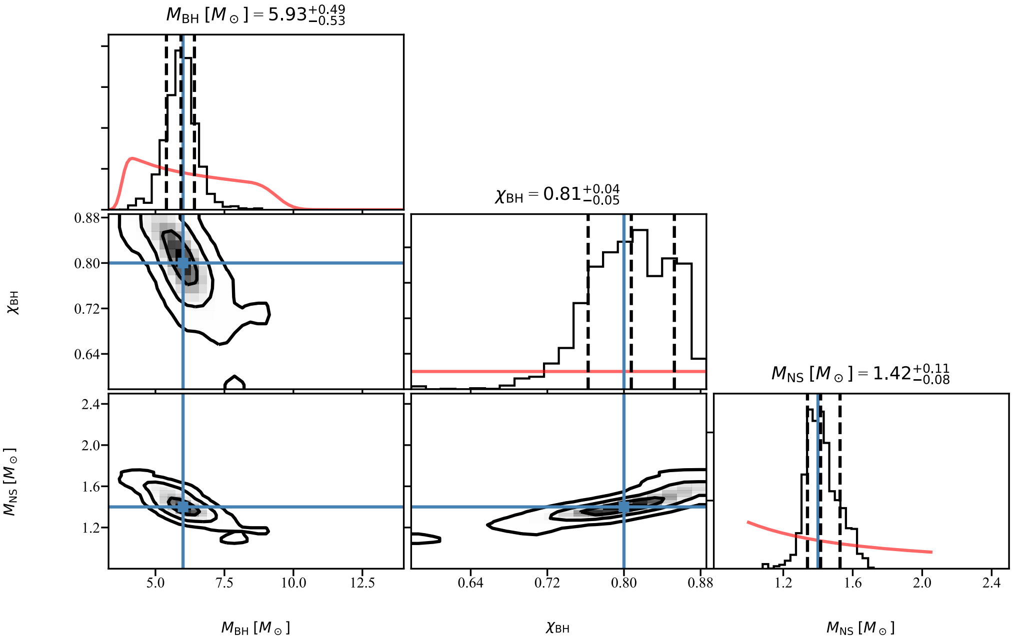

Fig. 6.11 Same as Fig. 6.9, considering as free parameters $M_{\rm BH}$, $\chi_{\rm BH}$, $M_{\rm NS}$ (fixing the EoS to SFHo).

binary system, where the inferred $M_{\rm BH} = 3.3^{+2.8}_{-0.7} M_\odot$, ideally falling in the mass gap.

In low-latency GW signal analysis, LVC use the inferred chirp mass value to classify the nature of the coalescing binary (information available in the GCNs). In particular, from $M_{\rm c}$ the possible ranges for M_1 and M_2 can be obtained (see Fig. 6.8). Systems with both component masses below $3M_\odot$ are classified as "BNS" (NSNS), those with both M_1 and M_2 above $5M_\odot$ as "BBH" (BHBH), those with $M_1 > 5M_\odot$ and $M_2 < 3M_\odot$ as "NSBH" and those with at least one component with mass $3 < M < 5M_\odot$ as "MassGap". Additionally the probability that the event is not of astrophysical origin (e.g. false trigger) is indicated as "Terrestrial". In this work I assume a partially different classification scheme. I consider the minimum mass of NSs $M_{\rm NS}^{\rm min} = 1M_\odot$ ($\sim 10\%$ less than the value indicated in Suwa et al. 2018). I classify as NSNS systems with both M_1 and M_2 between $1M_\odot$ and $M_{\rm NS}^{\rm max}$ (according to the considered EoS); BHNS systems with $M_1 \geq 5M_\odot$ and $M_2 \leq M_{\rm NS}^{\rm max}$; BHBH systems with both M_1 and M_2 above $5M_\odot$. Moreover I define "BH+gap" systems with $M_1 \geq 5M_\odot$ and $M_{\rm NS}^{\rm max} < M_2 < 5M_\odot$, "gap+NS" systems with $M_{\rm NS}^{\rm max} < M_1 < 5M_\odot$ and $M_2 \leq M_{\rm NS}^{\rm max}$, "gap+gap" systems with both M_1 and M_2 between $M_{\rm NS}^{\rm max}$ and $5M_\odot$. Considering that the "gap" is populated by compact objects, they have masses larger than $M_{\rm NS}^{\rm max}$, then I assume that they are low-mass stellar BHs. Therefore "gap+NS" systems are BHNS binaries, while "gap+gap" and "BH+gap' are BHBH binaries.

Considering SFHo EoS (consistent with NSNS GW signals and NICER results to date), the maximum NS mass is $\sim 2.05M_\odot$. Thus the maximum chirp mass for a NSNS system is $\sim 1.785M_\odot$. Assuming the existence of the mass gap, the minimum

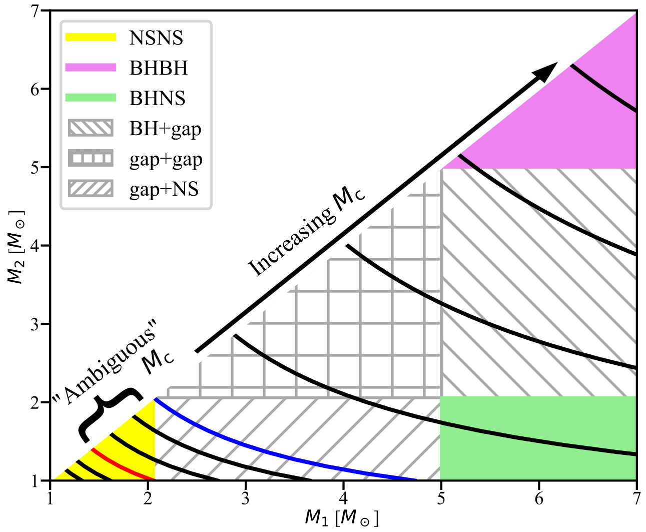

Fig. 6.12 Classification scheme for compact object binaries, assuming SFHo EoS $M_{\rm NS}^{\rm max} \sim 2.05 M_\odot$ and $M_{\rm NS}^{\rm min} = 1 M_\odot$. Solid lines indicate binary configurations consistent with several chirp mass values. Violet, green and yellow regions indicate, respectively, BHBH, BHNS and NSNS systems. Binaries with at least one component in the mass gap are indicated as gray-hatched regions. Red (blue) line indicates $M_{\rm c,amb}^{\rm min}$ ($M_{\rm c,amb}^{\rm max}$), see text for details.

chirp mass for a BHNS system is $\sim 1.835 M_\odot$ (configuration with $M_{\rm BH} = 5 M_\odot$ and $M_{\rm NS} = 1 M_\odot$). Thus no chirp mass value can be compatible both with NSNS and BHNS merger, assuming the existence of the mass gap.

Instead, assuming adjacent NS and BH mass distributions, there is a range of chirp mass values that are consistent with both NSNS and BHNS binaries (with the BH falling in the mass gap). In such a scenario, the nature of the merging system can not be identified only through the GW signal analysis (see i.e. Mandel et al. 2015). I define "ambiguous" the $M_{\rm c}$ values compatible with NSNS and BHNS binary natures. Fig. 6.12 has been produced considering SFHo EoS. The ambiguous chirp mass range for this EoS spans from $M_{\rm c,amb}^{\rm min} = 1.233 M_\odot$ (corresponding to $M_1 = M_{\rm NS}^{\rm max}$ and $M_2 = 1 M_\odot$, red line) and $M_{\rm c,amb}^{\rm max} = 1.792 M_\odot$ (corresponding to $M_1 = M_2 M_{\rm NS}^{\rm max}$, blue line). Indeed below $M_{\rm c,amb}^{\rm min}$ the system is certainly a NSNS binary, while above $M_{\rm c,amb}^{\rm max}$ the system can not be a NSNS binary.

Despite the system's nature being not discernable through the GW signal, the intrinsic binary properties affect the ejecta ones, that in turn determine the EM counterpart properties. Indeed in Barbieri et al. (2019b, 2020b) I showed that the observation of the kilonova associated with an "ambiguous" merger could help to identify the nature of the merging system.

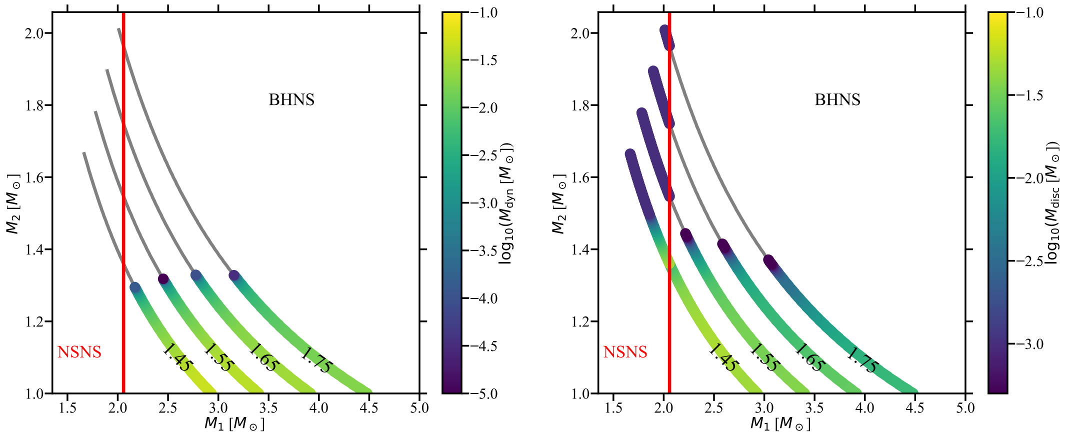

Fig. 6.13 Dynamical ejecta (left panel) and accretion disc (right panel) masses from NSNS/BHNS configurations compatible with "ambiguous" chirp masses (different lines with reported values). I assume $\chi_{\rm BH} = 0$ and SFHo EoS ($M_{\rm NS}^{\rm max} = 2.058 M_\odot$). The vertical red line separates BHNS systems (right) from NSNS ones (left).

6.2.2.2 Solving the ambiguity with kilonovae

Fig. 6.13 shows dynamical ejecta and accretion disc masses produced by different binary configurations consistent with several "ambiguous" chirp masses. It is evident that NSNS systems compatible with "ambiguous" $M_{\rm c}$ are expected to produce minimal accretion discs and no dynamical ejecta. The only exception is the case with low $M_{\rm c} = 1.45 M_\odot$, where massive accretion discs can be produced in binaries with sufficiently large mass ratios. Therefore "ambiguous" NSNS systems, being composed by massive stars, are the worst configurations for ejecta production. On the contrary, a large number of BHNS systems compatible with "ambiguous" $M_{\rm c}$ produce massive dynamical ejecta and accretion discs. Indeed "ambiguous" BHNS binaries have small mass ratios ($q < 5$) and low-mass (more deformable) NSs, corresponding to the optimal configuration for ejecta production.

The difference in the dynamical ejecta and accretion disc masses, together with the other different ejecta properties for the two kind of systems (see § 3.1), will produce significantly dissimilar kilonova emission. Fig. 6.14 shows the expected ranges of kilonova light curves from NSNS and BHNS mergers consistent with the considered "ambiguous" chirp masses. In particular I consider the g (509 nm) and K (2143 nm) bands, showing the absolute magnitude at different times. For $M_{\rm c} \geq 1.55 M_\odot$ no dynamical ejecta and minimal discs are produced for NSNS mergers (see Fig. 6.13). Thus dim kilonova emission is expected for these systems (peaking at ~ -14 mag in the g-band and ~ -12 mag in the K-band). The NSNS kilonova range for $M_{\rm c} = 1.45 M_\odot$ is shown in panels 1. Instead BHNS mergers produce a range of kilonova light curves for each "ambiguous" $M_{\rm c}$. For $M_{\rm c} \geq 1.55 M_\odot$ only BHNS systems can produce massive ejecta, thus the detection of a kilonova light curve would strongly favor this nature

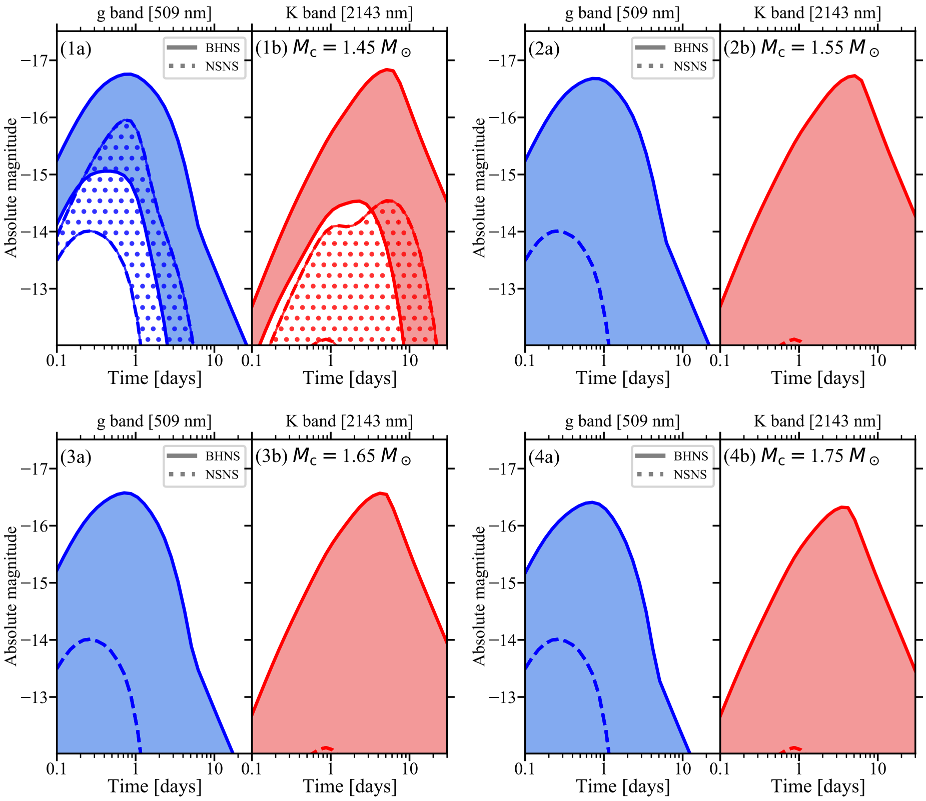

Fig. 6.14 Expected ranges of kilonova light curves from NSNS and BHNS mergers consistent with the considered "ambiguous" chirp masses (reported on panels "b"). I consider the g (509 nm, blue, panels "a") and K (2143 nm, red, panels "b") bands. Solid (dotted) filled regions indicate the BHNS (NSNS). Dashed lines in panels 2-3-4 indicate the NSNS KN when the disc mass is $10^{-3}M_\odot$. I assume SFHo EoS and non-spinning BHs.

for the merging system. Indeed there is only a small overlap of the corresponding dim kilonova (dotted lines in 6.14) with the BHNS light curves range. Thus for "ambiguous" $M_c \geq 1.55M_\odot$, except for the observation of a very dim emission, the kilonova detection would support a BHNS nature for the merging system. For $M_c = 1.45M_\odot$ all BHNS light curves are brighter than the NSNS ones at times $t \lesssim 7$ hours in the g-band and $t \lesssim 3$ days in the K-band. Moreover at times $t \gtrsim 1$ week in the g-band and $t \gtrsim 3$ weeks in the K-band the majority of BHNS light curves are brighter than the NSNS ones. Therefore the early/late time observation of the kilonova associated with an "ambiguous" system with such a chirp mass would distinguish the nature of the merging binary. At intermediate times there is an overlap of the BHNS/NSNS ranges. The kilonova observation at these times could unveil the nature of the coalescing system if it was very bright (BHNS) or very dim (NSNS).

BHNS kilonovae as luminous as or even brighter than NSNS ones were also presented in Kawaguchi et al. (2020). They found that in the K-band BHNS kilonovae are brighter (smaller ejecta Y_e due to the lack of strong neutrino irradiation from the remnant), while in the i-band the NSNS kilonovae from systems forming a supermassive NS are brighter (as in these cases the strong neutrino irradiation increases the ejecta Y_e). However they do not select NSNS/BHNS configurations corresponding to the same chirp mass. Fixing M_c reduces the NSNS configurations mainly to those producing low-mass ejecta, therefore the majority of BHNS kilonovae are brighter in each band. Other works on distinguishing the nature of the merging system are Hinderer et al. (2019), Coughlin and Dietrich (2019) (the authors considered a very low-mass BH of $\sim 1.4 M_\odot$, comparable to a NS).

It is important to stress that the BHNS kilonova ranges shown in Fig. 6.14 are obtained considering $\chi_\mathrm{BH} = 0$. As explained above, this is the worst configuration for ejecta production, corresponding to the dimmest light curves. Thus the capability to distinguish the nature of the merging system would be even larger for spinning BHs. As an example, assuming $\chi_\mathrm{BH} \lesssim 0.5$ all the BHNS kilonovae are much brighter that the NSNS ones.

Identifying the nature of an "ambiguous" system would give important information on the maximum NS mass $M_\mathrm{NS}^\mathrm{max}$ and (in case of a BHNS nature identification) discover the existence of low-mass stellar BHs (close to $M_\mathrm{NS}^\mathrm{max}$), confuting the existence of a "mass-gap" between $\sim 2 M_\odot$ and $\sim 5 M_\odot$. These results would also give fundamental constraints on the NS EoS.

6.2.2.3 Application to GW190425

In April 2019 the second GW signal consistent with a NSNS merger was detected by LVC (LVC 2020*c*). Very interestingly, the inferred chirp mass $M_\mathrm{c} = 1.44 \pm 0.02$ is exactly in the "ambiguous" range. Indeed, as LVC (2020*c*), Kyutoku et al. (2020), Han et al. (2020) indicated, the presence of a BH in the binary can not be excluded. In Barbieri et al. (2020b) I applied the study described above (§6.2.2.2) to the real GW190425 event.

Late in 2019, the Neutron Star Interior Composition Explorer (NICER) results provided new constraints on the EoS, by precise analysis of the millisecond pulsar PSRJ0030+0452 (Becker et al. 2000). In Barbieri et al. (2020b) I considered two EoS, namely "DD2" (Hempel and Schaffner-Bielich 2010, Typel et al. 2010) and "APR4" (Akmal et al. 1998, Read et al. 2009). These EoS are one of the stiffest and one of the softest, respectively, among those consistent with the NICER results (Miller et al. 2019a, Riley et al. 2019) and GW170817/GW190425 events (LVC 2019*e*, Kiuchi et al. 2019, Radice et al. 2018b, LVC 2020*c*). Fig. 6.15 shows the system configurations compatible with the GW190425 chirp mass. The dashed vertical lines indicate $M_\mathrm{NS}^\mathrm{max}$

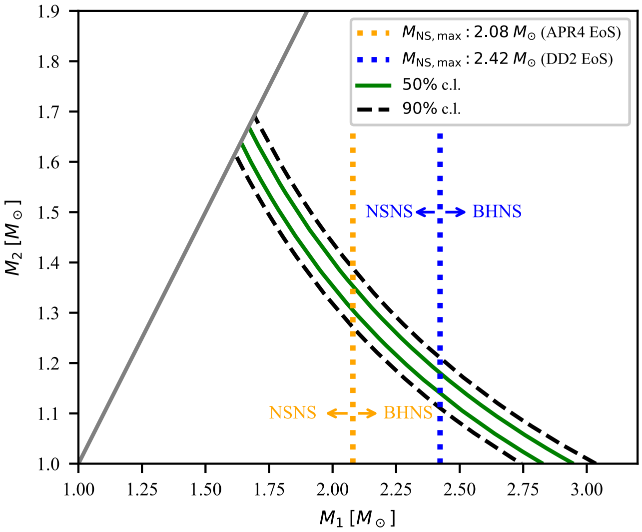

Fig. 6.15 Binary configurations consistent with $M_{\rm c} = 1.44 \pm 0.02 M_\odot$, the inferred chirp mass for GW190425. Green (black-dashed) lines indicate the 50% (90%) confidence regions. The dashed vertical lines indicate $M_{\rm NS}^{\rm max}$ for APR4 (orange) and DD2 (blue) EoS. Image from Barbieri et al. (2020b), copyright by the authors.

for APR4 (orange) and DD2 (blue) EoS. Binary configurations on the right of these lines are BHNS systems, while those on the left are NSNS systems.

Using the fitting formulae presented in §3.4, in Fig. 6.16 I show the dynamical ejecta and accretion disc masses for different NSNS/BHNS configurations consistent with the GW190425 $M_{\rm c}$. The primary's mass M_1 is shown on the upper x-axis and vertical dotted lines indicate $M_{\rm NS}^{\rm max}$ for APR4 and DD2 EoS. Therefore configurations on the left of these lines are BHNS binaries, while those on the right are NSNS. For BHNS mergers, I compute the upper and lower bound on ejecta masses considering, respectively, maximally-spinning BHs ($\chi_{\rm BH} = 0.99$, solid lines) and non-spinning BHs ($\chi_{\rm BH} = 0$, dot-dashed lines). I find that BHNS mergers with low-mass/large-$\Lambda_{\rm NS}$ NSs and small mass ratios produce massive ejecta (for both EoS and spin values). Instead NSNS mergers produce low-mass dynamical ejecta for DD2 EoS and no dynamical ejecta for APR4 EoS. Moreover, $\sim$ symmetric NSNS mergers produce low-mass accretion discs, while asymmetric NSNS mergers produce accretion discs with masses in between the non-spinning and maximally-spinning BHNS cases.

In Fig. 6.17 I show the NSNS/BHNS KN light curves ranges for binary configurations consistent with $M_{\rm c} = 1.44 M_\odot$. As above, I compute the upper and lower bound for BHNS systems considering, respectively, $\chi_{\rm BH} = 0.99$ and $\chi_{\rm BH} = 0$. For APR4 EoS, the NSNS KN ranges overlap with the BHNS ones in the low-luminosity region. However the majority of BHNS configurations produce KNae much brighter than the NSNS case (see also Fig. 6 and discussion in §4.1 in Barbieri et al. 2020b). The horizontal gray lines indicate the limiting magnitudes in the Zwicky Transient Facility (ZTF,

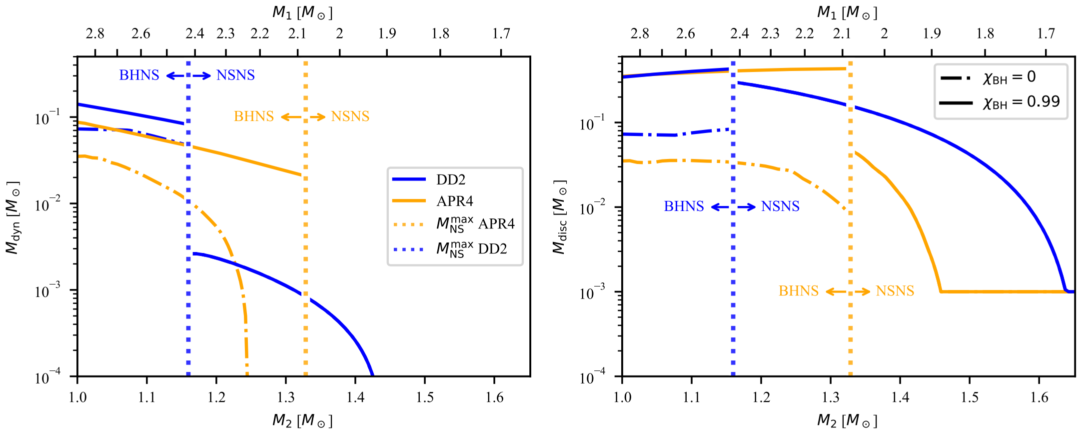

Fig. 6.16 Dynamical ejecta (left) and accretion disc (right) masses for different NSNS/BHNS configurations consistent with the inferred chirp mass for GW190425. I consider APR4 (orange) and DD2 (blue) EoS. The primary's mass M_1 is shown on the upper x-axis and vertical dotted lines indicate $M_{\rm NS}^{\rm max}$ for the considered EoS. Configurations on the left of these lines are BHNS binaries, while those on the right are NSNS. BHNS dot-dashed (solid) lines refer to non-spinning (maximally-spinning) BHs, representing the lower (upper) bound. Image from Barbieri et al. (2020b), copyright by the authors.

Bellm et al. 2019) EM follow-up of GW190425 (Coughlin et al. 2019c), in the g and r bands (assuming $d_{\rm L} = 161$ Mpc, LVC 2020c). For DD2 (APR4) EoS, all (the majority of) the BHNS configurations would have been detectable[4] in the first ~ 5 days. Also some NSNS configurations would have been detectable in the first days, even if with a dimmer emission.

Therefore, if the kilonova associated with GW190425 had been observed, the nature of the coalescing binary could have been unveiled.

6.2.3 Organisation of the EM follow-up campaign

As explained above, the nature of an "ambiguous" GW event can be unveiled if the associated kilonova is detected. The identification of the EM counterpart to a GW signal is not trivial. Indeed the low-latency GW analysis provides a localisation volume (combination of the sky localisation with the distance estimates) that can be very large. The GW source localisation depends on several factors (i.e. distance, masses, network configuration). For "ambiguous" systems, whose total mass is low compared to i.e. BHBH mergers, the sky localisation can be poorly informative. As an example, during O3 the mean 50% (90%) sky-localisation for NSNS candidates was ~ 2360 (8200) deg^2, while for BHNS candidates ~ 2090 (6860) deg^2. In case of a poorly informative localisation, thousands of galaxies and many more transients could be found in the

---

[4] Also Kyutoku et al. (2020) found that the kilonova from GW190425 would have been detectable if the system had hosted a BH.

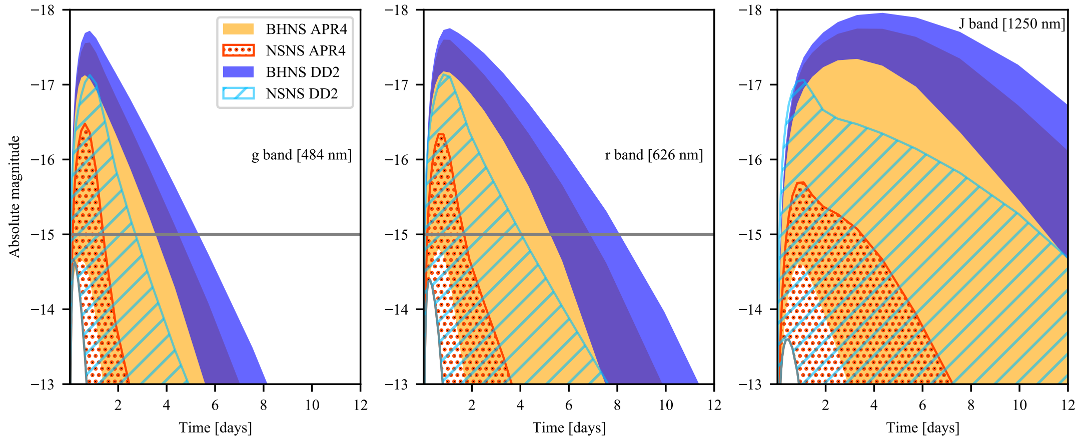

Fig. 6.17 Kilonova light curves ranges for NSNS/BHNS configurations consistent with the inferred chirp mass for GW190425. Upper (lower) bounds for BHNS KNae are computed assuming $\chi_{\rm BH} = 0.99$ (0). I show light curves in the g (484 nm), r (626 nm) and J (1250 nm) bands. Blue (orange) solid filled regions indicate the BHNS KNae ranges for DD2 (APR4) EoS. Light blue hatched (red dotted) regions indicate the NSNS KNae ranges for DD2 (APR4) EoS. Limiting magnitudes for the ZTF EM follow-up of GW190425 are shown as gray horizontal lines. Image from Barbieri et al. (2020b), copyright by the authors.

volume to be investigated. Therefore the identification of the EM counterparts to the GW signal would be very challenging. In the worst scenario, all the EM information is lost as no EM counterpart is detected. In the best scenario, the EM counterparts are identified at late times, and information on the rapidly decaying/short living transients is lost.

In the previous sections I showed that the low-latency GW analysis precisely estimates the system's chirp mass, with which the expected kilonova ranges can be computed. Here I discuss how this could be used to optimize the EM follow-up strategy, due to the limited available observing time and the huge amount of transients in the sky region of interest. If a transient is consistent with the expected KN range at its first detection, it could be prioritized for following photometric/spectroscopic follow-up (to classify its origin) with respect to transients that fall outside the expected range at their first detection. Adopting this criterion could increase the probability of identifying the EM counterpart of the GW signal.

In Barbieri et al. (2019b) I ideally apply this method to the GW190425 follow-up campaign. GW190425 signal was detected only by LIGO Livingston interferometer, with SNR 12.9 (LIGO Hanford was not in science mode, while Virgo interferometer did non contribute to the detection due to the low SNR). This represents one the reasons for the poorly informative source's sky localisation (90% credible area[5] $\sim$8300 deg^2, LVC 2020*c*). To date, the public alert from LVC includes the inferred distance, the

---

[5] As a comparison, GW170817 source was localised within a 90% credible area $\sim$ 28 deg^2.

binary classification (see §6.2.2.1) and the skymap. Despite the region to investigate was large, the Global Relay of Observatories Watching Transients Happen (GROWTH) network covered $\sim 21\%$ of the skymap (Coughlin et al. 2019c). In the first 2 days following the GW trigger, 15 candidates were particularly promising (Kasliwal et al. 2019, Anand et al. 2019). However, they were later all classified as supernovae (after 1-4 days of observations, see Fig. 3 in Coughlin et al. 2019c).

Fig. 6.18 shows how the previously presented criterion could have been applied to the EM follow-up of GW190425 event. I computed the expected KN ranges (apparent magnitude) using the distance estimates reported by LVC (LVC 2019*c*), namely $d_{\rm L} = 155{\pm}45$ Mpc, and assuming that also the inferred chirp mass $M_{\rm c} = 1.44{\pm}0.02 M_{\odot}$ had been released. I computed the upper (lower) bounds considering $d_{\rm L} = 110$ Mpc and $\chi_{\rm BH} = 0.99$ for BHNS case ($d_{\rm L} = 200$ Mpc and $\chi_{\rm BH} = 0$ for BHNS case). I considered APR4 and DD2 EoS. Fig. 6.18 also shows 4 promising candidates at their first detection by ZTF. Transients ZTF19aasckkq and ZTF19aarzaod are consistent with the expected kilonova ranges at their first detection. Thus they should have been monitored anyway to identify their nature. Instead ZTF19aasckwd and ZTF19aarykkb are inconsistent with the expected ranges at their first detection. Thus the observation of other candidates could have been prioritized. I stress that ZTF19aasckwd and ZTF19aarykkb transients can be confidently discarded as GW190425 counterparts. Indeed they are brighter than the kilonova produced by a system with the same chirp mass of the event and a maximally-spinning BH, located at the lower bound of the $d_{\rm L}$ 1σ interval, and assuming one of the stiffest EoS (DD2) compatible with presently available constraints.

This criterion can be extended to each NSNS and BHNS GW trigger, significantly increasing the probability of detecting the EM counterpart associated with these events. As already done for GW190425, in the remaining time to the next LVK observing run (and corresponding new detections) I will continue testing and applying the proposed method to progressively published O3 GW detections and associated EM follow-up campaigns. An addition to this method will be the implementation of SN-like light curves templates, in order to perform on-the-fly comparison between EM observations and KN/SN expected light curves. Another addition will be the extension of this method to the GRB prompt and afterglow, to calculate the expected fluxes in the gamma- and X-rays bands.

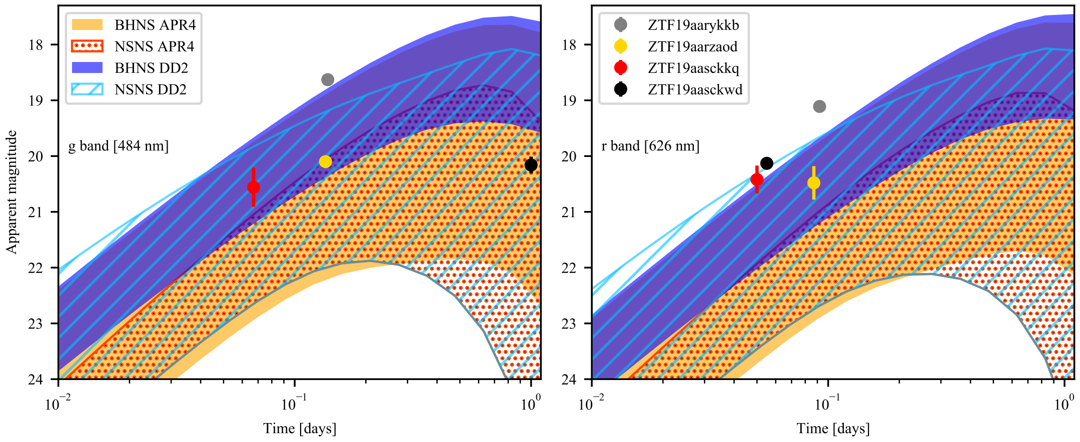

Fig. 6.18 Kilonova light curves ranges for NSNS/BHNS configurations consistent with the inferred chirp mass for GW190425. I consider the g (484 nm, left) and r (626 nm, right) bands. Blue (orange) solid filled regions indicate the BHNS KNae ranges for DD2 (APR4) EoS. Light blue hatched (red dotted) regions indicate the NSNS KNae ranges for DD2 (APR4) EoS. Upper (lower) bounds are obtained considering $d_{\rm L} = 110$ Mpc and $\chi_{\rm BH} = 0.99$ for BHNS case ($d_{\rm L} = 200$ Mpc and $\chi_{\rm BH} = 0$ for BHNS case). Points with errorbars represent the first ZTF detections of promising candidates as kilonova from GW190425. Image from Barbieri et al. (2020b), copyright by the authors.

6.3 NSNS/BHNS horizons and EM counterpart peak properties distribution

During the last LVC observing run O3 (concluded in March 2019 due to the COVID-19 emergency), several NSNS and BHNS merger candidates have been reported[6]. In particular, 5 (3) candidates were classified with probability $> 40\%$ (80%) as BHNS mergers, and 7 (2) as NSNS mergers.

Estimates on the BHNS and NSNS intrinsic merger rates from population synthesis models are, respectively, $6 \times 10^{-10} \lesssim \mathcal{R}_{\rm BHNS} \lesssim 10^{-6}$ Mpc^{-3} yr^{-1} and $3 \times 10^{-7} \lesssim \mathcal{R}_{\rm NSNS} \lesssim 4 \times 10^{-6}$ Mpc^{-3} yr^{-1} (LVC 2010, Coward et al. 2012, Petrillo et al. 2013, Fong et al. 2015, de Mink and Belczynski 2015, Dominik et al. 2015, Giacobbo and Mapelli 2018, Mapelli and Giacobbo 2018, Artale et al. 2019, see also Rastello et al. 2020 and references therein). Dominik et al. (2015) anticipated the expected detection rates in O3 as $0.04 \lesssim \mathcal{R}_{\rm BHNS,det} \lesssim 12$ yr^{-1} and $1.3 \lesssim \mathcal{R}_{\rm NSNS,det} \lesssim 6.9$ yr^{-1}.

In this section, based on binary population synthesis results in the literature, I analyse the EM counterparts properties of events that are detectable through GW signal. I focus on the kilonova and GRB afterglow, studying the peak time and magnitude distributions. This could provide an additional contribution to the EM follow-up strategy organisation of GW triggers. Moreover, for each merger in the binary population I

---

[6] LIGO/Virgo O3 Public Alerts webpage `https://gracedb.ligo.org/superevents/public/O3/`

compute the GW and EM signals, in order to calculate the detection rates and horizon distances for the considered populations in O3.

6.3.1 BHNS/NSNS populations and binary parameters distribution

I consider binary populations from the `Startrack` code (Belczynski et al. 2002, see `www.syntheticuniverse.org`) and from the `MOBSE` code (Giacobbo et al. 2018). From the former I select the "Optimistic Common Envelope" model, while from the latter I select the `CC15`α`5` model (see Dominik et al. 2012, 2013, Mapelli et al. 2019, for a complete description of considered models).

6.3.1.1 `Startrack` population

I adopt the BH and NS mass distributions of merging BHNS/NSNS binaries from Dominik et al. (2012) for two progenitor's metallicities, namely $Z = 0.02 \equiv Z_{\odot}$ and $Z = 0.002 \equiv Z_{\rm low}$. Distributions of BH/NS mass, $M_{\rm c}$ and q are shown in Figs. 6,7 and 9 in Dominik et al. (2012). For BHNS binaries with metallicity $Z_{\odot}$ the BH and NS masses cluster around $7.5M_{\odot}$ and $1.2M_{\odot}$, respectively. Instead for BHNS binaries with metallicity $Z_{\rm low}$ BHs and NSs have masses in the intervals $7M_{\odot} - 17M_{\odot}$ and $1.1M_{\odot} - 1.8M_{\odot}$, repectively. For NSNS binaries with metallicity $Z_{\odot}$, M_1 clusters around $1.3M_{\odot}$ and M_2 around $1.1M_{\odot}$. Instead for NSNS binaries with metallicity $Z_{\rm low}$, M_1 clusters around $1.3M_{\odot}$ and M_2 falls in the range $1.1 - 1.25M_{\odot}$.

I adopt the cumulative $\mathcal{R}_{\rm BHNS}$/$\mathcal{R}_{\rm NSNS}$ contributions for different metallicities from Dominik et al. (2013). In order to be consistent with the component masses distributions, I collected the contributions in two categories: those with $Z > 0.005$ form the $Z_{\odot}$ group, while those with $Z < 0.005$ form the $Z_{\rm low}$ group. I consider the "low-end" scenario for metallicity evolution (for description see Dominik et al. 2013). The total cumulative $\mathcal{R}_{\rm BHNS}$/$\mathcal{R}_{\rm NSNS}$ is the sum of all contributions (Fig. 7 in Dominik et al. 2013, see also gray lines in Fig. 6.21-6.20 in panels "a"). According to the considered model, in the local Universe ($z < 0.1$) the cumulative $\mathcal{R}_{\rm BHNS}(z < 0.1) \sim 6 - 7$ yr^{-1} and the cumulative $\mathcal{R}_{\rm NSNS}(z < 0.1) \sim 45$ yr^{-1}.

6.3.1.2 `MOBSE` population

I adopt the BH and NS mass distributions of merging BHNS/NSNS binaries from Mapelli et al. (2019). For BHNS binaries, BH and NS masses are mainly distributed in the range $5M_{\odot} - 9M_{\odot}$ and $1.4M_{\odot} - 1.9M_{\odot}$, respectively (see their Fig. 5). For NSNS binaries, M_1 and M_2 are mainly distributed in the range $1.1M_{\odot} - 1.3M_{\odot}$ and around $1.1M_{\odot}$, respectively (see their Fig. 8). I adopt the cumulative $\mathcal{R}_{\rm BHNS}$/$\mathcal{R}_{\rm NSNS}$ from Mapelli and Giacobbo (2018) (their Figs. 1-2, see also gray lines in Fig. 6.21-6.20 in panels "c"). According to the considered model, the cumulative $\mathcal{R}_{\rm BHNS}(z < 0.1) \sim 47$ yr^{-1} and the cumulative $\mathcal{R}_{\rm NSNS}(z < 0.1) \sim 227$ yr^{-1}.

6.3.1.3 $\chi_{\rm BH}$ distribution

I consider two distributions for $\chi_{\rm BH}$ in BHNS binaries. I assume that this parameter remains constant from the BH formation to the binary merger.

First I extend to BHs in BHNS binaries the inferred $\chi_{\rm BH}$ distribution from BHBH merger detections in O1 and O2, assuming that spins are preferentially aligned (LVC 2018*a*). This assumption requires that the majority of coalescing BHNS binaries are "isolated"[7] and that the components remain aligned during the system evolution. $\sim 90\%$ of BHs from this distribution ("LVC aligned" from now on) has $\chi_{\rm BH} \lesssim 0.6^{+0.24}_{-0.28}$ (see LVC 2018*a*).

The second $\chi_{\rm BH}$ distribution is derived using Eq. 2 in Arca Sedda and Benacquista (2019), that represents a fit from Belczynski et al. (2017) (combining different metallicities). Belczynski et al. (2017) indicate that massive stars lose an important fraction of their angular momentum due to significant mass loss via stellar wind. As a consequence, BHs with $M_{\rm BH} \gtrsim 20 - 30 M_\odot$ (final remnant of massive stars' evolution) have low spins. Instead lighter BHs have large spins (because their progenitors did not experience significant mass loss). From now on I define this distribution as "High spin".

Fig. 6.19 shows the two considered $\chi_{\rm BH}$ distributions. For "High spin" all BHs from the assumed populations have $0.75 \lesssim \chi_{\rm BH} \lesssim 1$, as they have masses $< 30 M_\odot$.

6.3.1.4 Other parameters

For BHNS systems I assume $\vec{S}_{\rm BH}$ to be aligned with the binary's total angular momentum $\vec{L}$, corresponding to non-precessing binaries ($\iota_{\rm tilt} = 0°$).

I assume SFHo EoS (Steiner et al. 2013), which is consistent with NS mass-radius measurements by NICER (Miller et al. 2019a, Riley et al. 2019), constraints from GWs (GW170817/GW190425, LVC 2019*e*, 2020*c*), nuclear theory and multi-messenger GW+EM observations (Landry et al. 2020, Capano et al. 2019, Dietrich et al. 2020).

For each binary I extract the viewing angle $\theta_{\rm v}$ from an uniform distribution in $\cos\theta_{\rm v}$ (peaking at "edge-on" orientation).

6.3.2 GW and EM signals

I compute the GW signal for each binary merger using the `pycbc` software (Nitz et al. 2019b), adoptig the `Taylor F2` waveform approximant[8]. $h_+(\nu)$ and $h_\times(\nu)$ are com-

---

[7] Ye et al. (2019) indicated that the dynamically formed binaries' contribution to the merger rate is negligible, supporting this assumption.

[8] `Taylor F2` is a very fast approximant for the inspiral phase, but it does not consider deformability and/or spin effects. I also tested more precise (and slower) approximants (i.e. `IMRPhenomD_NRTidal`)

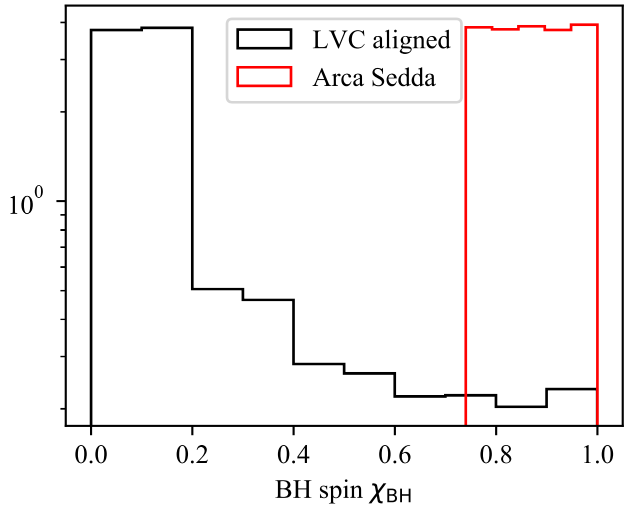

Fig. 6.19 Considered "High spin" (red) and "LVC aligned" (black) BH spin distributions.

puted giving M_1, M_2, $d_{\rm L}$ and $\theta_{\rm v}$. I consider the LVC detector network, composed by LIGO Livingston (L), LIGO Hanford (H) and Virgo (V) interferometers. The antenna pattern function $f(\alpha, \delta, \psi, t_{\rm merg})$ (where α is the source's right ascension, δ its declination, ψ the polarization angle and $t_{\rm merg}$ the merger time) for each detector is given is `pycbc`, together with the spectral strain sensitivity $S_{\rm noise}(\nu)$. The GW signal detected in each interferometer and the corresponding SNR are given by Eqs. 2.30 and 2.35, respectively. For a network detection, the total SNR is

$$\mathrm{SNR}^2_{\rm Net} = \sum_i \mathrm{SNR}^2_i, \tag{6.3}$$

with $SNR_{\rm i}$ the SNR in each detector. I consider that an event is "GW-detectable" if $SNR_{\rm Net} > 8$. Moreover for each event I assume a network configuration ("L+H+V", "L+H", "L+V", "H+V", "L", "H", "V", or no active detector), considering the O3 duty cycle. For each event I also average the SNR over different combinations of α, δ, ψ and $t_{\rm merg}$ parameters. In particular, α and ψ distributions are uniform in the $0 - 2\pi$ rad range, δ distribution is uniform in $\sin\delta$, and $t_{\rm merg}$ is uniformly extracted in the O3 period.

I compute the (possible) EM counterparts for each binary merger using the previously presented models. In particular I compute:

- KN light curves in the g (484 nm), r (626 nm) and J (1250 nm) bands from ~ 2 hours to 1 month, considering the limiting magnitudes of GW190425 follow-up

---

that includes these effects. However, despite producing significantly different waveforms, the estimated SNRs were very similar. Therefore, in order to reduce the computational time, I adopted `Taylor F2`.

GROWTH campaign (21 mag, 21 mag and 15.5 mag, respectively, Coughlin et al. 2019c);

- GRB afterglow light curves in the radio (1.4 GHz), optical (4.6×10^{14} Hz, 626 nm) and X bands (2.4×10^{17} Hz, 1 keV) from ~ 2 hours to 1 year, considering typical limiting fluxes of, respectively, 0.05 mJy, 5.7×10^{-3} mJy and 1.5×10^{-6} mJy;
- GRB prompt emission, considering Fermi-GBM limiting flux in the 10-1000 keV range, namely 1 phot cm^{-2} s^{-1}.

I do not consider kilonova radio remnant light curves as they peak at late times ($\sim$ years) with very low fluxes, with respect to the other counterparts (as explained in § 5.6, see also Barbieri et al. 2019a). Indeed all kilonova radio remnant light curves for the considered populations were not detectable in the simulated 1-year follow-up campaign.

In the following I define an event as “EM-detectable” if at least one of GRB prompt, KN, GRB afterglow is brighter than the limiting threshold in at least one of the considered bands. Moreover for the KN and GRB afterglow I require that the light curves are detectable for more than 1 day. In the same way, I define an event as “KN/GRB prompt/GRB afterglow-detectable” if the KN/GRB prompt/GRB afterglow is brighter than the limiting threshold in at least one of the considered bands. I stress that this is a simplification, as having the light curves above the limiting threshold is a necessary but not sufficient condition for detection. Indeed if the sky localisation from GW signal analysis is poorly informative the source’s location could be pointed at late times, when the emission has faded away, or even never pointed. Thus in the following when I refer to EM detections I assume that the GW signal analysis always precisely localises the source. Finally, I define an event as “GW+EM-detectable” if it is both EM-detectable and GW-detectable.

6.3.3 BHNS/NSNS mergers detection rates and horizons

In each redshift bin I generate 10^4 binaries. For each of them I assign an LVC interferometers network configuration and I calculate the probability of being GW-detectable and the possible GRB prompt, GRB afterglow and KN emission. Then for each of the X-channels (where X can be GW,KN,GRB afterglow, GRB prompt, GW+EM or EM) I calculate the detectable fraction of the generated binaries. Finally the contribution in each redshift bin to the X-channel detection rate is the product of the X-detectable events fraction by the intrinsic merger rate. The horizon distance for each channel is the one where the cumulative detection rate flattens (farther events are non detectable). In the following “local rate” indicates the cumulative merger rate for $z < 0.1$.

Fig. 6.20 (panels a-b) shows the results for `Startrack` BHNS population. The intrinsic cumulative merger rate is represented with a gray line. For this population I find that O3 GW horizon is $z \sim 0.3$ (corresponding to a distance $d_{\rm L} \sim 1.6$ Gpc) and the local GW detection rate is ~ 6 yr^{-1}, in agreement with expectations in LVC (2010) and the reported O3 BHNS candidates. For "High spin" $\chi_{\rm BH}$ distribution, the O3 KN horizon is $z \sim 0.1$ ($d_{\rm L} \sim 475$ Mpc) and the local KN detection rate is ~ 0.4 yr^{-1}. For "LVC aligned" $\chi_{\rm BH}$ distribution, the O3 KN horizon is $z \sim 0.09$ ($d_{\rm L} \sim 450$ Mpc) and the local KN detection rate is ~ 0.03 yr^{-1}.

Fig. 6.20 (panels c-d) shows the results for `MOBSE` BHNS population. The intrinsic cumulative merger rate is represented with a gray line. For this population I find that O3 GW horizon is $z \sim 0.28$ ($d_{\rm L} \sim 1.5$ Gpc) and the local GW detection rate is ~ 38 yr^{-1}, in agreement with expectations in LVC (2010) but not with the reported O3 BHNS candidates. For "High spin" $\chi_{\rm BH}$ distribution, the O3 KN horizon is $z \sim 0.09$ ($d_{\rm L} \sim 400$ Mpc) and the local KN detection rate is ~ 8 yr^{-1}. For "LVC aligned" $\chi_{\rm BH}$ distribution, the O3 KN horizon is $z \sim 0.09$ ($d_{\rm L} \sim 400$ Mpc) and the local KN detection rate is < 1 yr^{-1}.

Fig. 6.21 (panels a-b) shows the results for `Startrack` NSNS population. The intrinsic cumulative merger rate is represented with a gray line. For this population I find that O3 GW horizon is $z \sim 0.15$ (corresponding to a distance $d_{\rm L} \sim 736$ Mpc) and the local GW detection rate is ~ 12 yr^{-1}, in agreement with expectations in LVC (2010) and about twice the reported O3 NSNS candidates. The O3 KN horizon is $z \sim 0.06$ ($d_{\rm L} \sim 278$ Mpc) and the local KN detection rate is ~ 5 yr^{-1}.

Fig. 6.21 (panels c-d) shows the results for `MOBSE` NSNS population. The intrinsic cumulative merger rate is represented with a gray line. For this population I find that O3 GW horizon is $z \sim 0.13$ (corresponding to a distance $d_{\rm L} \sim 630$ Mpc) and the local GW detection rate is ~ 52 yr^{-1}, in agreement with expectations in LVC (2010) but not with the reported O3 NSNS candidates. The O3 KN horizon is $z \sim 0.065$ ($d_{\rm L} \sim 302$ Mpc) and the local KN detection rate is ~ 31 yr^{-1}.

Horizons and local detection rates from Figs. 6.20 and 6.21 are summarised in, respectively, Tables 6.2-6.3 and Tables 6.4-6.5. As mentioned above, BHNS (NSNS) estimated local GW detection rates for `Startrack` population are (almost) consistent with reported O3 candidates, while for `MOBSE` population I find large overestimates. This could indicate that the component masses distributions and/or the intrinsic merger rates from `Startrack` population are more likely. During O3 EM follow-up campaigns identified no counterparts associated with any of the BHNS/NSNS candidates. As already mentioned, the EM detection rates reported in this work are overestimations, because I assume each source to be precisely localised by the GW signal analysis. In reality during O3 the mean sky-area 50% (90%) confidence region for BHNS candidates has been ~ 2090 (~ 6860) deg^2, while for NSNS candidates ~ 2360 (~ 8200) deg^2.

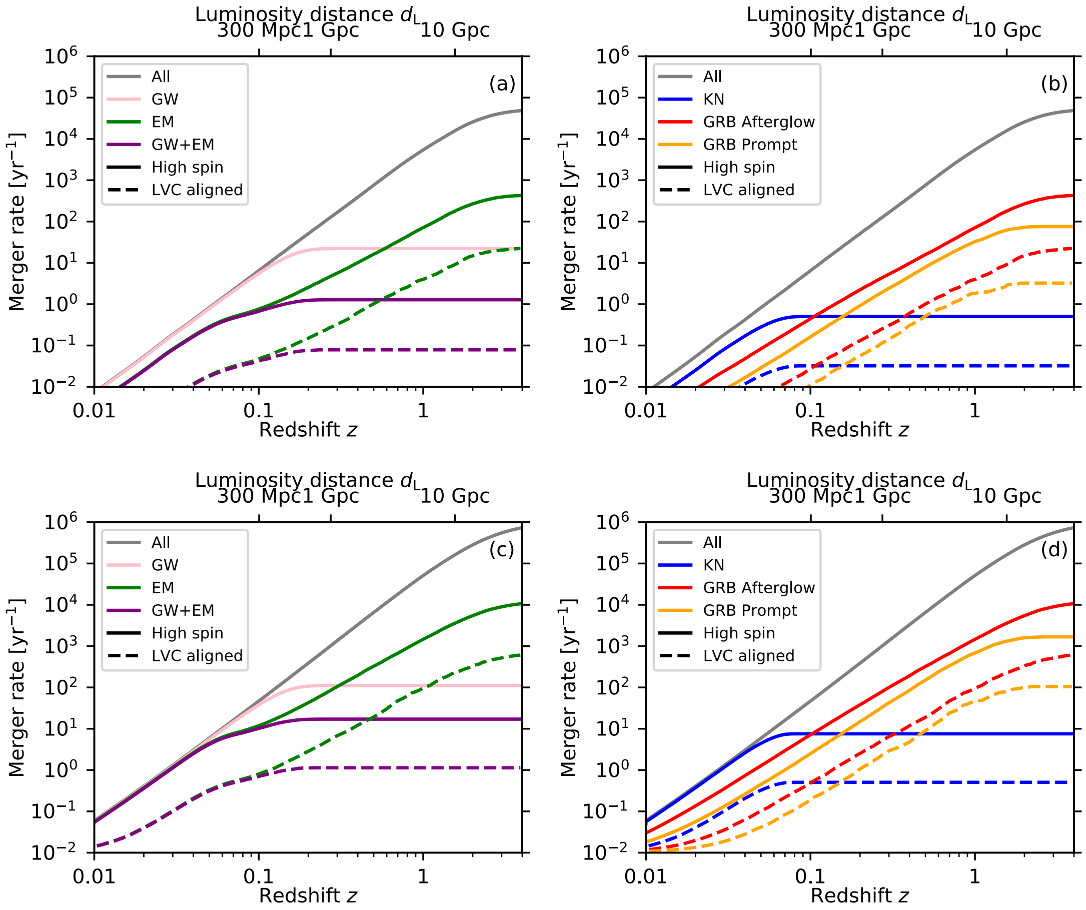

Fig. 6.20 Cumulative BHNS merger rate $R(< z)$ for the `Startrack` (panels a-b) and `MOBSE` (panels c-d) population. Gray lines indicate the intrinsic R. Filled and dashed lines are obtained using, respectively, "High-spin" and "LVC aligned" spin distribution. *Left column* – Pink lines indicate the GW-detectable R, green lines the EM-detectable R and purple lines the GW+EM-detectable R. *Right column* – Blue lines indicate the KN-detectable R, red lines the GRB Afterglow-detectable R and orange lines the GRB Prompt-detectable R.

Channel	`Startrack` population - BHNS			
	High Spin		LVC aligned	
	Horizon [Mpc]	Local detection [yr^{-1}]	Horizon [Mpc]	Local detection [yr^{-1}]
GW	1.6×10^3 ($z\sim0.3$)	6	1.6×10^3 ($z\sim0.3$)	6
EM	$z>4$	<1	$z>4$	$\ll1$
GW+EM	1.6×10^3 ($z\sim0.3$)	<1	1.2×10^3 ($z\sim0.23$)	$\ll1$
KN	475 ($z\sim0.1$)	<1	450 ($z\sim0.09$)	$\ll1$
GRB Afterglow	$z>4$	<1	$z>4$	$\ll1$
GRB Prompt	22×10^3 ($z\sim2.6$)	<1	15×10^3 ($z\sim1.9$)	$\ll1$

Table 6.2 Horizon distances and local ($z < 0.1$) detection rates in the different channels for the `Startrack` BHNS population and the two BH spin distributions.

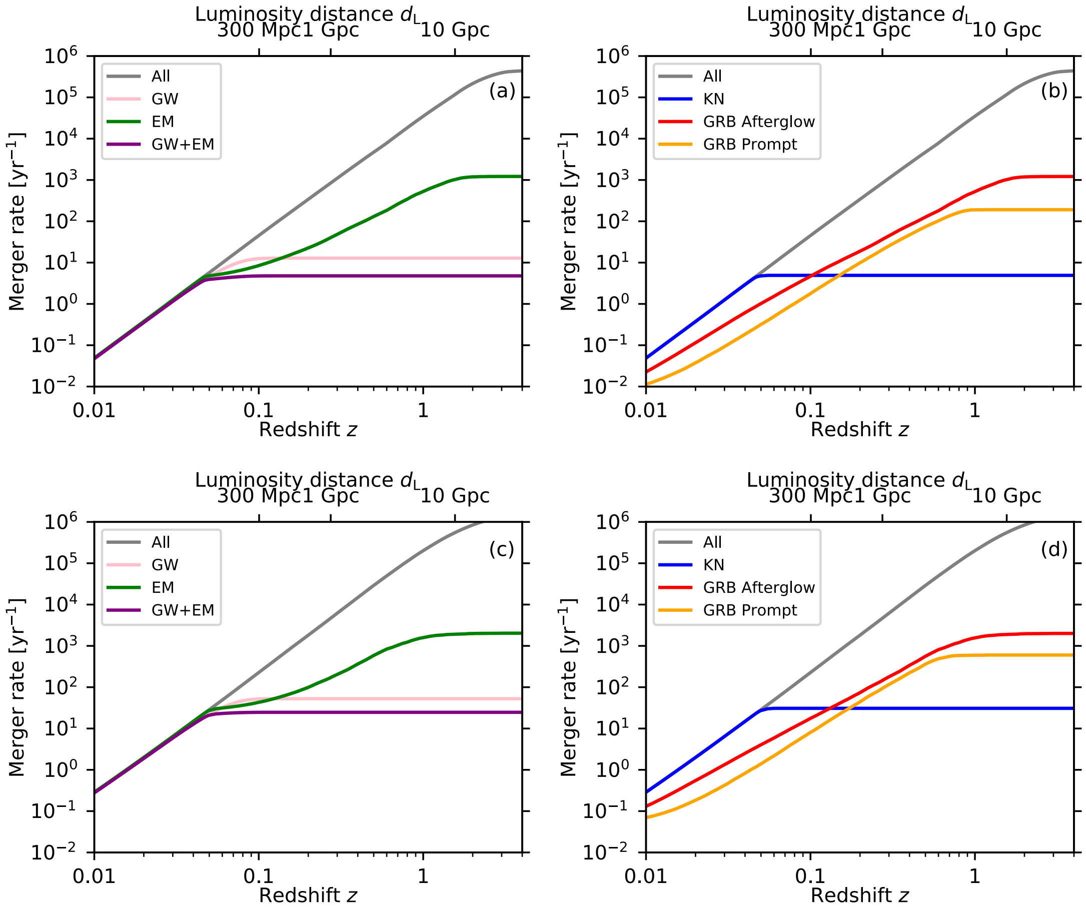

Fig. 6.21 Cumulative NSNS merger rate $R(<z)$ for the `Startrack` (panels a-b) and `MOBSE` (panels c-d) population. Gray lines indicate the intrinsic R. *Left column* – Pink lines indicate the GW-detectable R, green lines the EM-detectable R and purple lines the GW+EM-detectable R. *Right column* – Blue lines indicate the KN-detectable R, red lines the GRB Afterglow-detectable R and orange lines the GRB Prompt-detectable R.

Channel	`MOBSE` population - BHNS			
	High spin		LVC aligned	
	Horizon [Mpc]	Local detection [yr^{-1}]	Horizon [Mpc]	Local detection [yr^{-1}]
GW	$1.5{\times}10^3$ ($z\sim0.28$)	38	$1.5{\times}10^3$ ($z\sim0.28$)	38
EM	$z>4$	12	$z>4$	<1
GW+EM	$1.3{\times}10^3$ ($z\sim0.25$)	10	$1.1{\times}10^3$ ($z\sim0.22$)	<1
KN	400 ($z\sim0.09$)	8	400 ($z\sim0.09$)	<1
GRB Afterglow	$z>4$	7	$z>4$	<1
GRB Prompt	$23{\times}10^3$ ($z\sim2.7$)	3	$18{\times}10^3$ ($z\sim2.2$)	<1

Table 6.3 Same as Table 6.2, for the `MOBSE` BHNS population.

Channel	`Startrack` population - NSNS	
	Horizon [Mpc]	Local detection [yr^{-1}]
GW	736 ($z \sim 0.15$)	12
EM	36×10^3 ($z \sim 3.9$)	8
GW+EM	656 ($z \sim 0.13$)	5
KN	278 ($z \sim 0.06$)	5
GRB Afterglow	36×10^3 ($z \sim 3.9$)	5
GRB Prompt	8.5×10^3 ($z \sim 1.2$)	2

Table 6.4 Horizon distances and local ($z < 0.1$) detection rates in the different channels for the `Startrack` NSNS population.

Channel	`MOBSE` population - NSNS	
	Horizon [Mpc]	Local detection [yr^{-1}]
GW	630 ($z \sim 0.13$)	52
EM	26 × 10^3 ($z \sim 3$)	43
GW+EM	552 ($z \sim 0.11$)	25
KN	302 ($z \sim 0.065$)	31
GRB Afterglow	26×10^3 ($z \sim 3$)	18
GRB Prompt	8.5×10^3 ($z \sim 1.2$)	8

Table 6.5 Same as Table 6.4, for the `MOBSE` NSNS population.

It is important to note that I find GRB prompt and afterglow emission to be detectable also at $z > 1$, consistent with the farthest sGRBs observed to date (Zhang and Wang 2018). Thus, as proposed in Gompertz et al. (2018), Rossi et al. (2019) (and references therein), NSNS and/or BHNS mergers could be the progenitor of some of the observed sGRBs. Being these events very distant, the merger's GW signal is not detectable, making the interpretation of the progenitors more challenging.

6.3.4 EM counterparts peak properties distribution of GW-detectable BHNS/NSNS mergers

Among the simulated event, I select the GW-detectable ones that produce EM counterparts, in order to study the distribution of their peak properties (time and magnitude/flux).

Fig. 6.22 represents BHNS mergers. Here I show only the results for the "High spin" $\chi_{\rm BH}$ distribution. The results for "LVC aligned" distribution are similar, presenting only a small shift towards earlier times and dimmer peaks. Indeed for "LVC aligned" distribution a larger number of binaries produce low-mass ejecta, having smaller $\chi_{\rm BH}$. The `Startrack` population's results are shown in panels a-b. The KN peak time and absolute magnitude 50% and 90% intervals are shown in panel a. Panel b shows the 50% and 90% intervals for the GRB afterglow peak time and $\nu d\mathcal{L}/d\nu$, where

$$d\mathcal{L}/d\nu = \frac{4\pi d_{\rm L}^2}{1+z} F(\nu), \tag{6.4}$$

and ν is the observed frequency. It is important to remind that the observed GRB afterglow light curve is significantly affected by the viewing angle (see § 5.5). As explained above, I assume this parameter to be uniformly distributed in $\cos\theta_{\rm v}$ (predominantly off-axis cases). However, since "face-on" binaries produce a larger SNR and I am considering here GW-detectable events, the ratio of on-axis to off-axis binary number is slightly increased. Indeed I find the majority of GRB afterglow light curves to peak at late times ($\sim$ 10 days to $\sim$ 1 year), but there is also a non-negligible sub-group that peaks at early times[9] ($\sim$ hours) with bright emission, corresponding to the almost face-on events. The KN peaks have absolute magnitude in the range $-14 \lesssim M \lesssim -17.5$ and times $2 \lesssim t \lesssim 24$ hours in the g band, $8 \lesssim t \lesssim 40$ hours in the r band and 12 hours $\lesssim t \lesssim 10$ days in the J band.

The `MOBSE` population's results are shown in panels c-d. The KN peak time and absolute magnitude 50% and 90% intervals are shown in panel c. Panel d shows the 50% and 90% intervals for the GRB afterglow peak time and $\nu d\mathcal{L}/d\nu$. The KN peaks have absolute magnitude in the range $-15 \lesssim M \lesssim -17.5$ and times $2 \lesssim t \lesssim 24$ hours in the g band, $8 \lesssim t \lesssim 40$ hours in the r band and $1 \lesssim t \lesssim 10$ days in the J band.

Fig. 6.23 represents NSNS mergers. The `Startrack` population's results are shown in panels a-b. The KN peak time and absolute magnitude 50% and 90% intervals are shown in panel a. Panel b shows the 50% and 90% intervals for the GRB afterglow peak time and $\nu d\mathcal{L}/d\nu$. The KN peaks have times in the range 8 hours $\lesssim t \lesssim$ 3 days and absolute magnitude $-15.5 \lesssim M \lesssim -17$ in the g and r bands, and $-15.3 \lesssim M \lesssim -16.5$ in the J band.

The `MOBSE` population's results are shown in panels c-d. The KN peak time and absolute magnitude 50% and 90% intervals are shown in panel c. Panel d shows the 50% and 90% intervals for the GRB afterglow peak time and $\nu d\mathcal{L}/d\nu$. The KN peaks have times in the range 8 hours $\lesssim t \lesssim$ 3 days and absolute magnitude $-16 \lesssim M \lesssim -17$ in the g and r bands, and $-15.5 \lesssim M \lesssim -16.5$ in the J band.

Figs. 6.22 and 6.23 show that the kilonova peak properties distribution is quite narrow. Thus this analysis could provide stringent criteria to prioritize kilonova candidates observations, based on the expected luminosity/time range. If some constraints on the viewing angle are obtained from the GW signal analysis and/or the possible detection of a sGRB (see i.e. Iyyani and Sharma 2020), information from Figs. 6.22 and 6.23 can also guide the GRB afterglow search. The extension and systematic application of

---

[9] except for radio light curves. Indeed in this band also on-axis observers see the peaks at $t \geq 10$ days (see § 5.5, Fig. 5.7).

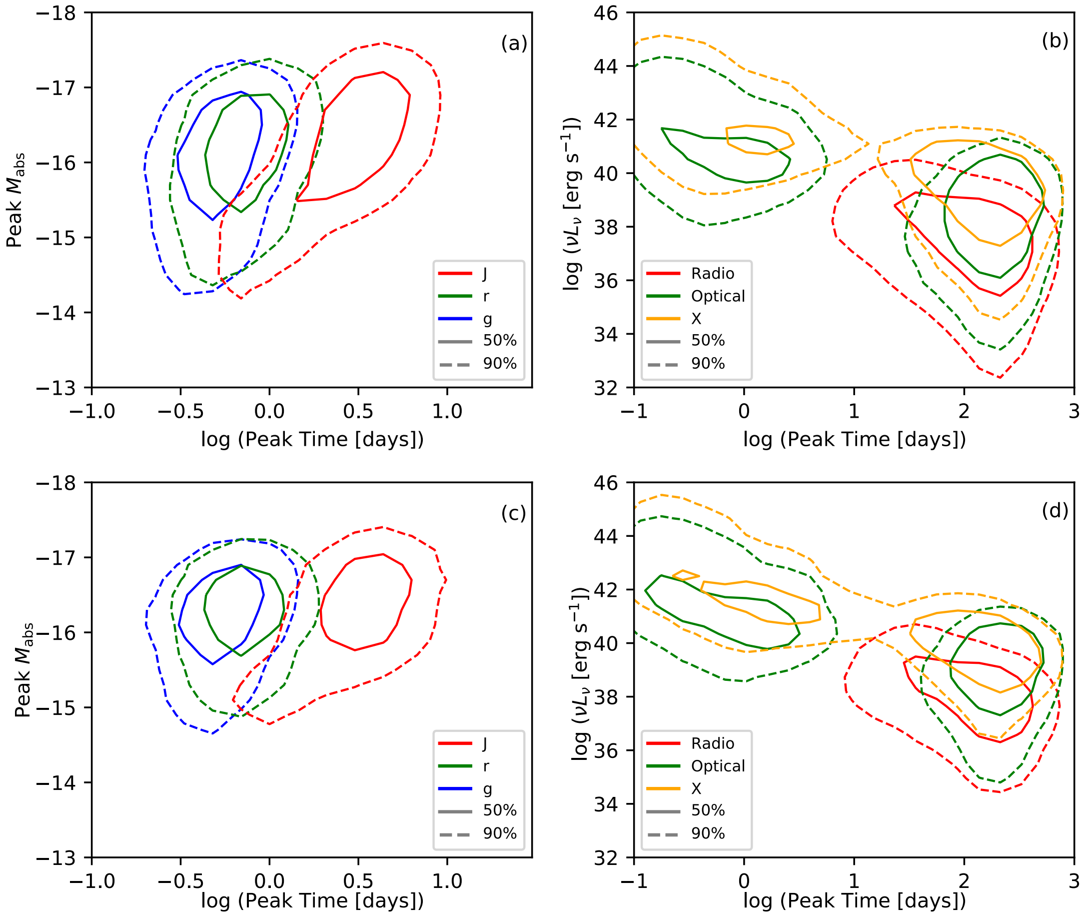

Fig. 6.22 EM counterparts peak properties distributions for GW-detectable BHNS mergers, from the `Startrack` (panels a-b) and `MOBSE` (panels c-d) population. I show the 50% (filled) and 90% (dashed) intervals, for the "High spin" BH spin distribution. *Left column* – Kilonova peaks absolute magnitude and time distribution, in the g (blue), r (green) and J (red) bands. *Right column* – GRB Afterglow peaks $\nu\ d\mathcal{L}/d\nu$ and time distribution, in the radio (red), optical (green) and X (orange) bands.

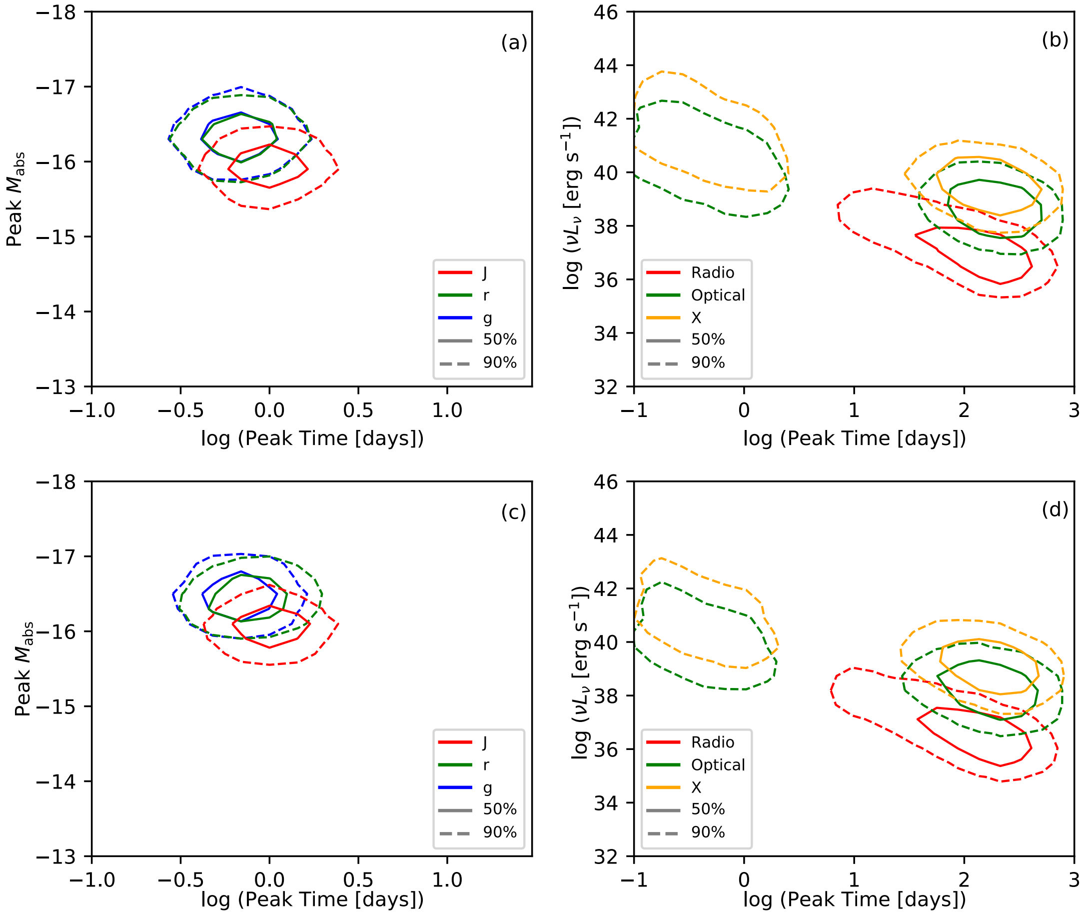

Fig. 6.23 EM counterparts peak properties distributions for GW-detectable NSNS mergers, from the `Startrack` (panels a-b) and `MOBSE` (panels c-d) population. I show the 50% (filled) and 90% (dashed) intervals. Stars indicate the peak properties of kilonova and GRB afterglow associated with GW170817. *Left column* – Kilonova peaks absolute magnitude and time distribution, in the g (blue), r (green) and J (red) bands. *Right column* – GRB Afterglow peaks $\nu\ d\mathcal{L}/d\nu$ and time distribution, in the radio (red), optical (green) and X (orange) bands.

this analysis to the future O4 observing run would be very important to characterize the expected EM counterparts' properties and to schedule the follow-up observations to maximize the probability of new multi-messenger detections (Barbieri et al. 2020c).

Conclusions

This work falls within the context of the nascent multi-messenger astronomy, where detections of gravitational waves and electromagnetic signals are combined together to increase the amount of available information. In particular, I studied the EM counterparts associated with BHNS and NSNS mergers.

I developed/updated emission models for all the expected EM counterparts (the kilonova and its radio remnant, the GRB prompt and GRB afteglow), based on results of recent state-of-the-art numerical simulations of BHNS/NSNS mergers.

Using these models, I anticipated the variety of light curves that can emerge from a BHNS merger. I showed how a combined GW+EM analysis could reduce the expected degeneracy and that a multi-messenger parameter estimation could give unprecedented constraints on the binary components (i.e. the NS tidal deformability and the BH spin).

This information would pose important constraints on the NS EoS and stellar BHs properties, besides giving insights on the compact object binaries formation and evolution history. As an example, if the BH spin is found to be almost aligned with the total orbital angular momentum L, the system is most likely a "field" binary (originated from the evolution of an isolated binary), and the BH spin can give insights on the stellar collapse (angular momentum transport, stellar winds). If instead the BH spin is not aligned with L, the system is a "dynamically-formed" binary, and the BH spin could indicate if it is a "second generation" BH (formed by the collapse of compact object) or a stellar BH.

I studied the particular case of coalescing binaries with "ambiguous" chirp mass, compatible with being both NSNS and BHNS (with low-mass BH, in the "mass-gap"). I showed that, while GW detection can not firmly identify the system's nature, the KN emission can be very different for the two cases. Thus the detection of this counterpart from an "ambiguous" event would be crucial to disentangle the system's nature.

I analyzed the real GW190425 event (whose chirp mass falls in the "ambiguous" range), proposing a method that, based on the knowledge of the system's chirp mass, could allow to distinguish the NSNS case from the BHNS one with the KN observation.

A firm identification of a "light" stellar BH, confuting the existence of a mass-gap between NS and BH mass distributions, would give crucial constraints on the maximum NS mass and it would be of paramount importance for supernova explosion models. Indeed to date two engine models are proposed: the "rapid" explosion, producing the mass-gap, and the “delayed” explosion (with longer timescales and significant fallback), producing a continuum mass spectrum for remnants.

Moreover I proposed new criteria to guide the organization of EM follow-up of GW triggers, with the aim of maximizing the EM counterpart detection probability. Indeed in the next LIGO/Virgo/KAGRA collaboration observing run O4 a large number of NSNS/BHNS events is expected to be detected through GWs, but the discovery and study of associated EM counterparts could be very challenging. Using the models presented in this work and by exploiting the posterior parameter distribution inferred from the analysis of the GW signal, the compound of the expected multi-wavelength light curves can be computed self-consistently. This precious information can be used both to schedule the observations in different bands and to prioritize the follow-up of transients consistent with the expected brightness at their first detection.

I applied the proposed method to KN candidates from GW190425 EM follow-up. I showed that some of them could have been immediately discarded, giving the possibility to observe other transients consistent with the expected luminosity range, thus increasing the detection probability of the GW190425 EM counterpart.

Finally, using the aforementioned models I simulated an LVC observing run to obtain the EM counterpart properties distribution for GW-detected events. By assuming a NSNS/BHNS population model (from population synthesis works in the literature), I simulated several events, computing both the GW signal and the EM counterparts (if any). Assuming observing scenarios for GWs (LVC network configurations and detector sensitivities) and EM signals (limiting magnitudes/fluxes at different wavelengths), I selected the events detectable in GWs obtaining the corresponding peak properties distributions. With this information, EM follow-up can be scheduled in order to make the most of telescopes’ availability by observing in each band at the optimal time for the detection (around the peak time). The extension and systematic application of this analysis to the future O4 observing run would be very important to characterize the expected EM counterparts’ properties and to maximize the probability of new multi-messenger detections.

REFERENCES

Ackley, K., Amati, L., Barbieri, C., Bauer, F. E., Benetti, S., Bernardini, M. G. and others (2020), ‘Observational constraints on the optical and near-infrared emission from the neutron star-black hole binary merger S190814bv’, *arXiv e-prints* p. arXiv:2002.01950.

Akmal, A., Pandharipande, V. R. and Ravenhall, D. G. (1998), ‘Equation of state of nucleon matter and neutron star structure’, *Phys. Rev. C* **58**(3), 1804–1828.

Alexander, K. D., Berger, E., Fong, W., Williams, P. K. G., Guidorzi, C., Margutti, R. and others (2017), ‘The Electromagnetic Counterpart of the Binary Neutron Star Merger LIGO/Virgo GW170817. VI. Radio Constraints on a Relativistic Jet and Predictions for Late-time Emission from the Kilonova Ejecta’, *ApJL* **848**(2), L21.

Anand, S., Kasliwal, M. M., Coughlin, M. W., Bellm, E. C., Ahumada, T., Perley, D. A. and Bhalerao, V. (2019), *Gamma-ray Coordinates Network Circulars* **24311**.

Arca Sedda, M. and Benacquista, M. (2019), ‘Using final black hole spins and masses to infer the formation history of the observed population of gravitational wave sources’, *MNRAS* **482**(3), 2991–3010.

Arcavi, I., McCully, C., Hosseinzadeh, G., Howell, D. A., Vasylyev, S., Poznanski, D., Zaltzman, M., Maoz, D., Singer, L., Valenti, S., Kasen, D., Barnes, J., Piran, T. and Fong, W.-f. (2017), ‘Optical Follow-up of Gravitational-wave Events with Las Cumbres Observatory’, *ApJL* **848**(2), L33.

Arcones, A., Janka, H. T. and Scheck, L. (2007), ‘Nucleosynthesis-relevant conditions in neutrino-driven supernova outflows. I. Spherically symmetric hydrodynamic simulations’, *AandA* **467**(3), 1227–1248.

Artale, M. C., Mapelli, M., Giacobbo, N., Sabha, N. B., Spera, M., Santoliquido, F. and Bressan, A. (2019), ‘Host galaxies of merging compact objects: mass, star formation rate, metallicity, and colours’, *MNRAS* **487**(2), 1675–1688.

Barbieri, C., Salafia, O. S., Colpi, M., Ghirlanda, G. and Perego, A. (2020b), ‘The kilonova of GW190425-like events’, *arXiv e-prints* p. arXiv:2002.09395.

Barbieri, C., Salafia, O. S., Colpi, M., Ghirlanda, G., Perego, A. and Colombo, A. (2019b), ‘Filling the Mass Gap: How Kilonova Observations Can Unveil the Nature of the Compact Object Merging with the Neutron Star’, *ApJL* **887**(2), L35.

Barbieri, C., Salafia, O. S., Perego, A., Colpi, M. and Ghirlanda, G. (2019a), ‘Light-curve models of black hole - neutron star mergers: steps towards a multi-messenger parameter estimation’, *AandA* **625**, A152.

Barbieri, C., Salafia, O. S., Perego, A., Colpi, M. and Ghirlanda, G. (2020a), ‘Electromagnetic counterparts of black hole-neutron star mergers: dependence on the neutron star properties’, *European Physical Journal A* **56**(1), 8.

Barbieri et al. (2020c), ‘’, *in preparation* .

Barnes, J. and Kasen, D. (2013), ‘Effect of a High Opacity on the Light Curves of Radioactively Powered Transients from Compact Object Mergers’, *ApJ* **775**, 18.

Baumgarte, T. W., Shapiro, S. L. and Shibata, M. (2000), ‘On the Maximum Mass of Differentially Rotating Neutron Stars’, *ApJL* **528**(1), L29–L32.

Bauswein, A., Baumgarte, T. W. and Janka, H. T. (2013), ‘Prompt Merger Collapse and the Maximum Mass of Neutron Stars’, *Phys. Rev. Let.* **111**(13), 131101.

Becker, W., Trümper, J., Lommen, A. N. and Backer, D. C. (2000), ‘X-Rays from the Nearby Solitary Millisecond Pulsar PSR J0030+0451: The Final ROSAT Observations’, *ApJ* **545**(2), 1015–1019.

Belczynski, K., Kalogera, V. and Bulik, T. (2002), ‘A Comprehensive Study of Binary Compact Objects as Gravitational Wave Sources: Evolutionary Channels, Rates, and Physical Properties’, *ApJ* **572**, 407–431.

Belczynski, K., Klencki, J., Meynet, G., Fryer, C. L., Brown, D. A., Chruslinska, M., Gladysz, W., O’Shaughnessy, R., Bulik, T., Berti, E., Holz, D. E., Gerosa, D., Giersz, M., Ekstrom, S., Georgy, C., Askar, A., Wysocki, D. and Lasota, J. P. (2017), ‘The origin of low spin of black holes in LIGO/Virgo mergers’, *arXiv e-prints* p. arXiv:1706.07053.

Belczynski, K., Wiktorowicz, G., Fryer, C. L., Holz, D. E. and Kalogera, V. (2012), ‘Missing Black Holes Unveil the Supernova Explosion Mechanism’, *ApJ* **757**(1), 91.

Bellm, E. C., Kulkarni, S. R., Graham, M. J., Dekany, R., Smith, R. M., Riddle, R. and others (2019), ‘The Zwicky Transient Facility: System Overview, Performance, and First Results’, *Publications of the Astronomical Society of the Pacific* **131**(995), 018002.

Beniamini, P., Nava, L. and Piran, T. (2016), ‘A revised analysis of gamma-ray bursts’ prompt efficiencies’, *MNRAS* **461**, 51–59.

Beniamini, P. and van der Horst, A. J. (2017), ‘Electrons’ energy in GRB afterglows implied by radio peaks’, *MNRAS* **472**, 3161–3168.

Bernuzzi, S., Breschi, M., Daszuta, B., Endrizzi, A., Logoteta, D., Nedora, V., Perego, A., Schianchi, F., Radice, D., Zappa, F., Bombaci, I. and Ortiz, N. (2020), ‘Accretion-induced prompt black hole formation in asymmetric neutron star mergers, dynamical ejecta and kilonova signals’, *arXiv e-prints* p. arXiv:2003.06015.

Bildsten, L. and Cutler, C. (1992), ‘Tidal Interactions of Inspiraling Compact Binaries’, *ApJ* **400**, 175.

Bishop, N. T. and Rezzolla, L. (2016), ‘Extraction of gravitational waves in numerical relativity’, *Living Reviews in Relativity* **19**(1), 2.

Blanchet, L. (2014), ‘Gravitational Radiation from Post-Newtonian Sources and Inspiralling Compact Binaries’, *Living Reviews in Relativity* **17**(1), 2.

Blandford, R. D. and McKee, C. F. (1976), ‘Fluid dynamics of relativistic blast waves’, *Physics of Fluids* **19**, 1130–1138.

Bovard, L., Martin, D., Guercilena, F., Arcones, A., Rezzolla, L. and Korobkin, O. (2017), ‘r -process nucleosynthesis from matter ejected in binary neutron star mergers’, *Phys. Rev. D* **96**(12), 124005.

Burbidge, E. M., Burbidge, G. R., Fowler, W. A. and Hoyle, F. (1957), ‘Synthesis of the elements in stars’, *Rev. Mod. Phys.* **29**, 547–650.
URL: *https://link.aps.org/doi/10.1103/RevModPhys.29.547*

Cameron, A. G. W. (1957), ‘Nuclear reactions in stars and nucleogenesis’, *Publications of the Astronomical Society of the Pacific* **69**, 201.
URL: *https://doi.org/10.1086*

Capano, C. D., Tews, I., Brown, S. M., Margalit, B., De, S., Kumar, S., Brown, D. A., Krishnan, B. and Reddy, S. (2019), ‘GW170817: Stringent constraints on neutron-star radii from multimessenger observations and nuclear theory’, *arXiv e-prints* p. arXiv:1908.10352.

Chornock, R., Berger, E., Kasen, D., Cowperthwaite, P. S., Nicholl, M., Villar, V. A. and others (2017), ‘The Electromagnetic Counterpart of the Binary Neutron Star Merger LIGO/Virgo GW170817. IV. Detection of Near-infrared Signatures of r-process Nucleosynthesis with Gemini-South’, *ApJL* **848**(2), L19.

Ciolfi, R. (2020), ‘Collimated outflows from long-lived binary neutron star merger remnants’, *arXiv e-prints* p. arXiv:2001.10241.

Coughlin, M., Dietrich, T., Kawaguchi, K., Smartt, S., Stubbs, C. and Ujevic, M. (2017), ‘Toward Rapid Transient Identification and Characterization of Kilonovae’, *ApJ* **849**(1), 12.

Coughlin, M. W., Ahumada, T., Anand, S., De, K., Hankins, M. J., Kasliwal, M. M. and others (2019c), ‘GROWTH on S190425z: Searching Thousands of Square Degrees to Identify an Optical or Infrared Counterpart to a Binary Neutron Star Merger with the Zwicky Transient Facility and Palomar Gattini-IR’, *ApJL* **885**(1), L19.

Coughlin, M. W. and Dietrich, T. (2019), ‘Can a black hole-neutron star merger explain GW170817, AT2017gfo, and GRB170817A?’, *Physical Review D* **100**(4), 043011.

Coughlin, M. W., Dietrich, T., Margalit, B. and Metzger, B. D. (2019), ‘Multimessenger Bayesian parameter inference of a binary neutron star merger’, *MNRAS* **489**(1), L91–L96.

Coward, D. M., Howell, E. J., Piran, T., Stratta, G., Branchesi, M., Bromberg, O., Gendre, B., Burman, R. R. and Guetta, D. (2012), ‘The Swift short gamma-ray burst rate density: implications for binary neutron star merger rates’, *MNRAS* **425**(4), 2668–2673.

Cowperthwaite, P. S., Berger, E., Villar, V. A., Metzger, B. D., Nicholl, M., Chornock, R. and others (2017), ‘The Electromagnetic Counterpart of the Binary Neutron Star Merger LIGO/Virgo GW170817. II. UV, Optical, and Near-infrared Light Curves and Comparison to Kilonova Models’, *ApJL* **848**(2), L17.

Cromartie, H. T., Fonseca, E., Ransom, S. M., Demorest, P. B., Arzoumanian, Z., Blumer, H. and others (2020), ‘Relativistic Shapiro delay measurements of an extremely massive millisecond pulsar’, *Nature Astronomy* **4**, 72–76.

D’Avanzo, P., Campana, S., Salafia, O. S., Ghirlanda, G., Ghisellini, G., Melandri, A., Bernardini, M. G., Branchesi, M., Chassande-Mottin, E., Covino, S., D’Elia, V., Nava, L., Salvaterra, R., Tagliaferri, G. and Vergani, S. D. (2018), ‘The evolution of the X-ray afterglow emission of GW 170817/ GRB 170817A in XMM-Newton observations’, *AandA* **613**, L1.

D'Avanzo, P., Salvaterra, R., Bernardini, M. G., Nava, L., Campana, S., Covino, S., D'Elia, V., Ghirlanda, G., Ghisellini, G., Melandri, A., Sbarufatti, B., Vergani, S. D. and Tagliaferri, G. (2014), 'A complete sample of bright Swift short gamma-ray bursts', *MNRAS* **442**, 2342–2356.

de Mink, S. E. and Belczynski, K. (2015), 'Merger Rates of Double Neutron Stars and Stellar Origin Black Holes: The Impact of Initial Conditions on Binary Evolution Predictions', *ApJ* **814**(1), 58.

Dietrich, T., Bernuzzi, S., Ujevic, M. and Tichy, W. (2017), 'Gravitational waves and mass ejecta from binary neutron star mergers: Effect of the stars' rotation', *Phys. Rev. D* **95**(4), 044045.

Dietrich, T., Coughlin, M. W., Pang, P. T. H., Bulla, M., Heinzel, J., Issa, L., Tews, I. and Antier, S. (2020), 'New Constraints on the Supranuclear Equation of State and the Hubble Constant from Nuclear Physics – Multi-Messenger Astronomy', *arXiv e-prints* p. arXiv:2002.11355.

Djorgovski, S. G., Kulkarni, S. R., Bloom, J. S., Goodrich, R., Frail, D. A., Piro, L. and Palazzi, E. (1998), 'Spectroscopy of the Host Galaxy of the Gamma-Ray Burst 980703', *ApJL* **508**(1), L17–L20.

Dominik, M., Belczynski, K., Fryer, C., Holz, D. E., Berti, E., Bulik, T., Mand el, I. and O'Shaughnessy, R. (2012), 'Double Compact Objects. I. The Significance of the Common Envelope on Merger Rates', *ApJ* **759**(1), 52.

Dominik, M., Belczynski, K., Fryer, C., Holz, D. E., Berti, E., Bulik, T., Mand el, I. and O'Shaughnessy, R. (2013), 'Double Compact Objects. II. Cosmological Merger Rates', *ApJ* **779**(1), 72.

Dominik, M., Berti, E., O'Shaughnessy, R., Mandel, I., Belczynski, K., Fryer, C., Holz, D. E., Bulik, T. and Pannarale, F. (2015), 'Double Compact Objects III: Gravitational-wave Detection Rates', *ApJ* **806**, 263.

Duffell, P. C., Quataert, E., Kasen, D. and Klion, H. (2018), 'Jet Dynamics in Compact Object Mergers: GW170817 Likely Had a Successful Jet', *ApJ* **866**(1), 3.

Duncan, R. C., Shapiro, S. L. and Wasserman, I. (1986), 'Neutrino-driven Winds from Young, Hot Neutron Stars', *ApJ* **309**, 141.

Eichler, D., Livio, M., Piran, T. and Schramm, D. N. (1989), 'Nucleosynthesis, neutrino bursts and γ-rays from coalescing neutron stars', *Nature* **340**(6229), 126–128.
URL: *http://www.nature.com/doifinder/10.1038/340126a0*

Fahlman, S. and Fernández, R. (2018), 'Hypermassive Neutron Star Disk Outflows and Blue Kilonovae', *ApJL* **869**(1), L3.

Fernández, R., Foucart, F., Kasen, D., Lippuner, J., Desai, D. and Roberts, L. F. (2017), 'Dynamics, nucleosynthesis, and kilonova signature of black hole—neutron star merger ejecta', *Classical and Quantum Gravity* **34**(15), 154001.

Fernández, R., Kasen, D., Metzger, B. D. and Quataert, E. (2015), 'Outflows from accretion discs formed in neutron star mergers: effect of black hole spin', *MNRAS* **446**(1), 750–758.

Fernández, R. and Metzger, B. D. (2013), 'Delayed outflows from black hole accretion tori following neutron star binary coalescence', *MNRAS* **435**(1), 502–517.

Fernández, R. and Metzger, B. D. (2016), 'Electromagnetic Signatures of Neutron Star Mergers in the Advanced LIGO Era', *Annual Review of Nuclear and Particle Science* **66**(1), 23–45.

Fernández, R., Tchekhovskoy, A., Quataert, E., Foucart, F. and Kasen, D. (2019), 'Long-term GRMHD simulations of neutron star merger accretion discs: implications for electromagnetic counterparts', *MNRAS* **482**(3), 3373–3393.

Finstad, D., De, S., Brown, D. A., Berger, E. and Biwer, C. M. (2018), 'Measuring the Viewing Angle of GW170817 with Electromagnetic and Gravitational Waves', *ApJL* **860**(1), L2.

Flanagan, É. É. and Hinderer, T. (2008), 'Constraining neutron-star tidal Love numbers with gravitational-wave detectors', *Phys. Rev. D* **77**(2), 021502.

Fong, W., Berger, E., Margutti, R. and Zauderer, B. A. (2015), 'A Decade of Short-duration Gamma-Ray Burst Broadband Afterglows: Energetics, Circumburst Densities, and Jet Opening Angles', *ApJ* **815**(2), 102.

Foreman-Mackey, D., Hogg, D. W., Lang, D. and Goodman, J. (2013), 'emcee: The MCMC Hammer', *Publications of the Astronomical Society of the Pacific* **125**(925), 306.

Foucart, F. (2012), 'Black-hole-neutron-star mergers: Disk mass predictions', *Physical Review D* **86**, 124007.

Foucart, F., Duez, M. D., Kidder, L. E., Nissanke, S. M., Pfeiffer, H. P. and Scheel, M. A. (2019), 'Numerical simulations of neutron star-black hole binaries in the near-equal-mass regime', *Physical Review D* **99**(10), 103025.

Foucart, F., Hinderer, T. and Nissanke, S. (2018), 'Remnant baryon mass outside of the black hole after a neutron star-black hole merger', *ArXiv e-prints* p. arXiv:1807.00011.

Freiburghaus, C., Rosswog, S. and Thielemann, F.-K. (1999), 'r-process in neutron star mergers', *The Astrophysical Journal* **525**(2), L121–L124.
URL: *https://doi.org/10.1086*

Fryer, C. L., Belczynski, K., Wiktorowicz, G., Dominik, M., Kalogera, V. and Holz, D. E. (2012), 'Compact Remnant Mass Function: Dependence on the Explosion Mechanism and Metallicity', *ApJ* **749**(1), 91.

Fujibayashi, S., Kiuchi, K., Nishimura, N., Sekiguchi, Y. and Shibata, M. (2018), 'Mass Ejection from the Remnant of a Binary Neutron Star Merger: Viscous-radiation Hydrodynamics Study', *ApJ* **860**(1), 64.

Ghirlanda, G., Salafia, O. S., Paragi, Z., Giroletti, M., Yang, J., Marcote, B. et al. (2019), 'Compact radio emission indicates a structured jet was produced by a binary neutron star merger', *Science* p. aau8815.

Giacobbo, N. and Mapelli, M. (2018), 'The progenitors of compact-object binaries: impact of metallicity, common envelope and natal kicks', *MNRAS* **480**, 2011–2030.

Giacobbo, N., Mapelli, M. and Spera, M. (2018), 'Merging black hole binaries: the effects of progenitor's metallicity, mass-loss rate and Eddington factor', *MNRAS* **474**(3), 2959–2974.

Giacomazzo, B. and Perna, R. (2013), 'Formation of Stable Magnetars from Binary Neutron Star Mergers', *ApJL* **771**(2), L26.

Giacomazzo, B., Zrake, J., Duffell, P. C., MacFadyen, A. I. and Perna, R. (2015), ‘Producing Magnetar Magnetic Fields in the Merger of Binary Neutron Stars’, *ApJ* **809**, 39.

Gompertz, B. P., Levan, A. J., Tanvir, N. R., Hjorth, J., Covino, S., Evans, P. A., Fruchter, A. S., González-Fernández, C., Jin, Z. P. and Lyman, J. D. (2018), ‘The Diversity of Kilonova Emission in Short Gamma-Ray Bursts’, *ApJ* **860**(1), 62.

Gottlieb, O., Nakar, E., Piran, T. and Hotokezaka, K. (2018), ‘A cocoon shock breakout as the origin of the γ-ray emission in GW170817’, *MNRAS* **479**(1), 588–600.

Granot, J. and Kumar, P. (2003), ‘Constraining the structure of gamma-ray burst jets through the afterglow light curves’, *The Astrophysical Journal* **591**(2), 1086–1096.
URL: *https://doi.org/10.10862F375489*

Granot, J., Piran, T. and Sari, R. (2000), ‘The Synchrotron Spectrum of Fast Cooling Electrons Revisited’, *ApJl* **534**, L163–L166.

Granot, J. and Sari, R. (2002), ‘The Shape of Spectral Breaks in Gamma-Ray Burst Afterglows’, *ApJ* **568**, 820–829.

Granot, J. and van der Horst, A. J. (2014), ‘Gamma-Ray Burst Jets and their Radio Observations’, *Publications of the Astronomical Society of Australia* **31**, e008.

Grossman, D., Korobkin, O., Rosswog, S. and Piran, T. (2014), ‘The long-term evolution of neutron star merger remnants - II. Radioactively powered transients’, *MNRAS* **439**(1), 757–770.

Han, M.-Z., Tang, S.-P., Hu, Y.-M., Li, Y.-J., Jiang, J.-L., Jin, Z.-P., Fan, Y.-Z. and Wei, D.-M. (2020), ‘Is GW190425 Consistent with Being a Neutron Star-Black Hole Merger?’, *ApJL* **891**(1), L5.

Hawley, J. F., Fendt, C., Hardcastle, M., Nokhrina, E. and Tchekhovskoy, A. (2015), ‘Disks and Jets. Gravity, Rotation and Magnetic Fields’, *Space Science Reviews* **191**, 441–469.

Hempel, M. and Schaffner-Bielich, J. (2010), ‘A statistical model for a complete supernova equation of state’, *Nuclear Physics A* **837**, 210–254.

Hinderer, T., Nissanke, S., Foucart, F., Hotokezaka, K., Vincent, T., Kasliwal, M., Schmidt, P., Williamson, A. R., Nichols, D. A., Duez, M. D., Kidder, L. E., Pfeiffer, H. P. and Scheel, M. A. (2019), ‘Distinguishing the nature of comparable-mass neutron star binary systems with multimessenger observations: GW170817 case study’, *Phys. Rev. D* **100**(6), 063021.

Hotokezaka, K., Kiuchi, K., Kyutoku, K., Okawa, H., Sekiguchi, Y.-i., Shibata, M. and Taniguchi, K. (2013), ‘Mass ejection from the merger of binary neutron stars’, *Phys. Rev. D* **87**(2), 024001.

Hotokezaka, K., Nissanke, S., Hallinan, G., Lazio, T. J. W., Nakar, E. and Piran, T. (2016), ‘Radio Counterparts of Compact Binary Mergers Detectable in Gravitational Waves: A Simulation for an Optimized Survey’, *ApJ* **831**(2), 190.

Hotokezaka, K. and Piran, T. (2015), ‘Mass ejection from neutron star mergers: different components and expected radio signals’, *MNRAS* **450**(2), 1430–1440.

Iyyani, S. and Sharma, V. (2020), ‘Prompt emission of short gamma ray bursts: a clue to the viewing angle and the post-merger remnant’, *arXiv e-prints* p. arXiv:2007.00020.

Just, O., Bauswein, A., Ardevol Pulpillo, R., Goriely, S. and Janka, H. T. (2015), 'Comprehensive nucleosynthesis analysis for ejecta of compact binary mergers', *MNRAS* **448**(1), 541–567.

Kaplan, J. D., Ott, C. D., O'Connor, E. P., Kiuchi, K., Roberts, L. and Duez, M. (2014), 'The Influence of Thermal Pressure on Equilibrium Models of Hypermassive Neutron Star Merger Remnants', *ApJ* **790**(1), 19.

Kasen, D., Badnell, N. R. and Barnes, J. (2013), 'Opacities and Spectra of the r-process Ejecta from Neutron Star Mergers', *ApJ* **774**(1), 25.

Kasen, D., Fernández, R. and Metzger, B. D. (2015), 'Kilonova light curves from the disc wind outflows of compact object mergers', *MNRAS* **450**(2), 1777–1786.

Kasliwal, M. M., Coughlin, M. W., Bellm, E. C., Singer, L. P., De, K., Andreoni, I. and Duev, D. (2019), *Gamma-ray Coordinates Network Circulars* **24191**.

Kathirgamaraju, A., Tchekhovskoy, A., Giannios, D. and Barniol Duran, R. (2019), 'EM counterparts of structured jets from 3D GRMHD simulations', *MNRAS* **484**(1), L98–L103.

Kawaguchi, K., Kyutoku, K., Nakano, H., Okawa, H., Shibata, M. and Taniguchi, K. (2015), 'Black hole-neutron star binary merger: Dependence on black hole spin orientation and equation of state', *Physical Review D* **92**(2), 024014.

Kawaguchi, K., Kyutoku, K., Shibata, M. and Tanaka, M. (2016), 'Models of Kilonova/Macronova Emission from Black Hole-Neutron Star Mergers', *ApJ* **825**(1), 52.

Kawaguchi, K., Shibata, M. and Tanaka, M. (2020), 'Diversity of Kilonova Light Curves', *ApJ* **889**(2), 171.

Kiuchi, K., Kyutoku, K., Shibata, M. and Taniguchi, K. (2019), 'Revisiting the Lower Bound on Tidal Deformability Derived by AT 2017gfo', *ApJL* **876**(2), L31.

Kiuchi, K., Sekiguchi, Y., Kyutoku, K., Shibata, M., Taniguchi, K. and Wada, T. (2015), 'High resolution magnetohydrodynamic simulation of black hole-neutron star merger: Mass ejection and short gamma ray bursts', *Phys. Rev. D* **92**(6), 064034.

Kiziltan, B., Kottas, A., De Yoreo, M. and Thorsett, S. E. (2013), 'The Neutron Star Mass Distribution', *ApJ* **778**(1), 66.

Kochanek, C. S. (1992), 'Coalescing Binary Neutron Stars', *ApJ* **398**, 234.

Kohri, K., Narayan, R. and Piran, T. (2005), 'Neutrino-dominated Accretion and Supernovae', *ApJ* **629**(1), 341–361.

Komissarov, S. S. (2001), 'Direct numerical simulations of the Blandford-Znajek effect', *MNRAS* **326**, L41–L44.

Korobkin, O., Rosswog, S., Arcones, A. and Winteler, C. (2012), 'On the astrophysical robustness of the neutron star merger r-process', *MNRAS* **426**, 1940–1949.

Kulkarni, S. R. (2005), 'Modeling Supernova-like Explosions Associated with Gamma-ray Bursts with Short Durations', *arXiv e-prints* pp. astro–ph/0510256.

Kyutoku, K., Fujibayashi, S., Hayashi, K., Kawaguchi, K., Kiuchi, K., Shibata, M. and Tanaka, M. (2020), 'On the Possibility of GW190425 Being a Black Hole-Neutron Star Binary Merger', *ApJL* **890**(1), L4.

Kyutoku, K., Ioka, K., Okawa, H., Shibata, M. and Taniguchi, K. (2015), 'Dynamical mass ejection from black hole-neutron star binaries', *Physical Review D* **92**(4), 044028.

Landry, P., Essick, R. and Chatziioannou, K. (2020), 'Nonparametric constraints on neutron star matter with existing and upcoming gravitational wave and pulsar observations', *arXiv e-prints* p. arXiv:2003.04880.

Lattimer, J. M. and Prakash, M. (2001), 'Neutron Star Structure and the Equation of State', *ApJ* **550**(1), 426–442.

Lattimer, J. M. and Schramm, D. N. (1974), 'Black-hole-neutron-star collisions', *ApJl* **192**, L145–L147.

Lattimer, J. M. and Schramm, D. N. (1976), 'The tidal disruption of neutron stars by black holes in close binaries.', *ApJ* **210**, 549–567.

Li, L.-X. and Paczyński, B. (1998), 'Transient Events from Neutron Star Mergers', *ApJl* **507**, L59–L62.

Lippuner, J., Fernández, R., Roberts, L. F., Foucart, F., Kasen, D., Metzger, B. D. and Ott, C. D. (2017), 'Signatures of hypermassive neutron star lifetimes on r-process nucleosynthesis in the disc ejecta from neutron star mergers', *MNRAS* **472**(1), 904–918.

LVC (2010), 'TOPICAL REVIEW: Predictions for the rates of compact binary coalescences observable by ground-based gravitational-wave detectors', *Classical and Quantum Gravity* **27**, 173001.

LVC (2017*a*), 'GW170817: Observation of Gravitational Waves from a Binary Neutron Star Inspiral', *Phys. Rev. Lett.* **119**(16), 161101.

LVC (2018*a*), 'Binary Black Hole Population Properties Inferred from the First and Second Observing Runs of Advanced LIGO and Advanced Virgo', *arXiv e-prints* p. arXiv:1811.12940.

LVC (2018*b*), 'GW170817: Measurements of Neutron Star Radii and Equation of State', *Phys. Rev. Lett.* **121**(16), 161101.

LVC (2019*a*), *Gamma-ray Coordinates Network Circulars* **25829**.

LVC (2019*b*), *Gamma-ray Coordinates Network Circulars* **25871**.

LVC (2019*c*), *Gamma-ray Coordinates Network Circulars* **24168**.

LVC (2019*d*), 'GWTC-1: A Gravitational-Wave Transient Catalog of Compact Binary Mergers Observed by LIGO and Virgo during the First and Second Observing Runs', *Physical Review X* **9**(3), 031040.

LVC (2019*e*), 'Properties of the Binary Neutron Star Merger GW170817', *Physical Review X* **9**(1), 011001.

LVC (2020*a*), *Gamma-ray Coordinates Network Circulars* **26759**.

LVC (2020*b*), *Gamma-ray Coordinates Network Circulars* **27388**.

LVC (2020*c*), 'GW190425: Observation of a Compact Binary Coalescence with Total Mass $\sim 3.4 M_{\odot}$', *arXiv e-prints* p. arXiv:2001.01761.

LVC (2020*d*), 'GW190814: Gravitational Waves from the Coalescence of a 23 $\mathrm{M}_{\odot}$ Black Hole with a 2.6 $\mathrm{M}_{\odot}$ Compact Object', *arXiv e-prints* p. arXiv:2006.12611.

LVC, Fermi, I. (2017*b*), 'Gravitational Waves and Gamma-Rays from a Binary Neutron Star Merger: GW170817 and GRB 170817A', *ApJL* **848**(2), L13.

Maggiore, M. (2008), *Gravitational Waves: Volume 1: Theory and Experiments*, Gravitational Waves, OUP Oxford.
URL: *https://books.google.it/books?id=mk-1DAAAQBAJ*

Mandel, I., Haster, C.-J., Dominik, M. and Belczynski, K. (2015), 'Distinguishing types of compact-object binaries using the gravitational-wave signatures of their mergers', *MNRAS* **450**(1), L85–L89.

Mapelli, M. and Giacobbo, N. (2018), 'The cosmic merger rate of neutron stars and black holes', *MNRAS* **479**, 4391–4398.

Mapelli, M., Giacobbo, N., Santoliquido, F. and Artale, M. C. (2019), 'The properties of merging black holes and neutron stars across cosmic time', *arXiv e-prints* p. arXiv:1902.01419.

Margalit, B. and Metzger, B. D. (2017), 'Constraining the Maximum Mass of Neutron Stars from Multi-messenger Observations of GW170817', *ApJL* **850**(2), L19.

Margalit, B. and Metzger, B. D. (2019), 'The Multi-messenger Matrix: The Future of Neutron Star Merger Constraints on the Nuclear Equation of State', *ApJL* **880**(1), L15.

Margutti, R., Berger, E., Fong, W., Guidorzi, C., Alexander, K. D., Metzger, B. D. and others (2017), 'The Electromagnetic Counterpart of the Binary Neutron Star Merger LIGO/Virgo GW170817. V. Rising X-Ray Emission from an Off-axis Jet', *ApJL* **848**(2), L20.

Martin, D., Perego, A., Arcones, A., Thielemann, F. K., Korobkin, O. and Rosswog, S. (2015), 'Neutrino-driven Winds in the Aftermath of a Neutron Star Merger: Nucleosynthesis and Electromagnetic Transients', *ApJ* **813**(1), 2.

McBrien, O. R., Smartt, S. J., Huber, M. E., Rest, A., Chambers, K. C., Barbieri, C. and others (2020), 'PS15cey and PS17cke: prospective candidates from the Pan-STARRS Search for Kilonovae', *arXiv e-prints* p. arXiv:2006.10442.

Mendoza-Temis, J. d. J., Wu, M.-R., Langanke, K., Martínez-Pinedo, G., Bauswein, A. and Janka, H.-T. (2015), 'Nuclear robustness of the r process in neutron-star mergers', *Phys. Rev. C* **92**(5), 055805.

Metzger, B. D. (2019), 'Kilonovae', *Living Reviews in Relativity* **23**(1), 1.

Metzger, B. D. and Fernández, R. (2014), 'Red or blue? A potential kilonova imprint of the delay until black hole formation following a neutron star merger', *MNRAS* **441**(4), 3444–3453.

Metzger, B. D., Martínez-Pinedo, G., Darbha, S., Quataert, E., Arcones, A., Kasen, D., Thomas, R., Nugent, P., Panov, I. V. and Zinner, N. T. (2010), 'Electromagnetic counterparts of compact object mergers powered by the radioactive decay of r-process nuclei', *MNRAS* **406**(4), 2650–2662.

Metzger, B. D., Piro, A. L. and Quataert, E. (2009), ‘Neutron-rich freeze-out in viscously spreading accretion discs formed from compact object mergers’, *MNRAS* **396**(1), 304–314.

Metzger, B. D., Quataert, E. and Thompson, T. A. (2008), ‘Short-duration gamma-ray bursts with extended emission from protomagnetar spin-down’, *MNRAS* **385**(3), 1455–1460.

Metzger, M. R., Djorgovski, S. G., Kulkarni, S. R., Steidel, C. C., Adelberger, K. L., Frail, D. A., Costa, E. and Frontera, F. (1997), ‘Spectral constraints on the redshift of the optical counterpart to the γ-ray burst of 8 May 1997’, *Nature* **387**(6636), 878–880.

Miller, J. M., Ryan, B. R., Dolence, J. C., Burrows, A., Fontes, C. J., Fryer, C. L., Korobkin, O., Lippuner, J., Mumpower, M. R. and Wollaeger, R. T. (2019), ‘Full transport model of GW170817-like disk produces a blue kilonova’, *Phys. Rev. D* **100**(2), 023008.

Miller, M. C., Lamb, F. K., Dittmann, A. J., Bogdanov, S., Arzoumanian, Z., Gendreau, K. C. and others (2019a), ‘PSR J0030+0451 Mass and Radius from NICER Data and Implications for the Properties of Neutron Star Matter’, *ApJL* **887**(1), L24.

Mooley, K. P., Nakar, E., Hotokezaka, K., Hallinan, G., Corsi, A., Frail, D. A. and others (2018), ‘A mildly relativistic wide-angle outflow in the neutron-star merger event GW170817’, *Nature* **554**(7691), 207–210.

Most, E. R., Papenfort, L. J., Tsokaros, A. and Rezzolla, L. (2019), ‘Impact of High Spins on the Ejection of Mass in GW170817’, *ApJ* **884**(1), 40.

Mösta, P., Radice, D., Haas, R., Schnetter, E. and Bernuzzi, S. (2020), ‘A magnetar engine for short GRBs and kilonovae’, *arXiv e-prints* p. arXiv:2003.06043.

Nakar, E. and Piran, T. (2011), ‘Detectable radio flares following gravitational waves from mergers of binary neutron stars’, *Nature* **478**(7367), 82–84.

Narayan, R., Paczynski, B. and Piran, T. (1992), ‘Gamma-ray bursts as the death throes of massive binary stars’, *ApJl* **395**, L83–L86.

Nava, L., Vianello, G., Omodei, N., Ghisellini, G., Ghirlanda, G., Celotti, A., Longo, F., Desiante, R. and Barniol Duran, R. (2014), ‘Clustering of LAT light curves: a clue to the origin of high-energy emission in gamma-ray bursts’, *MNRAS* **443**, 3578–3585.

Nedora, V., Bernuzzi, S., Radice, D., Perego, A., Endrizzi, A. and Ortiz, N. (2019), ‘Spiral-wave Wind for the Blue Kilonova’, *ApJL* **886**(2), L30.

Nicholl, M., Berger, E., Kasen, D., Metzger, B. D., Elias, J., Briceño, C. and others (2017), ‘The Electromagnetic Counterpart of the Binary Neutron Star Merger LIGO/Virgo GW170817. III. Optical and UV Spectra of a Blue Kilonova from Fast Polar Ejecta’, *ApJL* **848**(2), L18.

Nitz, A. H., Dent, T., Davies, G. S., Kumar, S., Capano, C. D., Harry, I., Mozzon, S., Nuttall, L., Lundgren, A. and Tápai, M. (2019), ‘2-OGC: Open Gravitational-wave Catalog of binary mergers from analysis of public Advanced LIGO and Virgo data’, *arXiv e-prints* p. arXiv:1910.05331.

Nitz, A., Harry, I., Brown, D., Biwer, C. M., Willis, J., Dal Canton, T. et al. (2019b), ‘gwastro/pycbc: Pycbc release v1.13.5’.
URL: *https://doi.org/10.5281/zenodo.2581446*

Özel, F., Psaltis, D., Narayan, R. and McClintock, J. E. (2010), 'The Black Hole Mass Distribution in the Galaxy', *ApJ* **725**(2), 1918–1927.

Paczynski, B. (1986), 'Gamma-ray bursters at cosmological distances', *ApJL* **308**, L43–L46.

Panaitescu, A. and Kumar, P. (2000), 'Analytic Light Curves of Gamma-Ray Burst Afterglows: Homogeneous versus Wind External Media', *ApJ* **543**, 66–76.

Pannarale, F. (2013), 'Black hole remnant of black hole-neutron star coalescing binaries', *Physical Review D* **88**, 104025.

Pannarale, F. and Ohme, F. (2014), 'Prospects for Joint Gravitational-wave and Electromagnetic Observations of Neutron-star-Black-hole Coalescing Binaries', *ApJL* **791**(1), L7.

Pe'er, A. (2012), 'Dynamical Model of an Expanding Shell', *ApJ* **752**(1), L8.

Perego, A., Radice, D. and Bernuzzi, S. (2017), 'AT 2017gfo: An Anisotropic and Three-component Kilonova Counterpart of GW170817', *ApJL* **850**(2), L37.

Perego, A., Rosswog, S., Cabezón, R. M., Korobkin, O., Käppeli, R., Arcones, A. and Liebendörfer, M. (2014), 'Neutrino-driven winds from neutron star merger remnants', *MNRAS* **443**(4), 3134–3156.

Petrillo, C. E., Dietz, A. and Cavaglià, M. (2013), 'Compact Object Coalescence Rate Estimation from Short Gamma-Ray Burst Observations', *ApJ* **767**(2), 140.

Popham, R., Woosley, S. E. and Fryer, C. (1999), 'Hyperaccreting Black Holes and Gamma-Ray Bursts', *ApJ* **518**(1), 356–374.

Qian, Y.-Z. (2000), 'Supernovae versus neutron star mergers as the major r-process sources', *The Astrophysical Journal* **534**(1), L67–L70.
URL: *https://doi.org/10.1086*

Radice, D., Bernuzzi, S. and Perego, A. (2020), 'The Dynamics of Binary Neutron Star Mergers and of GW170817', *arXiv e-prints* p. arXiv:2002.03863.

Radice, D., Galeazzi, F., Lippuner, J., Roberts, L. F., Ott, C. D. and Rezzolla, L. (2016), 'Dynamical mass ejection from binary neutron star mergers', *MNRAS* **460**(3), 3255–3271.

Radice, D., Perego, A., Hotokezaka, K., Bernuzzi, S., Fromm, S. A. and Roberts, L. F. (2018c), 'Viscous-dynamical Ejecta from Binary Neutron Star Mergers', *ApJL* **869**(2), L35.

Radice, D., Perego, A., Hotokezaka, K., Fromm, S. A., Bernuzzi, S. and Roberts, L. F. (2018a), 'Binary Neutron Star Mergers: Mass Ejection, Electromagnetic Counterparts, and Nucleosynthesis', *ApJ* **869**(2), 130.

Radice, D., Perego, A., Zappa, F. and Bernuzzi, S. (2018b), 'GW170817: Joint Constraint on the Neutron Star Equation of State from Multimessenger Observations', *ApJL* **852**(2), L29.

Raithel, C. A., Özel, F. and Psaltis, D. (2018), 'Tidal Deformability from GW170817 as a Direct Probe of the Neutron Star Radius', *ApJL* **857**(2), L23.

Rastello, S., Mapelli, M., Di Carlo, U. N., Giacobbo, N., Santoliquido, F., Spera, M. and Ballone, A. (2020), ‘Dynamics of black hole - neutron star binaries in young star clusters’, *arXiv e-prints* p. arXiv:2003.02277.

Read, J. S., Lackey, B. D., Owen, B. J. and Friedman, J. L. (2009), ‘Constraints on a phenomenologically parametrized neutron-star equation of state’, *Phys. Rev. D* **79**(12), 124032.

Rees, M. J. (1988), ‘Tidal disruption of stars by black holes of 10^6-10^8 solar masses in nearby galaxies’, *Nature* **333**(6173), 523–528.

Riley, T. E., Watts, A. L., Bogdanov, S., Ray, P. S., Ludlam, R. M. and others (2019), ‘A NICER View of PSR J0030+0451: Millisecond Pulsar Parameter Estimation’, *ApJL* **887**(1), L21.

Roberts, L. F., Reddy, S. and Shen, G. (2012), ‘Medium modification of the charged-current neutrino opacity and its implications’, *Phys. Rev. C* **86**, 065803.
URL: *https://link.aps.org/doi/10.1103/PhysRevC.86.065803*

Rossi, A., Stratta, G., Maiorano, E., Spighi, D., Masetti, N., Palazzi, E., Gardini, A., Melandri, A., Nicastro, L. and Pian, E. (2019), ‘A comparison between short GRB afterglows and KN170817: shedding light on kilonovae properties’, *arXiv e-prints* p. arXiv:1901.05792.

Rosswog, S., Feindt, U., Korobkin, O., Wu, M. R., Sollerman, J., Goobar, A. and Martinez-Pinedo, G. (2017), ‘Detectability of compact binary merger macronovae’, *Classical and Quantum Gravity* **34**(10), 104001.

Rosswog, S., Piran, T. and Nakar, E. (2013), ‘The multimessenger picture of compact object encounters: binary mergers versus dynamical collisions’, *MNRAS* **430**, 2585–2604.

Salafia et al. (2020), ‘’, *in preparation* .

Salafia, O. S., Barbieri, C., Ascenzi, S. and Toffano, M. (2019b), ‘Gamma-ray burst jet propagation, development of angular structure, and the luminosity function’, *arXiv e-prints* p. arXiv:1907.07599.

Salafia, O. S., Ghirlanda, G., Ascenzi, S. and Ghisellini, G. (2019a), ‘On-axis view of GRB 170817A’, $AandA$ **628**, A18.

Salafia, O. S., Ghisellini, G., Pescalli, A., Ghirland a, G. and Nappo, F. (2015), ‘Structure of gamma-ray burst jets: intrinsic versus apparent properties’, *MNRAS* **450**(4), 3549–3558.

Santana, R., Barniol Duran, R. and Kumar, P. (2014), ‘Magnetic Fields in Relativistic Collisionless Shocks’, *ApJ* **785**, 29.

Sari, R., Piran, T. and Narayan, R. (1998), ‘Spectra and Light Curves of Gamma-Ray Burst Afterglows’, *ApJ* **497**, L17–L20.

Schutz, B. F. (2011), ‘Networks of gravitational wave detectors and three figures of merit’, *Classical and Quantum Gravity* **28**(12), 125023.

Shapiro, S. L. (2017), ‘Black holes, disks, and jets following binary mergers and stellar collapse: The narrow range of electromagnetic luminosities and accretion rates’, *Physical Review D* **95**, 101303.

Shibata, M. and Hotokezaka, K. (2019), ‘Merger and Mass Ejection of Neutron Star Binaries’, *Annual Review of Nuclear and Particle Science* **69**, 41–64.

Shibata, M. and Taniguchi, K. (2006), ‘Merger of binary neutron stars to a black hole: Disk mass, short gamma-ray bursts, and quasinormal mode ringing’, *Phys. Rev. D* **73**(6), 064027.

Shibata, M. and Taniguchi, K. (2011), ‘Coalescence of Black Hole-Neutron Star Binaries’, *Living Reviews in Relativity* **14**, 6.

Shibata, M. and Uryū, K. ō. (2000), ‘Simulation of merging binary neutron stars in full general relativity: Γ=2 case’, *Phys. Rev. D* **61**(6), 064001.

Siegel, D. M., Ciolfi, R., Harte, A. I. and Rezzolla, L. (2013), ‘Magnetorotational instability in relativistic hypermassive neutron stars’, *Phys. Rev. D* **87**(12), 121302.

Siegel, D. M. and Metzger, B. D. (2017), ‘Three-Dimensional General-Relativistic Magnetohydrodynamic Simulations of Remnant Accretion Disks from Neutron Star Mergers: Outflows and r -Process Nucleosynthesis’, *Phys. Rev. Let.* **119**(23), 231102.

Sironi, L., Spitkovsky, A. and Arons, J. (2013), ‘The Maximum Energy of Accelerated Particles in Relativistic Collisionless Shocks’, *ApJ* **771**, 54.

Soares-Santos, M., Holz, D. E., Annis, J., Chornock, R., Herner, K., Berger, E. and others (2017), ‘The Electromagnetic Counterpart of the Binary Neutron Star Merger LIGO/Virgo GW170817. I. Discovery of the Optical Counterpart Using the Dark Energy Camera’, *ApJL* **848**(2), L16.

Steiner, A. W., Hempel, M. and Fischer, T. (2013), ‘Core-collapse Supernova Equations of State Based on Neutron Star Observations’, *ApJ* **774**, 17.

Suwa, Y., Yoshida, T., Shibata, M., Umeda, H. and Takahashi, K. (2018), ‘On the minimum mass of neutron stars’, *MNRAS* **481**(3), 3305–3312.

Symbalisty, E. and Schramm, D. N. (1982), ‘Neutron Star Collisions and the r-Process’, *ApJL* **22**, 143.

Takahashi, K., Witti, J. and Janka, H. T. (1994), ‘Nucleosynthesis in neutrino-driven winds from protoneutron stars II. The r-process’, *AandA* **286**, 857–869.

Tanaka, M., Kato, D., Gaigalas, G. and Kawaguchi, K. (2019), ‘Systematic Opacity Calculations for Kilonovae’, *arXiv e-prints* p. arXiv:1906.08914.

Tchekhovskoy, A., Narayan, R. and McKinney, J. C. (2010), ‘Black Hole Spin and The Radio Loud/Quiet Dichotomy of Active Galactic Nuclei’, *ApJ* **711**, 50–63.

Thompson, T. A., Kochanek, C. S., Stanek, K. Z., Badenes, C., Post, R. S., Jayasinghe, T. and others (2019), ‘A noninteracting low-mass black hole-giant star binary system’, *Science* **366**(6465), 637–640.

Typel, S., Röpke, G., Klähn, T., Blaschke, D. and Wolter, H. H. (2010), ‘Composition and thermodynamics of nuclear matter with light clusters’, *Phys. Rev. C* **81**(1), 015803.

van Eerten, H., van der Horst, A. and MacFadyen, A. (2012), ‘Gamma-Ray Burst Afterglow Broadband Fitting Based Directly on Hydrodynamics Simulations’, *ApJ* **749**(1), 44.

van Paradijs, J., Kouveliotou, C. and Wijers, R. A. M. J. (2000), ‘Gamma-Ray Burst Afterglows’, *Annual Review of Astronomy and Astrophysics* **38**, 379–425.

Vangioni, E., Goriely, S., Daigne, F., François, P. and Belczynski, K. (2016), ‘Cosmic neutron-star merger rate and gravitational waves constrained by the r-process nucleosynthesis’, *MNRAS* **455**(1), 17–34.

Voss, R. and Tauris, T. M. (2003), ‘Galactic distribution of merging neutron stars and black holes - prospects for short gamma-ray burst progenitors and LIGO/VIRGO’, *MNRAS* **342**, 1169–1184.

Wollaeger, R. T., Korobkin, O., Fontes, C. J., Rosswog, S. K., Even, W. P., Fryer, C. L., Sollerman, J., Hungerford, A. L., van Rossum, D. R. and Wollaber, A. B. (2018), ‘Impact of ejecta morphology and composition on the electromagnetic signatures of neutron star mergers’, *MNRAS* **478**(3), 3298–3334.

Yagi, K. and Yunes, N. (2017), ‘Approximate universal relations for neutron stars and quark stars’, *Physics Reports* **681**, 1–72.

Ye, C. S., Fong, W.-f., Kremer, K., Rodriguez, C. L., Fragione, G. and Rasio, F. A. (2019), ‘On the Rate of Neutron Star Binary Mergers from Globular Clusters’, *arXiv e-prints* p. arXiv:1910.10740.

Zappa, F., Bernuzzi, S., Radice, D., Perego, A. and Dietrich, T. (2018), ‘Gravitational-Wave Luminosity of Binary Neutron Stars Mergers’, *PRL* **120**(11), 111101.

Zhang, B.-B., van Eerten, H., Burrows, D. N., Ryan, G. S., Evans, P. A., Racusin, J. L., Troja, E. and MacFadyen, A. (2015), ‘An Analysis of Chandra Deep Follow-up Gamma-Ray Bursts: Implications for Off-axis Jets’, *ApJ* **806**, 15.

Zhang, G. Q. and Wang, F. Y. (2018), ‘The Formation Rate of Short Gamma-Ray Bursts and Gravitational Waves’, *ApJ* **852**(1), 1.

Zhang, J., Yang, Y., Zhang, C., Yang, W., Li, D., Bi, S. and Zhang, X. (2019), ‘The mass distribution of Galactic double neutron stars: constraints on the gravitational-wave sources like GW170817’, *MNRAS* **488**(4), 5020–5028.

LIST OF PUBLICATIONS

1. C. Barbieri, O. S. Salafia, M. Colpi, G. Ghirlanda and A. Perego, 2020. “Distinguishing the nature of ambiguous merging systems hosting a neutron star: GW190425 in low-latency”. Submitted to Astronomy and Astrophysics.
2. C. Barbieri, O. S. Salafia, A. Perego, M. Colpi and G. Ghirlanda, 2020. “Electromagnetic counterparts of black hole-neutron star mergers: dependence on the neutron star properties”. The European Physical Journal A, Volume 56, Issue 1, 8.
3. C. Barbieri, O. S. Salafia, M. Colpi, G. Ghirlanda, A. Perego and A. Colombo, 2019. “Filling the mass gap: How kilonova observations can unveil the nature of the compact object merging with the neutron star”. The Astrophysical Journal Letters, Volume 887, Issue 2, L35.
4. C. Barbieri, O. S. Salafia, A. Perego, M. Colpi and G. Ghirlanda, 2019. “Light-curve models of black hole - neutron star mergers: steps towards a multi-messenger parameter estimation”. Astronomy and Astrophysics, Volume 625, A152.
5. O. S. Salafia, C. Barbieri, S. Ascenzi, M. Toffano, 2020. “Gamma-ray burst jet propagation, development of angular structure, and the luminosity function”. Astronomy and Astrophysics, Volume 636, id.A105.
6. O. R. McBrien, S. J. Smartt, M. E. Huber, A. Rest, K. C. Chambers, C. Barbieri, M. Bulla, S. Jha, M. Gromadzki, S. Srivastav, K. W. Smith, D. R. Young, S. McLaughlin, C. Inserra, M. Nicholl, M. Fraser, K. Maguire, T. Chen, T. Wevers, J. P. Anderson, T. E. Müller-Bravo, F. Olivares, E. Kankare, A. Gal-Yam, C. Waters, 2020. “PS15cey and PS17cke: prospective candidates from the Pan-STARRS Search for Kilonovae”. Submitted to MNRAS.

7. ENGRAVE collaboration, 2020. “Observational constraints on the optical and near-infrared emission from the neutron star-black hole binary merger S190814bv”. Submitted to Astronomy and Astrophysics.

8. LIGO Scientific Collaboration and Virgo Collaboration, 2020. Gravitational-wave Constraints on the Equatorial Ellipticity of Millisecond Pulsars. The Astrophysical Journal Letters, Volume 902, Issue 1, L21.

9. Virgo Collaboration, 2020. Quantum Backaction on Kg-Scale Mirrors: Observation of Radiation Pressure Noise in the Advanced Virgo Detector. Physical Review Letters, Volume 125, Issue 13, 131101.

10. LIGO Scientific Collaboration and Virgo Collaboration, 2020. GW190521: A Binary Black Hole Merger with a Total Mass of 150 $M\odot$. Physical Review Letters, Volume 125, Issue 10, 101102.

11. LIGO Scientific Collaboration and Virgo Collaboration, 2020. Properties and Astrophysical Implications of the 150 $M\odot$ Binary Black Hole Merger GW190521. The Astrophysical Journal Letters, Volume 900, Issue 1, L13.

12. LIGO Scientific Collaboration and Virgo Collaboration, 2020. “GW190814: Gravitational Waves from the Coalescence of a 23 Solar Mass Black Hole with a 2.6 Solar Mass Compact Object”. The Astrophysical Journal Letters, Volume 896, Issue 2, id.L44.

13. LIGO Scientific Collaboration and Virgo Collaboration, 2020. “GW190412: Observation of a Binary-Black-Hole Coalescence with Asymmetric Masses”. Physical Review D, Volume 102, Issue 4, 043015.

14. Virgo Collaboration, 2020. “The advanced Virgo longitudinal control system for the O2 observing run”. Astroparticle Physics, Volume 116, 102386.

15. LIGO Scientific Collaboration and Virgo Collaboration, 2020. “Model comparison from LIGO-Virgo data on GW170817’s binary components and consequences for the merger remnant”. Classical and Quantum Gravity, Volume 37, 4.

16. LIGO Scientific Collaboration and Virgo Collaboration, 2020. “GW190425: Observation of a Compact Binary Coalescence with Total Mass $\sim 3.4 M_{\odot}$”. The Astrophysical Journal Letters, Volume 892, Issue 1, id.L3.

17. Fermi Gamma-ray Burst Monitor Team, LIGO Scientific Collaboration and Virgo Collaboration, 2020. “A Joint Fermi-GBM and LIGO/Virgo Analysis of Compact Binary Mergers From the First and Second Gravitational-wave Observing Runs”. The Astrophysical Journal, Volume 893, Issue 2, id.100.

18. Virgo Collaboration, 2019. “Increasing the Astrophysical Reach of the Advanced Virgo Detector via the Application of Squeezed Vacuum States of Light”. Physical Review Letters, Volume 123, Issue 23, 231108.

19. LIGO Scientific Collaboration and Virgo Collaboration, 2019. “Open data from the first and second observing runs of Advanced LIGO and Advanced Virgo”. Submitted to Scientific Data.

20. LIGO Scientific Collaboration and Virgo Collaboration, 2019. “Search for Gravitational-wave Signals Associated with Gamma-Ray Bursts during the Second Observing Run of Advanced LIGO and Advanced Virgo”. The Astrophysical Journal, Volume 886, Issue 1, 75.

21. LIGO Scientific Collaboration and Virgo Collaboration, 2019. “Search for Subsolar Mass Ultracompact Binaries in Advanced LIGO’s Second Observing Run”. Physical Review Letters, Volume 123, Issue 16, 161102.

22. LIGO Scientific Collaboration and Virgo Collaboration, 2019. “Search for Eccentric Binary Black Hole Mergers with Advanced LIGO and Advanced Virgo during Their First and Second Observing Runs”. The Astrophysical Journal, Volume 883, Issue 2, 149.

23. LIGO Scientific Collaboration and Virgo Collaboration, 2019. “Search for intermediate mass black hole binaries in the first and second observing runs of the Advanced LIGO and Virgo network”. Physical Review D, Volume 100, Issue 6, 064064.

24. LIGO Scientific Collaboration and Virgo Collaboration, 2019. “A gravitational-wave measurement of the Hubble constant following the second observing run of Advanced LIGO and Virgo”. ArXiv e-print.

25. LIGO Scientific Collaboration and Virgo Collaboration, 2019. “An Optically Targeted Search for Gravitational Waves emitted by Core-Collapse Supernovae during the First and Second Observing Runs of Advanced LIGO and Advanced Virgo”. Physical Review D, Volume 101, Issue 8, 084002.

26. LIGO Scientific Collaboration and Virgo Collaboration, 2019. “All-sky search for short gravitational-wave bursts in the second Advanced LIGO and Advanced Virgo run”. Physical Review D, Volume 100, Issue 2, 024017.

27. LIGO Scientific Collaboration and Virgo Collaboration, 2019. “All-sky search for long-duration gravitational-wave transients in the second Advanced LIGO observing run”. Physical Review D, Volume 99, Issue 10, 104033.